Combination of optical coherence tomography and Raman spectroscopy

Dissertation

zur Erlangung des akademischen Grades doctor rerum naturalium

(Dr. rer. nat.)

vorgelegt dem Rat der Chemisch-Geowissenschaftlichen Fakultät der

Friedrich-Schiller-Universität Jena

von **Kokila Dampali Egodage**

geboren am 23.04.1988 in Galle, Sri Lanka

Gutachter:

1. Prof. Dr. Jürgen Popp, Institut für Physikalische Chemie, FSU Jena

2. Prof. Dr. Volker Deckert, Institut für Physikalische Chemie, FSU Jena

Tag der Verteidigung: 27. Juni 2018

Table of Contents

List of abbreviations

AR	anti-reflective
BCC	basal cell carcinoma
CARS	coherent anti-stokes Raman spectroscopy
CVD	cardiovascular disease
EvG	elastic van Gieson
FLIM	fluorescence lifetime imaging
FOV	field of view
GRIN	gradient index
H&E	hematoxylin and eosin
IVUS	intravascular ultrasound
MM	multimode
NCF	no-core fiber
NIRS	near infrared spectroscopy
OCT	optical coherence tomography
SCC	squamous cell carcinoma
SD	spectral domain
SHG	second harmonic generation
SMF	single mode fiber
SNR	signal-to-noise ratio
SS	swept source
TD	time domain
TPEF	two-photon excitation microscopy

Acknowledgements

First, I would like to thank Carl Zeiss for funding this project and allowing me to accomplish this challenging adventure. My sincere gratitude goes to Dr. Sebastian Dochow and Dr. Christian Matthäus for taking me under their wings, training me throughout my PhD and preparing me for the big bad world. You two have provided me with knowledge, lots of courage and motivation in the past three or so years. Immense gratitude also goes to apl. Prof. Schmitt and Prof. Popp for being the strong pillars of the institute where all the scientific magic happens. In my first year I was working at Dr. Christoph Krafft's laboratory and I am very thankful for this time as I was able to work with Dr. Sara Piqueras from Spain with whom I now share a publication.

My loving parents, thank you for supporting and allowing me to go on this journey (with so much hesitation) and keeping up with my stressful and unstable lifestyle. Thank you for being strong and always helping me when I am knee deep in trouble. I cannot repay you enough for everything you have sacrificed for me.

My dear fellow office mates: Jan and Roman (my heroes in R), Katharinchen, Iwan, Clärchen (thank you for the corrections), Tania and Mohamed. Thank you enough for being supportive and making even the tough times pass-on like a breeze. Our group fun times and Christmas parties were the best! I am sure I will never find an amazing working group as you all. I am going to miss you dearly.

Friedrich, thank you for motivating me and saying everything will be OK. Thank you for believing in me, having faith and for not giving up on me. Thank you for training my German language skills and giving me confidence to speak it. You reminded me of myself when I was young, ambitious and wanting to reach the stars. That reminder helped me get through this chapter of my life.

Finally, I would like to list some of those who have helped me by even a teeny tiny bit: Michael Hermes, Marcel Dahms, Stefan Hanf, Andreas Hänsel, Albrecht, Michael Teupser, Martin, Per-Christian Heisel, Christian Karass, Alexandar Lukic, Anuradha Ramoji, Antje Raabe, Marion Krause, Annett Bodien, Dorit Schmidt, Mario Kindermann, Martina Hampel and Benita Göbel. The blue overall crew (Detlef, Georg, Robert and etc.) should not be forgotten as they would always come to my rescue whenever I needed help. Those outside campus who had been my emotional support include Ajay, Bjoern, Pascal and Jeremy, thank you for the companionship over the years. Of course, Hina Nisar, my best friend since high school, have been supporting me from far far away through prayers and words at all times.

To conclude, I am very grateful for being able to complete my doctoral project in Jena, Germany, as I have had very many memorable experiences that have allowed me to be the person I am now.

1 Introduction

Medical devices have evolved dramatically since the introduction of X-ray imaging into routine hospital procedures. This trend was a result of the essential need to screen for diseases that are located deep within the body. Nowadays, endoscopes are being widely used to provide prognostic information followed by targeted therapeutics increasing patient recovery rates [1, 2]. Therefore, novel medical device development is generally heading towards providing an accurate and early *in vivo* diagnosis at a faster rate, with no or minimal invasiveness. Many efforts are being promoted to produce devices to fulfill these standards, especially to diagnose diseases with a strategic advantage i.e. those tending towards increased recovery rates upon early diagnosis. Diseases such as cancer and atherosclerosis fall into this category. It has been shown that early diagnosis and targeted medication, either surgical or therapeutic, increase the chances of recovery significantly. The importance of early diagnosis has been observed, for example, by the 70% reduction in mortality in cervical cancer since the introduction of the Pap smear screening test [3]. Many early screening programs for a wide range of diseases have been implemented to promote early detection as the chance of recovery decreases drastically along with disease progression. This is very well observed with cancer which has become the second leading cause of death in the United States alone, and it has been estimated that in the year 2030 the numbers will increase to 13 million worldwide with 21.7 million new cases [4]. The main cause of cancer is still subject to speculation where specific mutations, exposure to the sun and modern lifestyle are only a few probable causes. These internal and external factors can induce cells to proliferate at an abnormal rate thereby producing a necrotic cell mass at the core that continues its growth unless intervened. This manifestation is termed as a ‘tumor’ and if the proliferation becomes aggressive, these cells would reach the blood stream and spread through the organism resulting in metastasis (malignant) whereas benign cancers are mostly confined to certain regions. Lack of care or neglect, however, would dramatically decrease the chances of recovery resulting in eventual death [4].

Similar to cancer, modern lifestyle and aging are well-known causes of atherosclerosis which is one of the cardiovascular diseases (CVD) that takes more than 17 million lives each year globally [5]. Due to damage or inflammation, arterial endothelium membranes can become susceptible to deposition and permeation of various lipids circulating through the bloodstream such as cholesterol and cholesterol ester. At the onset of this process, monocytes, a type of white blood cells, become attracted to and move into the arterial membrane. There, they differentiate into macrophages, taking up lipids and other cellular debris. Macrophages play an important role in lipid decomposition within tissue but can be overwhelmed by toxic lipid levels in the blood stream causing metabolic stress, subsequent cell death and the accumulation of cellular debris, which produce arterial swelling. This localized effect results in a lipid-rich plaque that eventually may cause a state of atherothrombosis leading to fatal consequences such as myocardial infarction or stroke. The biochemical composition of arterial plaques can vary [6] and it is well known that the severity of a plaque and its stability are strongly correlated with its biochemical composition [7]. Despite the long-term prevalence of CVDs, the identification of vulnerable plaques remains one of the most important and challenging aspects in cardiology. There are several types of vulnerable plaques with distinct biochemical compositions. For example, most common characteristics range within complex lipid cores, thin fibrous caps infiltrated by macrophages, proteo-glycan matrices in a smooth muscle cell-rich environment, intra-plaque hemorrhage and calcific nodules invading the arterial lumen [8]. Hence, having specific biochemical information of plaque composition would greatly improve the risk assessment and management of atherosclerosis.

MOTIVATION

The current 'gold standard' for cancer diagnosis is via microscopic imaging of stained tissue slices. This routine sample extracting procedure consists of a tissue biopsy performed by a surgeon and the difficulty in this procedure depends strongly on the tumor location. For example, tumors of internal organs lead to complicated and painful surgical procedures in which all efforts would be eventually dedicated to diagnosis. The biopsied sample is then sectioned and stained most commonly by hematoxylin and eosin (H&E) to reveal subcellular features where a histopathologic diagnosis is conducted by a well-trained individual (pathologist) to identify the type and stage of tumor. This procedure is well known to have false positives and long waiting times that heavily affect the standard of patient care [9, 10]. If the biopsy results show signs of a tumor, appropriate intervening steps would be taken, depending on the stage of disease progression. In the case of the former, the patient maybe called for another biopsy, resulting in higher costs and expenditures. This can be avoided all together with the routine utilization of efficient and specific diagnostic tools.

The term 'optical biopsy' in disease inspection was coined as an alternative method to tissue biopsy where light and its properties are used to produce cross-sectional images of biological matter. This was an outcome from a field of life science known as biophotonics, which uses optical and spectroscopic methods to characterize diseases at a molecular level either by high-resolution imaging or identifying biomarkers [11]. Clinically incorporated imaging methods, such as computed tomography (CT), magnetic resonance imaging (MRI) and ultrasound imaging, fulfill the criteria of obtaining non-invasive cross-sectional images of tissue [12]. Even though these techniques are readily used to obtain detailed images from hard-to-access regions such as the cranial cavity, they have disadvantages due to their basic working principles. For example, CT scans require a contrast agent to achieve better imaging quality due to the applied X-ray radiation, which in fact can be harmful to the patient. Despite its high resolution, CT scanning devices are bulky, a property shared with MRI. Based on magnetic fields, the latter also requires contrast agents and is very costly. Ultrasound exceeds all aforementioned disadvantages but lacks high-resolution capability. Thus, a niche for an imaging technique exists that must be compact, inexpensive and produces high resolution images. After the large interest in the field of ophthalmology in recent years, optical coherence tomography (OCT) seems to fill this space suitably [13]. It is based on interferometric imaging that utilizes coherent property of light to image subsurface morphology. Since then, OCT has been used in many biomedical applications and has been readily used in some countries as an optical guidance in cardiac surgeries such as bypass and stent implants [14]. In addition, there has been experimental work done on identifying non- melanoma and pre-cancers *in vivo* [15, 16]. The suitability of OCT for detecting skin cancers had been confirmed by the successful correlation of cross-sectional OCT images of basal cell carcinoma (BCC) with histopathologic data [17-20]. Detailed information on tumor morphology with a spatial resolution in the order of 10- 15 µm and a penetration depth of 1- 2 mm in skin have been reported [21-23]. This method would be able to extract more information as opposed to dermoscopy that has been widely used as a screening method. It provides the color and minimal microstructural features that would require well trained personnel for a subjective diagnosis [24].

A technique complementary to cross-sectional imaging would be a method that provides specific chemical information that identifies the molecular ‘fingerprint’ of the substance under investigation. Extensive research has been conducted especially in the field of fluorescence as well as infrared spectroscopy that has shown the feasibility of applying analytical methods to differentiate between diseased and healthy tissue [25, 26]. The application of optical spectroscopic methods primarily in biology and medicine was due to the large matrix of molecular combinations that require high chemical specificity and thus a need for a method that provides consistent data [27]. Raman spectroscopy is suitable for this application as it enables accurate and specific molecular identification. It has also been widely used in numerous disease recognition studies that have gained acceptance as a powerful histopathologic tool especially in optical biopsies [28, 29]. A large variety of cancer types have been analyzed using Raman spectroscopy [30-32] but the only drawback of this technique in biomedical application is its low sensitivity which results in large measuring or integration times.

Therefore, as a proposed solution, a combination of OCT and Raman spectroscopy is presented followed by the outcome of its application in characterizing non-melanoma skin cancers as well as atherosclerotic plaques. This effort required a novel biomedical device applicable in diagnostic routines, capable of imaging as well as obtaining chemical information. Thus, two modalities were included where one captures depth information in the form of a real-time image and the other provides spectroscopic data from desired regions with high biochemical specificity. Pioneered by the group of Anita Mahadevan-Jansen, a combination of OCT and Raman spectroscopy had been used to investigate *in vivo* non-melanoma skin cancers [33-35]. Other groups have applied the same concept for inspecting *ex vivo* porcine retinas [36] and psoriasis [36, 37].

The second type of disease in question is atherosclerosis and the associated plaques have been investigated *in vivo* via imaging techniques such as intravascular ultrasound (IVUS), CT and OCT [38, 39]. It is a challenge to obtain reliable information about the stage and type of plaques accurately with imaging methods purely. Most vital changes that occur are within their chemical composition and topology. With more advanced plaques, a fibrous thin cap has been commonly observed that would cover the lipid-rich core which becomes highly unstable and, on sudden rupture, causes a cardiac event. The current clinical diagnostic routine involves echocardiography and angiography to pinpoint blocked arteries. Most commonly, urgent cases are treated with stent implants that would prevent ischemia. So far, studies conducted on autopsies have been the most reliable in terms of plaques that cause coronary thrombosis [40]. *Ex vivo* measurements conducted on postmortem human arteries using IVUS and near infrared spectroscopy (NIRS) have correlated results from both modalities to show the feasibility of such a combination [41, 42]. This particular study proved that including a spectroscopic method improved the sensitivity and accuracy of diagnosis compared to using IVUS alone. Because Raman spectroscopy is inherently slower than OCT, the former would not be suited for intravascular imaging as a standalone. A combination with IVUS would be certainly less feasible as the associated signal generation and detection technologies are completely different. However, signal transduction for NIRS and IVUS also need to be realized by two different types of fibers. The main reason to combine NIRS with IVUS had been that both techniques function at a similar speed, so that the signals can be co-registered [41]. Apart from intravascular vibrational spectroscopy, several other spectroscopic approaches have been suggested and are currently under investigation. Fluorescence based techniques such as two-photon excitation fluorescence (TPEF) and FLIM are certainly fast enough to record images and have been utilized to characterize atherosclerotic plaques [43-46]. TPEF has been combined often with other multiphoton processes, such as second harmonic generation (SHG) and coherent anti-Stokes Raman scattering (CARS), a much faster, but also more complicated variant of Raman spectroscopy [47-50]. However, for these multimodal techniques reliable optical fibers that are applicable for *in vivo* imaging need to be developed.

One of the main differences between the two diseases investigated here had been the accessibility to disease locations, apart from the prevalence of the disease. Detecting skin cancers has an obvious simplicity compared to any other type of cancer as a microscopic setup is able to access the locations in an *in vivo* scenario. However, the experiments on non-melanoma skin cancers had been conducted *ex vivo* as it was a preliminary pilot study. Investigating atherosclerotic plaques *in vivo*, on the other hand, require a flexible catheter that can reach inner arterial walls for identifying affected regions. As part of the investigation, an OCT needle probe was built in collaboration with the University of Perth, Australia, that will be integrated with Raman spectroscopy in the future. Since both OCT and Raman spectroscopy utilize laser light in the NIR region, a fiber probe would be technologically feasible. Similar needle probes have been utilized mainly to investigate breast cancer and lung tissue as a puncture incision is not surgically challenging and would heal quicker which reduces the level of invasiveness [51, 52]. As a proof of concept the combined OCT-Raman investigations on arteries were also conducted under *ex vivo* conditions.

The application of this combined setup on disease diagnostic routines, has great potential to reduce false positives eliminating intraoperative variations and diagnostic efforts [53]. The benefits would be in terms of better patient care and a positive economic impact by avoiding unnecessary labor costs [54]. Furthermore, the scenarios in operating theaters would change in a way that the surgeons will be guided through surgeries via live imaging with high accuracy and speed. As a final step, the presence and/or removal of all diseased tissue will be confirmed by a chemically specific spectroscopic method such as Raman spectroscopy thus avoiding patients to be called for a follow-up surgery. This would promote taking advantage of the high molecular specificity of Raman spectroscopy and highly detailed image scanning capability of OCT, which would help achieving an improved quality in disease diagnosis.

1.1 Outline of thesis

An outline of the chapters has been described below.

- Chapter 2 presents the theory of OCT that elaborates on the working principle and the different types. A similar format has been used for Raman spectroscopy followed by an overview of the combination.

- Chapter 3 provides a thorough account of the implementation of the combined OCT- Raman device. The reasoning for using specific components have been explained. The preliminary tests utilized to characterize the device has been described as well.
- Chapter 4 exhibits the results of a pilot clinical study on non-melanoma skin cancers. This chapter discusses the correlation of OCT and Raman data with histopathology.
- Chapter 5 addresses the outcome of the combined OCT-Raman application on aortas *ex vivo* and *in vivo* to characterize atherosclerotic plaques. Apart from the data types dealt with earlier, X-ray imaging have been introduced that was used only with the *in vivo* experiments.
- Chapter 6 investigates the feasibility of an OCT needle-probe developed for atherosclerotic plaque measurements.
- Chapter 7 summarizes the results and provides an outlook for future methods to improve methodology and the analytical outcome.

2 Theory

2.1 Optical coherence tomography

Optical coherence tomography (OCT) is an interferometric method that was introduced in the 90s by a group at MIT [55]. Its development for clinical applications took off by the successful investigations in ophthalmology as OCT was utilized to obtain high resolution cross-sectional images (tomography) of the retina [56, 57]. Since then, studies have been conducted in many fields including cardiovascular and skin cancer imaging, to visualize tissue pathology without laborious clinical measures [17, 23, 58, 59]. There are a few different types of OCT systems that will be explained in detail in the following.

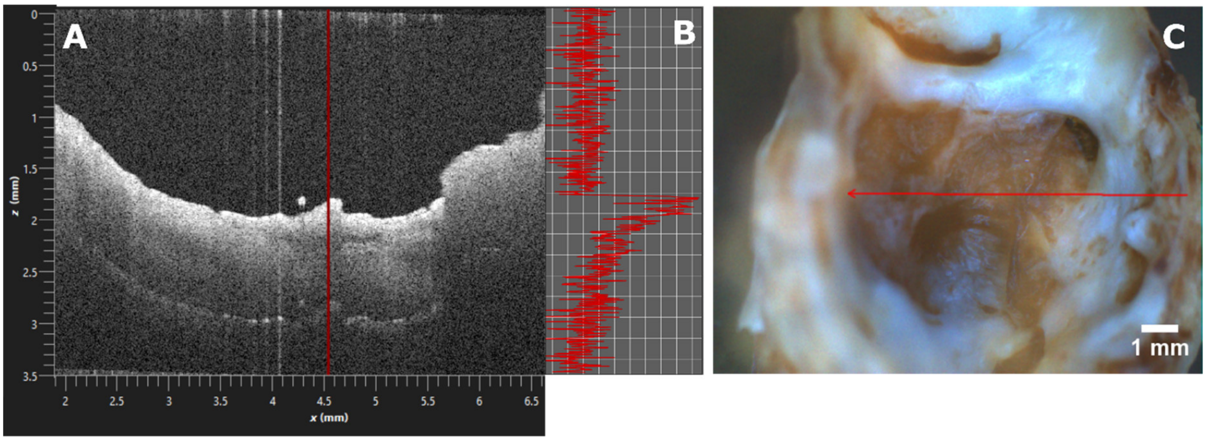

Figure 2.1: A- cross-sectional image of a cavity observed from an excised human aorta collected from a spectral domain OCT (Telesto SD-OCT, Thorlabs). The tissue morphology beneath the surface can be seen and at the 4.5 mm mark (red vertical line) an A-scan was recorded shown in B. The corresponding line measurement (red arrow in C) has been overlaid on the camera image of the aorta.

As an example, Fig. 2.1 A shows a 2D cross-sectional image (B-Scan) of an excised human aorta and it is composed of a collection of axial scans (Fig. 2.1 B, A-Scan). A corresponding camera image of the aorta (Fig. 2.1 C) shows the length where the line measurement had been conducted. A 3D or volumetric data set (C-Scan) can also be produced by stacking all 2D images of a region of interest. Thus it can be shown that OCT systems enable an ‘optical biopsy’ by comparing back scattered electromagnetic waves from the sample with that of the incident waves.

The working of an OCT system is such that, first, the incident laser light is split via a beam splitter, whereby one part is directed to the sample and the other to a reflecting mirror which acts as a reference. Then, back scattered light from the sample and light from the reflected mirror undergo interference only when the lengths of the reference and sample arms are matching within the coherence length, a property of the incident laser light [60]. Since the coherence length is inversley proportional to the axial depth resolution, broad bandwidth illumination sources (low coherence) are usually used in OCT imaging. Lateral resolution has no effect on the axial resolution, as the former depends on the spot size goverened by the objective optics. However, the lateral resolution at a given wavelegnth is inversely proportional to the depth of field [61]. Therefore the NA of the objective lens has an effect on the visualized z-axis range. The penetration depth is governed by the principle wavelength and the light-sample interactions such as absoprtion and scattering [62, 63]. Since water is the main constituent of tissue, wavelegnths longer than ~2000 nm would result in high vibrational absoprtion that would reduce the achievable penetration depth [64]. Therefore, it is important to choose the appropriate wavelegnth for a working OCT device.

To probe into the sample and obtain depth information, the reference arm is scanned a given distance (Δz) as shown in Fig 2.2. This method is known as time domain (TD) OCT.

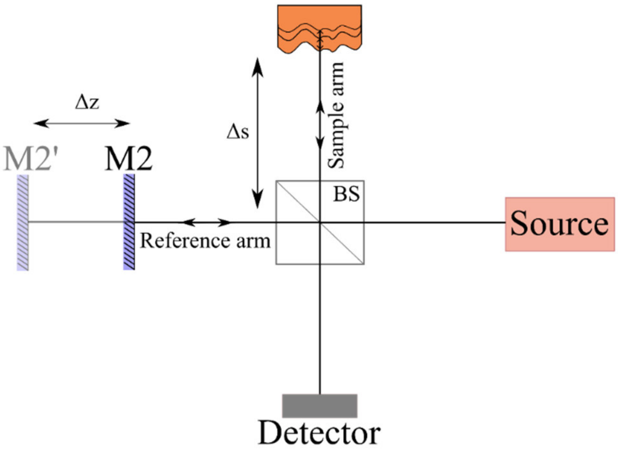

Figure 2.2: Time domain OCT (TD-OCT) setup with a sample with underlying layers at the end of the sample arm. Δz is the distance the reference arm is moved to obtain subsurface infromation from the sample where as Δs is the length of the sample arm which remains constant. Adapted from [60]

The above illustrated setup consumes time for the reference arm adjustment and involves moving parts resulting in reduced stability. To overcome these drawbacks, Fourier or spectral domain OCT (FD-OCT) has been developed where the reference mirror is kept at a constant position matching the length of the sample arm. The detector is replaced by a spectrometer followed by a high-speed line camera and the detected response is Fourier transformed to obtain time information, thus extracting depth related information.

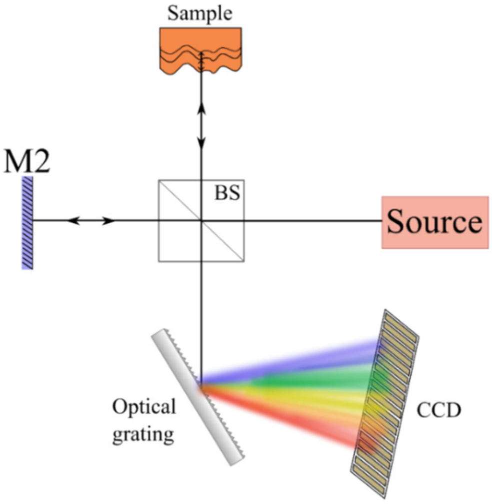

Figure 2.3: Fourier or spectral domain OCT (SD-OCT) setup. The optical grating represents the spectrometer. Adapted from [60]

Since there are no moving parts in the SD-OCT setup, all signals from the measurement depth are collected and Fourier transformed [65]. This may also produce ghost images and other unwanted artefact on the image but provides a higher senstivity than TD-OCT. This also means that SD-OCT has a higher signal to noise ratio (SNR) which can be beneficial for reducing the amount of laser power in biomedical applications. As SD-OCT detects all the signals from the entire depth, using Fourier transform the interference pattern can be reconstructed to extract specific responses originating from a given point in depth. In terms of depth or axial resolution both SD- and TD-OCT have a dependence on the spectral bandwidth of the source [66].

Similar to SD-OCT, another type of Fourier domain OCT system known as swept source OCT (SS-OCT) has emerged that uses a narrow bandwidth swept source which avoids the use of a spectrometer but employs a single photo-detector instead. This type of continuous wave laser excitation provides a much larger intensity than the laser source used on an SD-OCT i.e. a superluminescent LED source. Therefore, SS-OCT produces a larger tissue penetration depth [67] compared to SD-OCT. Since the sample signal is received at evenly spaced frequencies, applying a discrete Fourier transform would provide depth information [65]. With the swept source, the amount of noise would be reduced as opposed to the broadband source. For the results presented in chapters 3, 4 and 5 SD-OCT and SS-OCT have been used since they are the most suitable for biomedical applications in terms of sensitivity and speed.

2.2 Raman spectroscopy

Raman spectroscopy generates spectra that represent molecular fingerprints of tissue components. As it is chemically specific and does not require the use of contrast agents, the possibilities of medicinal application has become an intensely studied topic. When laser light interacts with matter, part of the energy is absorbed and another part is scattered. A large fraction of the scattered light would maintain the original frequency (Rayleigh scattering, see Fig. 2.4) but the other smaller fraction would be shifted in frequency. The latter which has influenced molecular vibration, holds the characteristics of the molecules. This phenomenon has been named after its discoverer and is called the Raman effect [68].

Raman scattered photons are a result of interactions which are initiated by absorption of an incident photon. This promotes the molecule to a higher energy state (virtual). Due to its unstable state, the molecule recedes to an energy state higher than its vibrational ground state which emits a Raman photon also known as an inelastically scattered photon. The energy detected during this Stokes event is red shifted. If the molecule is already at a higher energy state and after emitting a photon, lands in the ground state, blue shifted anti-Stokes photons can be observed [69] (Fig. 2.4).

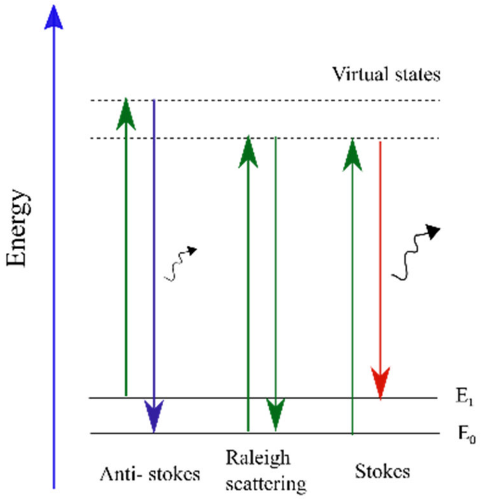

Figure 2.4: Jablonski diagram showing Anti- stokes, Rayleigh scattering and Stokes responses.

Raman scattering is limited by the change in polarizability between the ground and excited states as well as the molecular symmetry. The intensity of scattered photons relates to the polarizability and therefore Raman spectroscopy can be used as a means to quantify specific molecular groups [70, 71].

The collection and separation of Raman scattered light is carried out by a spectrometer and visualized as a spectrum. Usually CCDs are used to detect Raman emitted photons displayed as spectra. Excitation wavelengths in the visible light range produce broad fluorescence when used on tissue that masks Raman responses. This is because visible wavelengths contain the suitable energy difference to promote fluorescence. Therefore, near infrared (IR) light is used to investigate biological tissues as it contributes to reduced fluorescence. Wavelengths around 800 nm have shown optimal Raman spectral results with minimal fluorescence disturbance. However, at longer wavelengths, i.e. more than 850 nm, the current silicon based CCD cameras meet a sudden drop of detector efficiencies from 1000 – 1100 nm. Thus, an appropriate wavelength must be chosen for the given application.

The collection of back scattered photons on a microscopic setup is carried out via an objective lens usually with a high-NA in order to have a wide collection angle. This would be then coupled to an optical fiber that guides the light to a slit on the spectrograph. The diverging light is collimated and directed to a grating that disperses the beam at varying angles which is then directed to the detector. There are different types of gratings and ways of fabrication but its general function is to separate the components of light and governs the spectrometer resolution.

In order to identify the separated wavelength components, the Raman instrument must be calibrated using a known material, such as cyclohexane and 1,4-Acetamidophenol to interpolate the wavelength [72]. This is a necessary step when replacing the grating or starting the instrument. The calibration step is important especially in medical applications to achieve high accuracies and to be highly reproducible. Once the known material has been measured, specific peaks that relate to certain wavelengths are associated to given pixels on the CCD. By the known peaks of the standard material, the wavelength can be extrapolated using a third-order polynomial regression. Intensity calibration is also usually carried out to account for varying quantum efficiencies of the grating and pixels at different wavelengths [73]. Thus system artefacts originating from the optical components can be avoided.

In addition to optimizing the spectrograph, the Raman backscattered photons must be collected with minimal loss. However, applying this setup in a clinical setting, requires careful consideration of the specific application. If the Raman signals must be collected from locations that are hard to reach, an optic fiber probe must be used that will not produce its own Raman spectra and resist sterilization processes in the hospital [68].

3 Material and methods

The main goal of including two modalities with complementary strengths is to gain both morphological and chemical information from a single measurement which would save time and effort significantly. When considering the clinical workflow, OCT would be used first to obtain quick information on tissue morphology in order to track or recognize signs of disease. If any unusual sightings were to be found, the region would be inspected using Raman spectroscopy which identifies any molecular abnormalities. This chemical confirmation would be able to diagnose diseases accurately with the help of an algorithm or a separate database.

3.1 OCT-Raman combination for clinical application

Current clinical needs have paved the development of novel medical devices either for guided surgeries or early diagnosis [74]. In these applications, large tissue areas require real-time investigation that costs measurement time. This is an important factor that governs the diagnosis strategy and workflow. Compliance to standard clinical processes and having the advantage of a compact and mobile built are some key factors that the medical industry places emphasis on regarding biomedical devices.

There have been a number of studies within the past 10 years that confirm the benefits of using spectroscopic and optical methods for diagnosing skin cancers. Majority of the groups have used fiber probes to collect data, the datasets include more than 100 samples and constitute of different types of non-melanoma as well as melanoma cancers. Some of the groups had combined Raman spectroscopy with other modalities such as auto fluorescence [75], diffuse optical spectroscopy and laser induced fluorescence spectroscopy [76]. All the statistics point towards Raman spectroscopy having higher sensitivity than experienced clinicians. An attempt to differentiate BCC subtypes using OCT had resulted in needing further information of the tumor constituents. However, the OCT and histopathology images possess similarities in terms of unorganized tissue architecture and clear inflammations but, to confirm the tumor subtype, only using OCT would require ultra-high imaging resolutions [17].

Patil et al. have tested an OCT-Raman setup under *in vivo* clinical conditions that had produced results confirming the feasibility of this combination in non-melanoma applications. Even though Raman imaging capability was missing in the setup as well as sample numbers differences had been identified between cancer and non-cancer regions. The common focus on non-melanomas was simply due to its high occurrences compared to melanomas. These types of tumors are responsible for structural damage in tissue even though metastasis is relatively slow. They may arise in the form of scars, ulcers and inflammations. BCCs generally consist of groups of unorganized basaloid cells at tumor centers. These islands are characteristically different from cells originating from the dermis and the changes in tumor content cause a clear separation between the tumor nucleoids and the surrounding tissue [77]. The presence of keratin and fibrous tissue may vary depending on the location and stage of the tumor and specific tumor types can be identified as nodular, superficial and infiltrating which have resulted in three distinctive types of BCCs.

In atherosclerotic plaque imaging, OCT has been well known and have already been used as a guided imaging tool in surgeries such as stent implantations [78, 79]. Catheters are utilized to enable the OCT fiber probe to reach the relevant locations and the procedure takes place under X-ray examination. Once the catheter is inserted until past the location of interest, it is pulled back at a constant velocity while rotating 360°. In doing so, the entire aorta is imaged within a few minutes. However, to obtain clear visualizations of plaques a blood free path is required. Therefore a contrast agent is administered via the catheter before the pullback begins. The image capture therefore must be time gated with the pullback motion. The strengths of OCT in this application involve the ability to acquire high resolution images with the required sensitivity. Due to the varying sizes of plaques, the limited penetration depth of OCT might not provide a complete image of larger or deeply embedded plaques [80]. The challenging task, however, is to distinguish between calcium and lipid rich plaque content.

Amongst the studies conducted on *in vivo* plaque imaging, the most common encounters have been ruptured, lipid rich, thin fibrous caps and calcified plaques. One study had quantified the amount of macrophages using OCT which can be correlated to the stage of the plaque [81]. The most important information extracted from thin fibrous caps is the thickness as it has a significant correlation to plaque vulnerability [79]. Even though thin fibrous caps and calcifications can be easily identified at later stages via OCT, early occurrences have been difficult to confirm [82, 83]. Therefore, combining OCT with Raman spectroscopy which can differentiate between specific chemical signatures would expedite the diagnostic procedure and promote better therapeutic interventions. Raman spectroscopy contains distinctive spectral features that identify calcium phosphate (960 cm^{-1}) and cholesterol/ cholesterol ester groups (~900 – 1100 cm^{-1}) [84]. There have been a few *in vivo* as well as *ex vivo* animal experiments investigated to conclude the presence of high- cholesterol rich diet induced plaques [85]. Moreover, postmortem aorta examinations have also increased the confidence of Raman spectroscopy in classifying atherosclerotic plaques [86].

Thus, OCT-Raman combination would enable cross-sectional images with corresponding chemical information which would promote early diagnosis and reduce death rates due to CVDs.

3.2 Device implementation

The implementation of SD-OCT and Raman spectroscopy was enabled via a probe cage consisting of optomechanical components from Thorlabs (OCTP-1300/M Adjustable Scanner, Thorlabs, Lübeck, Germany) that was mainly developed for the OCT system. This was modified to incorporate the Raman modality using additional dichroic mirrors that directed respective light paths to the sample and back to the detectors. Since the working wavelength range of the two modalities are quite wide apart, choosing the suitable objective lens was a challenge as they are mainly manufactured specifically for narrow wavelength ranges. However, in this chapter the principles behind the combination has been discussed along with the reasoning behind certain instrumental choices.

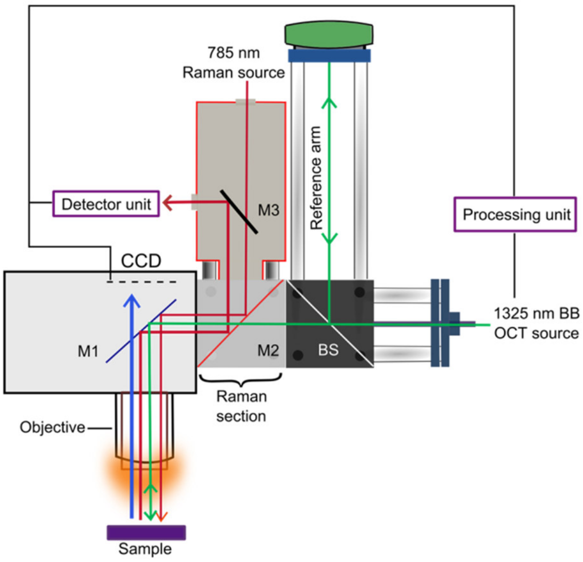

Figure 3.1: A schematic of the probe cage showing the OCT (green) as well as the Raman (red) beam paths. Adapted from [87]**.**

Fig. 3.1 shows the combined SD-OCT-Raman setup consisting of the probe cage where the control of beam paths has been achieved by dichroic mirrors M1, M2 and M3 at specific junctions where the beam paths cross. M1 represents two galvanometer mirrors (G1 and G2 Fig. 3.3) placed adjacent to one another, each directing the light beam downwards onto the sample. Each mirror scans in one direction, i.e. across X and Y directions, producing line scans over a specified FOV (max. limit= 10mm). One of the mirrors scan at a faster rate and both together provide a final area scan along with depth information. The CCD situated on top of M1, records microscopic images of the sample as the slower galvanometer mirror allows white light to pass while reflecting the rest. The incident beam paths of both OCT and Raman modalities must be coinciding spatially. This was achieved by adjusting the laser beam couplers of both Raman excitation beam and that of OCT at the entry point to the probe cage. Mirror M2 was inserted at a 45^0 angle with an alignment such that both Raman and OCT beam paths overlap (overlaid beam paths, green and red, in Fig. 3.2). It also allows the incident OCT beam to pass while reflecting the incident Raman light together with the back scattered Raman signal. Mirror M3 was aligned using a neon calibration lamp to achieve the highest collection efficiency (red beam path, in Fig. 3.1) as it is responsible for reflecting Raman signals into the collection arm where focusing optics couple the signal to the fiber core. This collection arm consists of a notch filter to remove any residual signals from the 785 nm laser as well as a focusing lens to couple the back scattered Raman light onto the collection fiber.

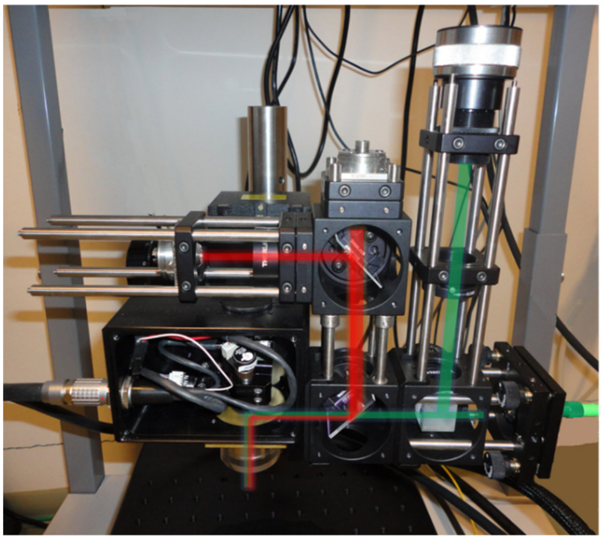

Figure 3.2. A photograph of the probe cage showing the Raman (red) and OCT beam paths (green) Adapted from [87].

To assist the visualization of the sample through the objective a dispersive ring of LEDs illuminates the sample through a wide area during measurement (Fig. 3.3) which assists in the sample alignment, positioning and OCT calibration.

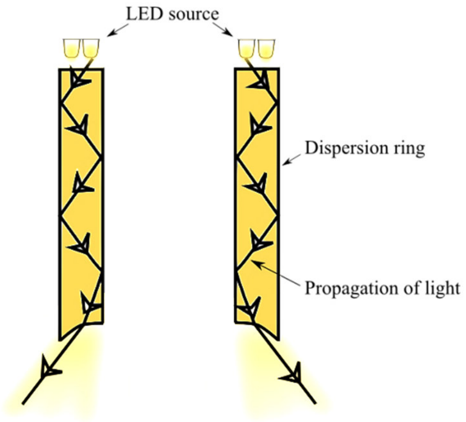

Figure 3.3. Cross section of the dispersion ring that was placed around the objective lens to illuminate the sample.

The intensity of this ring is adjustable and during Raman measurements the LEDs were switched off so as to avoid any interference with backscattered photons.

3.3 Scanning system

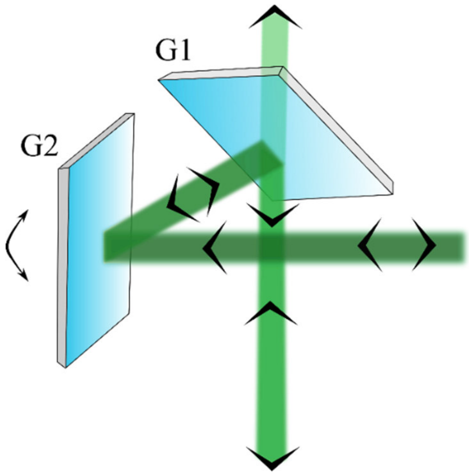

Figure 3.4: Galvanometer mirror scanning system. The green lines follow the path of the incident light rays.

This galvanometer mirror set (G1 and G2) has been housed underneath the CCD camera that records en face microscopic images of the sample. G1 transmits UV-VIS light reflected from the sample to the CCD camera situated in probe cage. The rest of the light is reflected to G2 and in turn towards M2 and other parts of the instrument. The total scan speed to acquire point scans (A-scan) can be varied between 5.5 kHz to 146 kHz. G1 moves at a slower rate in one direction as it reflects the light from G2 and the latter moves quicker in the other direction to produce line scans that span the entire field of view. Thus, each line scan produces a 2D cross-sectional image (B-scan) and a 3D volume scans (C-scan) have been constructed by a collection of B-scans as shown in Figure 3.5.

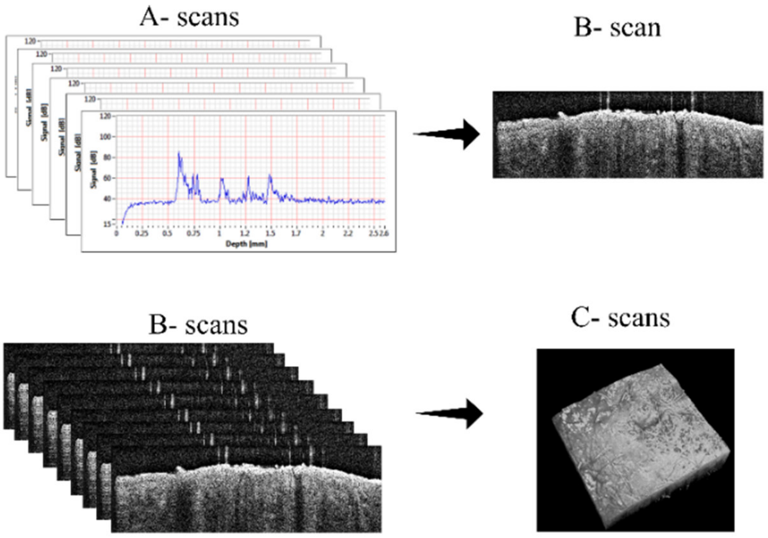

Figure 3.5: Definitions of A-scans, B-scans and C-scans in OCT shown using skin sample

3.4 Dichroic mirrors and alignment procedure

The dichroic mirrors are utilized to isolate light selectively with respect to the desired application. Those used in the combined OCT-Raman setup were all positioned at 45^{O} due to the design of the probe cage.

- One of the two galvo-scanning mirrors, G1 (AHF Analysentechnik, Tübingen, Germany) as shown in Figure 5.4 allows visible light ($\sim 350 - 650$ nm, blue arrow in Fig. 5.1) through to the CCD while reflecting $700 - 1500$ nm with a $> 93\%$ reflectivity.

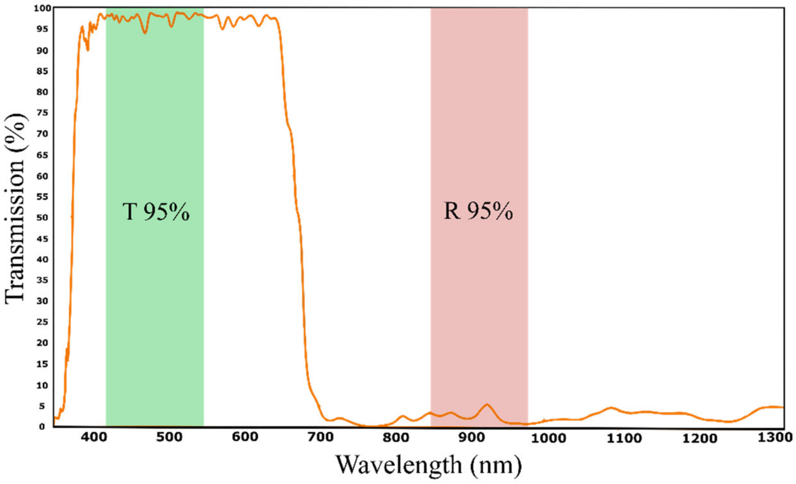

Figure 3.6: Galvanometer mirror G1

- M2 (AHF Analysentechnik, Tübingen, Germany) reflects the incident Raman beam at a 90^{O} angle towards the galvanometer mirror G2 as well as the Raman back scattered photons from the sample (750 – 1050 nm) towards the respective detectors maintaining an unchanged OCT optical path (see Figure 5.1).

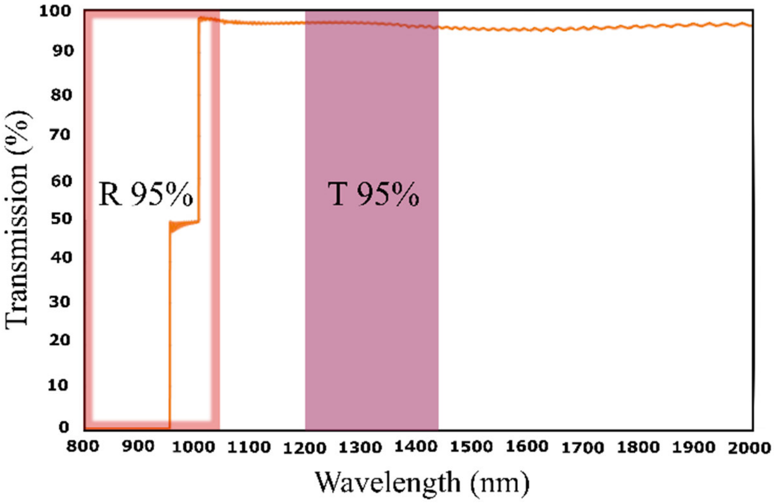

Figure 3.6: Transmission response of the dichroic mirror M2 at 45^{0}

As shown in Fig. 5.5, at a 45^{O} angle this mirror exhibits a small kink in its transmission response which results in a fair deformation of Raman spectra at around ~ 2700 cm^{-1}. This is further seen on Raman spectra shown in the Results section.

- The role of M3 (AHF Analysentechnik, Tübingen, Germany) is such that the back reflected Raman signals (750 – 1050 nm) are directed towards the detector while transmitting the incident Raman laser light. The profile of this mirror is the opposed to that of M2 with a high reflectivity in the range of 750 – 1050 nm.

The alignment procedure of the system involves controlling many parameters simultaneously. First, the OCT beam path was adjusted using the laser couplers such that the input OCT laser beam was collimated onto the optical axis of the beam splitter cube and the reference arm (green beam path in Fig. 3.2). Then mirrors M2 and M3 were inserted and aligned at a 45^{0} angle. Calibration of mirrors G1 and G2 was conducted by an inbuilt calibration software on ThorImageOCT and this step was carried out for each objective lens before any measurement. The reference arm length was adjusted according to the objective lens used and the reference arm power needed adjustment relative to the iris situated on the arm. This step was necessary to compensate for the different working distances in the objective lenses and the centering of the reference path length with the aperture. By adjusting the tilt of the beam splitter, the maximum intensity response was registered while the iris was fully open. Then, the opening diameter was gradually reduced while adjusting the beam splitter tilt-angle until the intensity variation shows the highest sensitivity to the aperture movement. After this step, the reference arm mirror was aligned until the surface of the sample was at ~ 3 mm on the axial scale as this position produced the least number of artifacts such as sharp intensity peaks in cross-sectional images due to the reflections from the sample surface. Moreover, this adjustment was necessary for the alignment of both axial foci of Raman and the OCT system that obviously needed to be overlapping. For the Raman counterpart, a pure powder sample of 1,4-Acetamidophenol was measured to achieve the highest signal intensity and the OCT reference arm was then adjusted to compensate for the axial distance mismatch.

The software that controlled the functioning of both modalities is based on LabVIEW. The data acquisition of OCT, Raman as well as the laser power were controlled by combining the already available OCT LabVIEW Software Development Kit with the LabVIEW components of the Raman spectrometer. OCT B- scans are stored in '.fits' format and by stacking the B- scans, a C- scan was produced using the 3D Viewer plugin on ImageJ. The Raman data are stored in '.txt' file format along with the coordinates so that the data localization would be feasible during data analysis.

In practice, the alignment was a challenge and the OCT and Raman beams were not overlapping spatially at the sample plane after the Raman system was optimized for the highest data quality achievable. This produced a discrepancy between both Raman and OCT laser spots which was observed on microscopic images. This issue was solved by measuring the difference in distance of misalignment (2.22 mm) and adding this parameter to the LabVIEW software so that the coordinates would be adjusted during the data saving process. Allowing this offset to persist would have caused a mismatch in our coordinate system and may even mislead the final statements.

3.5 The Raman spectrometer and SD-OCT system

The table below lists the specification of both the Raman and SD-OCT system with respect to different components such as laser source, detector and spectrometer specifications.

Table 3.1: SD-OCT and Raman spectrometer in terms of laser source, detector and spectrometer specifications. NOTE: For some measurements (porcine and system characterization), a Kaiser Raman spectrometer was used and these specifications will be mentioned on the relevant results sections.

Component	Raman system	SD-OCT
Laser source	785 nm narrow linewidth laser-MatchBox^{TM} from Integrated Optics, UAB. As the name suggests, the laser was as large as a match box.	Broadband super luminescent diode (SLD) with the central wavelength at 1325 with a bandwidth of > 100 nm.
Detector	Andor DU420A BEX2-DD configuration	Goodrich SU-LDH, digital high speed InGaAs line scan camera
Spectrometer	Andor Shamrock 303i in Czerny turner configuration with a grating 300 l/mm with a 3.4^0 nominal blaze angle.	Uses a linear-k spectrometer with a diffraction grating, and a prism for spectral dispersion.

The Raman spectrograph grating was aligned using the built-in motorized, indexed triple grating turret. The Andor CCD camera coupled with this spectrograph consisted of 1024 × 256 pixels and is a back illuminated, deep depletion CCD camera with fringe suppression and AR coating. Before any measurements, the detector was cooled to -60 ^{0}C and maintained at this temperature throughout.

The SD-OCT device used was also based on a spectrometer setup. Since it had acquired cross-sectional information all at once, Fourier transformation had been applied to produce the final 2D image from the interference patterns. Thus, the acquired signals needed to go through a post-processing step that may have costed a few seconds after measurement. During data processing, different contributions from the system was manipulated so as to extract the sample information and the signal quality in OCT was mainly governed by the scan speed and the detector readout rate. The acquisition rate of this OCT device ranged from 11 µs - 181 µs per A-scan. The OCT signal received via the single mode (SM) fiber contained a large contribution from the reference arm response which had been removed as a preliminary step in signal processing. Normally, the frequency of the reference signal was lower compared to that of the interference fringes of the sample thus isolating the reference signal was feasible. Another contribution received by the detector consisted of the DC component that represents those reflections from the reference mirror and the sample that do not contribute to the interference term. In addition, the autocorrelation term that originates from resulting interference between the different layers within the sample was another artefact present in captured OCT images. These two components had been filtered allowing only the cross-correlation term to be used for image processing which consisted of valuable sample and reference information. Reflections (with respect to SD-OCT) from the sample across the z-axis are given by the square of the Fourier component in k- space that magnifies even small amounts of detected photons. The detector itself had its own offset (part of the background) that shifted the spectrum axially up or down along the axis that had been subtracted as well. Even though axial resolution is governed by the spectral bandwidth, during the Fourier transform step the resulting side lobes can cause spectral leakage. With biological samples, the acquired spectrum was never smooth due to non-uniformities in scattering by the different cellular organelles. Large back scattered signals can produce large side lobes that reduce the axial resolution. Since it was difficult to estimate the input frequencies accurately a window-function had been chosen as a precaution which had been then multiplied with the spectral response. In our SD-OCT system, a Hann window was applied (also known as apodization). These processes were part of the deconvolution method where the relevant interference patterns were extracted from the interferogram.

3.6 Objective lens

In terms of the working wavelength range of the combined system, both OCT and Raman spectroscopy were far apart as they functioned at 1325 and 785 nm respectively. While deep tissue OCT imaging requires objective lenses with a rather low numerical aperture (long working distance), Raman spectroscopy requires relatively larger numerical apertures to achieve higher collection efficiencies. The perfect objective lens for combining OCT and Raman measurements would be always a compromise for both modalities. However, an anti-reflection (AR) coating and transmission wavelengths from 700 – 1500 nm are advantageous properties to have. Initially three different commercially available microscope objectives specially designed for OCT imaging systems were tested and detailed information can be found in Table 3.2.

Table 3.2: Details of the telecentric objectives LSM02,-03 and -04 line from Thorlabs.

LSM02	**LSM03**	**LSM04**
f= 18 mm, NA= 0.11, magnification of 10x, working distance 7.5 mm	*f*= 36.0 mm, NA= 0.056, magnification of 5x, working distance 25.1 mm	*f*= 54.0 mm, NA= 0.037, magnification of 3x, working distance 42.0 mm.

Two more objective lenses were also tested: Mitutoyo M Plan Apo NIR Infinity Corrected Objective (5x, NA=0.14, Edmund Optics, US), as well as an achromatic doublet lens with AR coating (diameter = 25mm, *f*= 35mm-NIRII, NA= 0.36 Edmund optics, US).

The testing criteria included optimum Raman intensities, low fluorescence backgrounds and clear OCT images. The three LSM objectives are telecentric, which had ensured minimal image distortions (for e.g. due to the varying thicknesses throughout the different areas of the objective) and a constant image resolution due to the spot size behaving evenly on flat image planes during scanning. For this same reason, the probe head was calibrated for each objective prior to the measurements. In addition, the OCT reference arm length was adjusted each time the objective lens was changed. The final objective lens testing process had included the application of the mentioned objectives on a porcine sample that had produced results proving the superiority of the achromatic doublet lens from Edmund Optics for this particular system.

3.7 Integration into the medical cart

Before introducing the system into the clinics, all the instrumental components were integrated onto a medical cart (WISAP® medical technology, Brunnthal, Germany) for ease of mobility thus further complying with medical standards (see Fig. 3.9). This provided the freedom to move the system without affecting any aligned optical components. In clinical settings, this feature had been very useful as it was transported many times via the elevator to different departments without any internal misalignments. As the system was built for clinical use, stability and mobility were two essential features that it needed to fulfill. Therefore, the instruments were kept on slip-free rubber sheets/ double sided tape and the CPU was well bound to the cart by a harness. After moving the system through elevators and corridors, the alignment and instrument positions had not fluctuated while transportation.

Since Raman spectroscopy is light sensitive, the probe head and the spectrometer were light proofed by covering the shelves that they were housed in, with light blocking material. A coverage of two layers of the light proofing material surrounding the probe head as well as the Raman spectrometer were required for the complete omission of ambient light. The material was held via Velcro adhesive tape over the shelves and access to the probe cage was enabled by magnetic stripes glued onto the openings). This allowed for quick and flexible light proofing with easy access to the probe cage.

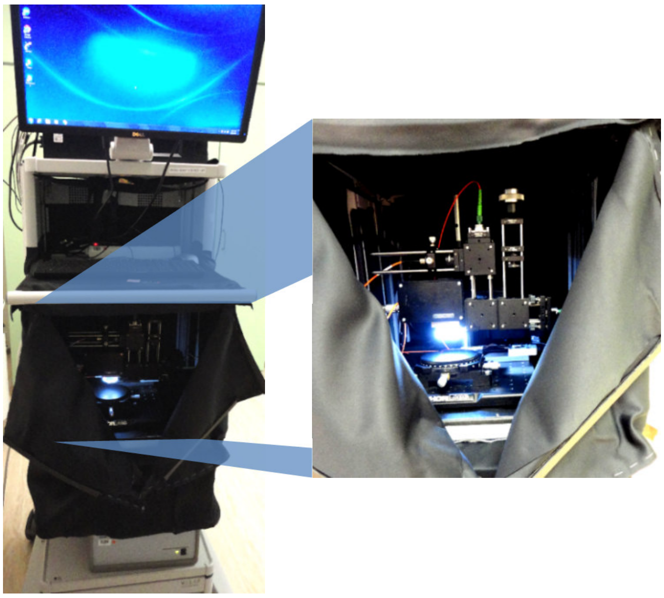

Figure 3.9: Integrated OCT- Raman system on the medical cart. A zoomed photograph of the probe head chamber is shown as an inset.

A probable issue with combining two modalities would be the combination of data acquired in the z- axis (depth). Khan et al. [88] had measured a phantom as well as biological tissue with layered structures. Since their system was a confocal Raman system and the FOV was 10 folds smaller than that of our combined OCT-Raman setup, depth localization was possible. However, there would be many challenges if their system were to be applied in clinical conditions as the OCT images collected would need to be larger along with impeccable image quality for the clinicians to diagnose with the 2D scans of tumor regions.

Besides the data correlation, the most challenging task in terms of the equipment had been the choice of a suitable objective lens. Since the device combines wavelengths ranging from 785 to 1325 nm (a difference of 540 nm), opting for a commercially available objective lens would have required the exchange of the light sources so that the difference in wavelengths would become smaller. However, this would have depleted the device performance drastically. In terms of the refractive index (NA) Raman spectroscopy requires a higher NA than OCT as it increases the probability of back scattered photon detection. The desired NA for this would be a value close to ~0.9. On the other hand to achieve good lateral resolution with OCT imaging, a lower NA objective would be required [13]. The used combination of wavelengths fulfill high axial resolution (OCT) and results in low fluorescence background (Raman spectroscopy). Since the wavelengths of the systems were ideal for the application, there should be a solution in terms of the objective lens, which was why a compromise had been made. In the method presented by Mahadeven-Jansen's group, single spectra had been collected from the axis of the objective, which had not produced any artefacts at the edge of the FOV. Since our strategy included a scanning method for both OCT and Raman spectroscopy, the effects of the objective lens was observed.

The reasoning behind choosing these wavelengths relates directly to light-tissue interaction principles. Using wavelengths in the UV region to measure Raman bands would result in doubled fluorescence especially when investigation biomaterials. A large fluorescence background can mask the Raman response even though theoretically, it would provide a better SNR and stronger Raman scattering. Those wavelengths larger than 785 nm, such as 1064 nm which has been used very commonly with tissue sections, would reduce the fluorescence response significantly. However, this effect is coupled with reduced Raman scattering efficiency, which is inversely proportional to the wavelength i.e. λ^{-4}. Since our application on non-melanoma skin cancers had large time constraints, utilizing a 1064 nm laser source was not possible. A workaround for using the advantages of 1064 nm would be to implement a real time diagnosis based on Raman and OCT images that would cut down the waiting period for patients. The more common silicon CCD detectors would need to be replaced with an InGaAs one as the former becomes insensitive above ~1000 nm.

In terms of the OCT laser wavelength, using wavelengths lower than ~1000 nm would have reduced the quality of data and would result in sacrificing the penetration depth. This is because at longer wavelengths, especially at the 'tissue optical window' light is able to penetrate the tissue surface. The limit of transparency would be reached by water where vibrational absorption dominates at 2500 nm. Furthermore, longer wavelengths have less multiple scattering events as they enter tissue which promotes more scattered photons. In contrast, only a tissue transparency less than a 100 µm would be reached with lower wavelengths as the photons would lose their energy quite quickly. For example, Evans et al had applied a combined OCT-Raman system to measure bovine retinas [36] since the primary application of OCT had been to investigate retinal health. Their setup consisted of a Raman excitation wavelength of 633 nm and an OCT counterpart at 855 nm. The different layers that built the retina was relatively thin that the penetration depth of the OCT excitation laser was sufficient to visualize the structures. Even though their results achieved very good OCT 3D images, the Raman spectra were dominated with noise and therefore had poor signal to noise ratio (SNR).

In our application, improvements to the software would be required to achieve a smoother workflow. Firstly, multiple prompts must be implemented so that the user would not miss any important saving steps. The detector configurations must be embedded into the system that will not allow the user to access or change them. For further clinical applications with this device, a more robust software application should be developed with better computational power to be able to view 3D images collected by OCT. The images that had been collected were post processed by ImageJ.

The next section presents the experimental results carried out to obtain system characteristic followed by the preliminary results on commercially available pork samples.

3.8 System characterization

3.8.1 Measuring system resolution

For the OCT counterpart a roll of scotch tape was used to measure the axial resolution. In this simple experiment the adhesive layer between consecutive tape layers were measured and it was found that the value stayed constant at ~ 10 µm with the different objective lenses used because the axial resolution only depends on the source bandwidth and the OCT- spectrometer resolution.

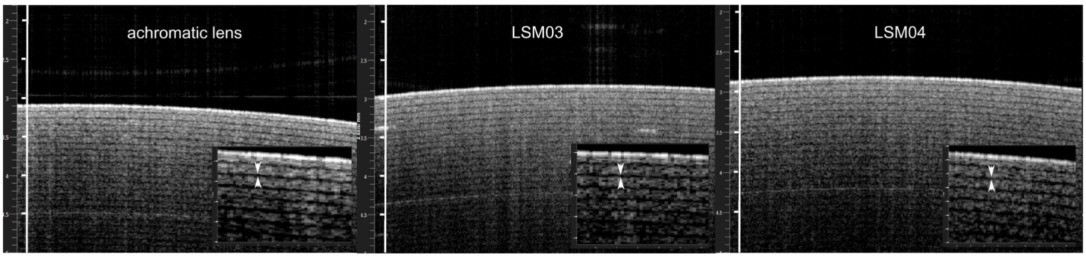

Figure 3.10: Axial resolution images measured using scotch tape to compare the three objectives in question. Insets at the bottom right corner show the distance of the glue between the tape layers which was measured to be ~ 10 µm (white arrows). Adapted from [87]

The lateral resolution was also characterized using a 50 µm thick tape that was placed on a glass slide assuming that the tape has a straight edge. Resulting mismatch between the distance of the proximal and distal surfaces of the tape was found to be approx. 13 µm (Fig. 3.11 A).

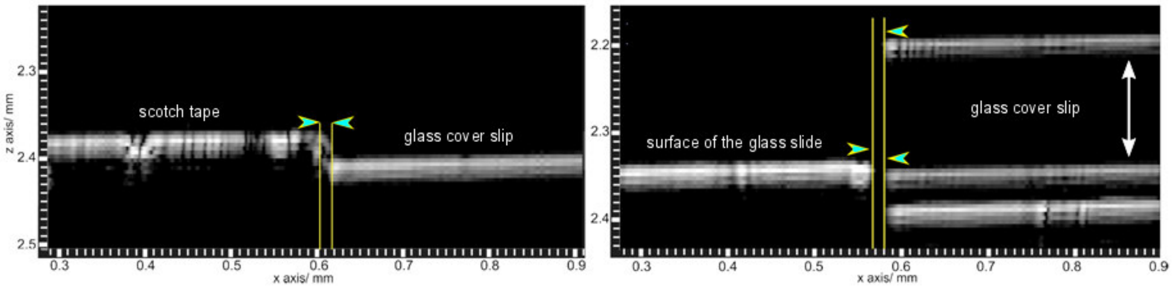

Figure 3.11: OCT images of scotch tape (left) and a glass cover slip placed on a glass slide (right). The mismatch of the proximal and distal surfaces was found to be 13 µm in both cases. Adapted from [87]

To further confirm this finding, a cover slip was placed on a glass slide and line scans were measured across the edges using OCT. This resulted in the same mismatch as earlier (Fig. 3.11 B).

In order to characterize the Raman imaging counterpart, a raster scan was performed on a Teflon layer with a scanning step size of 20 µm, mapping a region of 20 × 500 px. The Teflon layer was taped over a quartz slide and measured across the edge. At a representative Raman peak at 338 cm^{-1}, the intensity variations were recorded. To quantify the changes, the peak area was plotted with respect to the measured distance. The lateral resolution was thus defined as the distance between the intensity change between 10% and 90% of the integrated peak (area) as shown in Fig. 3.12 A. The achievable resolution was 104 ± 6 µm which was in fact in good agreement with the core diameter of the Raman excitation fiber (Thorlabs, M43L02, NA=0.22).

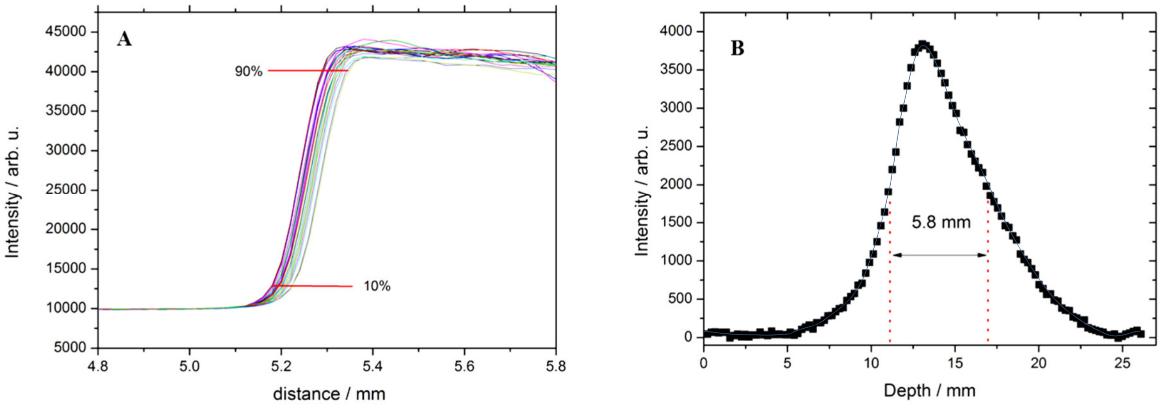

Figure 3.12: Lateral resolution (A) measured across a teflon tape (peak at 338 cm^{-1}) and axial resolution (B) in air using scotch tape (peak at 493 cm^{-1}). Adapted from [87]

As for the depth of focus of the Raman excitation laser light a transparent scotch tape was used. The tape was wrapped around a metal slide that contained a wide opening. Therefore by changing the Raman focus across the z-axis, within a height of 27 mm only the material itself was measured. After recording Raman spectra at each 0.225 mm, an intensity variation graph was produced by integrating the measured peak at 493 cm^{-1}. The depth of focus was then calculated as the FWHM of this intensity profile (Fig. 3.12 B) that was calculated to be 5.8 mm. This observation was the result of measuring in air as it is vital to consider the refractive index of the sample when calculating depth of focus. In biological samples the refractive index is generally 1.4 and which results in a depth of focus of about 1 mm for the 785 nm wavelength used. In conclusion, our investigation resulted in a Raman spot size with a lateral resolution of ~ 100 µm and 700- 1000 µm axially in tissue [87].

3.8.2 The choice of objective lens

There were many criteria that needed considering when testing different objective lenses for our application. Our systematic approach was to pick the most suitable objective lens from the LSM series from Thorlabs and then compare that with the other two objective lenses in question. Despite having the highest numerical aperture (see Table 3.2) from the entire LSM objective lens series (Thorlabs), LSM02 only transmitted 10% of the Raman signals. LSM03 on the other hand produced its own Raman signal that masked any sample signals leaving LSM04 as the most appropriate option amongst the series. As the next step, the SNR was compared between Mitutoyo, LSM04 and Edmund Optics achromatic doublet lens using a reference sample i.e. a pure powder sample of 1,4- Acetoamidophenol. As shown in Fig. 3.13, the achromatic doublet lens demonstrated a far superior back scattered Raman signal as well as a lower fluorescent background compared to Mitutoyo and the LSM04 objective lens. Out of the LSM series, the latter had the best signal output. For this measurement, the RAMAN RXN1 (Kaiser Optical Systems, USA) spectrometer was used with a 785 nm multimode laser source, Invictus $^{\text{TM}}$ (785-nm NIR laser, Kaiser Optical Systems, Inc.). This setup included a *HoloPlex*, holographic transmission volume grating and an ANDOR iDus 420 BB-DR CCD camera. All spectra were measured at the same laser power and integration time.

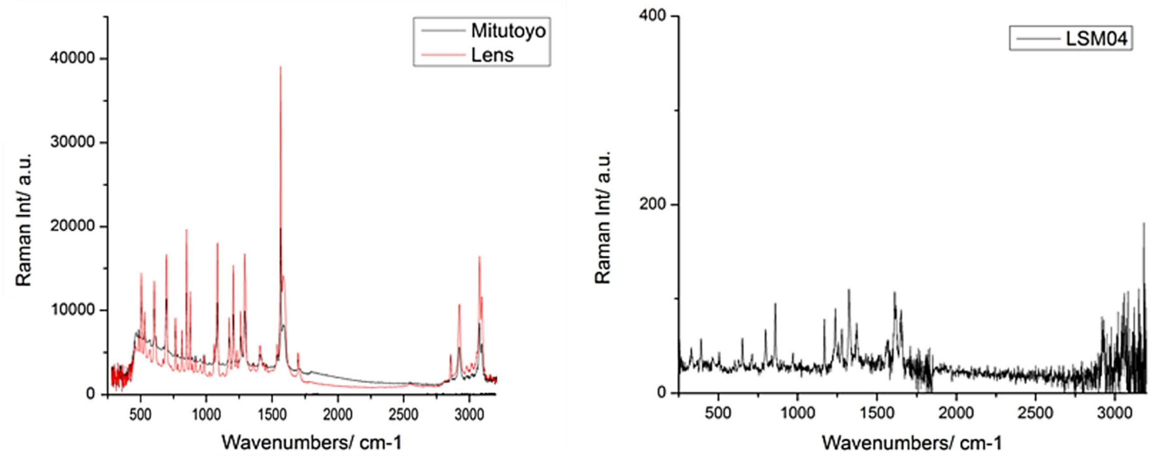

Figure 3.13: 1,4- Acetoamidophenol measured using Mitutoyo objective (left, black), Edmund optics lens (left, red) and LSM04 (right).

Another criterion that needed to be considered was the alignment of the main optical axis of the objective lens with the galvanometer mirrors so that the OCT calibration would be accurate. The diameter of the objective lens must be at least 6 × 6 mm to align with the galvo mirrors. Otherwise the system calibration would not proceed to completion due to blocked beam paths. Mitutoyo had a smaller diameter that cut out nearly 50% of the images proving it unsuitable.

3.8.3 Application on biological tissue

A complete overview of all the objective lens (LSM03, LSM04 and achromatic doublet) performance was investigated by carrying out measurements on biological samples. Commercially available pork loin samples (~1 cm thick) consisting of bone, fat and muscle tissue were chosen. A ~50 × 50 mm piece was carefully extracted using a scalpel and was placed on a petri dish for measurement. For each objective lens, a fresh sample was used as it would lose its moisture throughout the measuring process.

First, with the achromatic doublet lens, a microscopic image was recorded with a 10 x 10 mm FOV utilizing the CCD situated on the probe head followed by a C-scan using the ThorImageOCT software (Fig. 3.14 I and J). The surface C-scan shows more detail that cannot be shown by a magnified VIS image even though the eye can differentiate bone, fat and muscle by the color. Since the OCT image has not been color coded to represent the corresponding regions it would be impossible to distinguish between muscles, fat and bone by only inspecting OCT images.

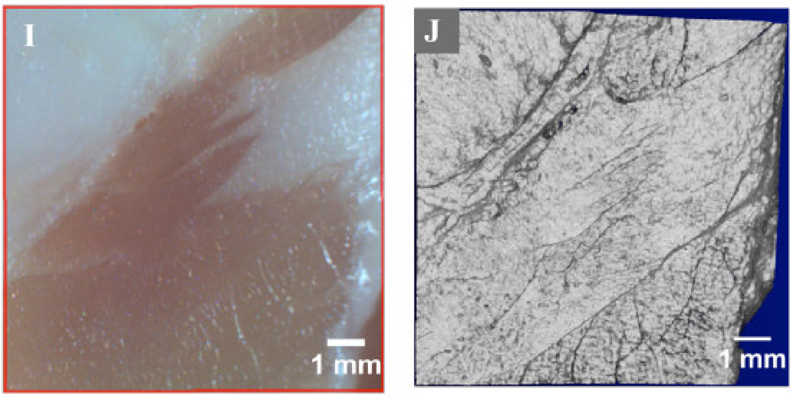

Figure 3.14: Microscopic image (left) and the corresponding surface C-scan of a pork loin sample. Adapted from [87]

Then, without moving the sample position, a Raman map (100 × 100 pixel size) was measured with an integration time of 1 second and ~40 mW laser power at the sample plane. Fig. 3.15 K shows the Raman map and Fig. 3.15 L shows the mean spectrum of each cluster after data analysis. Pre-processing steps of the Raman map include wavenumber calibration using 1,4- acetoamidophenol, a baseline subtraction via the SNIP algorithm [89] and followed by vector normalization. For the analysis step a k-means cluster analysis with $k = 5$ was applied to identify spectral variations within the sample.

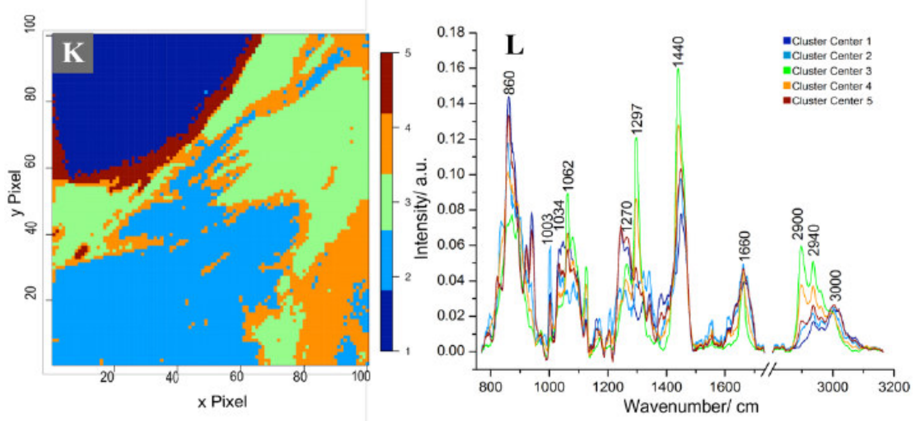

Figure 3.15: Measured Raman map (K) and results from the k-means cluster analysis (L) showing spectra representing each detected region.

With the achromatic doublet lens, only a transmission loss of 10% of the laser power was observed as seen by the signals in Stokes Raman region between 785 – 1050nm. This is also reflected upon the cluster images (Fig. 3.15 K) where all tissue components have been separated spectroscopically including the tissue transition regions. Cluster 1 (dark blue) represents bone whereas bulk fat has been identified by cluster 3 (green). The representation of bone by the first cluster was further confirmed by the lowest signal recorded at the longer CH stretching region (~2800 – 3000 cm^{-1}). Cyan (cluster 2) identifies the muscle regions on the sample but it is clear that the margins between each tissue type contain another type of tissue. It has been concluded that they consist of a mixture of both tissues which cannot be seen on either microscopic or surface OCT images. Since our system is not confocal the spectral features are mixed and hard to pin-point by eye. The 3D surface images obviously contain information from the entire scanned area, which can be manipulated to obtain further depth information to investigate the structures beneath the surface. Since the shape of the Raman spot is oval in shape i.e. elongated in the axial direction, the depth correlation of the data has not been possible which would be very useful as the accuracy of the results would increase. Confocal setups were not considered since the FOV would be limited and the time taken for measurement would be large for our application.

The measurement procedure was repeated with the LSM03 and LSM04 objective lenses. The corresponding microscopic, surface 3D OCT, Raman map and the result of the k-means cluster analysis images are shown in Fig. 3.16.

LSM03- 3x

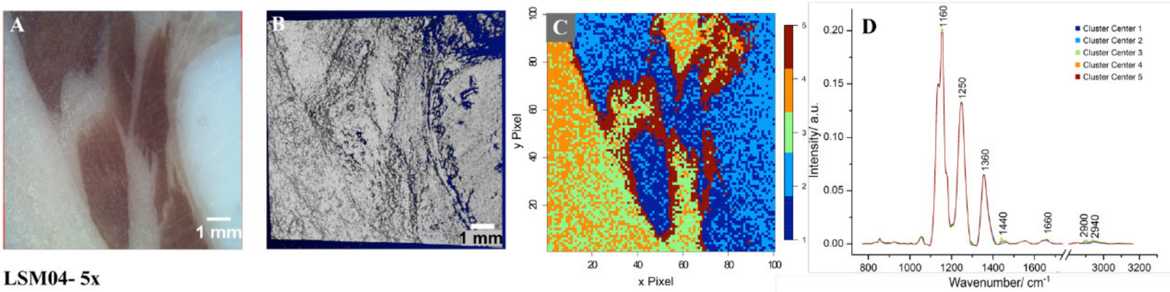

LSM04- 5x

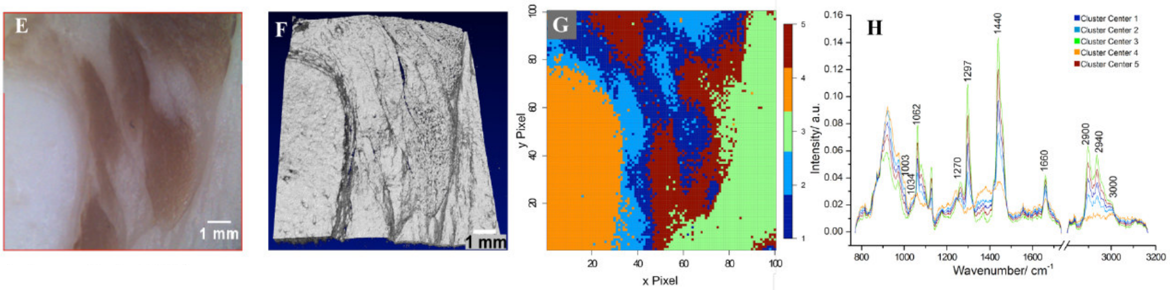

Figure 3.16: Comparing LSM03 and LSM04 by measuring pork loin samples. The first row (A, B, C and D)consists of the microscopic images of the sample area, the OCT C-scans seen from surface and the k-means cluster images derived from the Raman raster scan of the same area, respectively. The second row shows the same but with the lens LSM04.

The Raman spectra collected via LSM03 resulted in large bands at 1160, 1250 and 1360 cm^{-1} most probably due to the optical glue within the lens material itself. Therefore, the clustering resulted in poor differentiation of spectra with cluster 1 and 2 that merged bone and muscle, 3 and 4 denoting bulk fat while cluster 5 the fat-muscle margin. In terms of the OCT imaging, as Fig. 3.16 B, shows the image seemed to be thinned down. This is an after effect of adjusting the contrast after image acquisition, which had been applied to all the 3D OCT images. In contrast, LSM04 displayed only a smaller Raman contribution thus resulting in more sample specific signals. The SNR at 1440 cm^{-1} was 64.3 with just 25% of the excitation laser power that might have corresponded to a low numerical aperture.

Since the OCT calibration software has been specifically developed for the LSM objectives, the OCT calibration process did not perform too accurately with the achromatic doublet lens. This is because the OCT calibration process seemed to have worked by detecting the reflected light from the metal calibration sample that was provided upon purchasing the OCT device. Therefore, the reflected light captured by the achromatic lens had not been optimal for an accurate calibration, even though the calibration procedure was completed. Everything considered, it has the best compromise between the quality of Raman spectra and OCT images. The SNR of 248.5 achieved with the doublet lens is 4 times better than the SNR obtained with LSM04 at 64.3.

3.8.4 Preliminary measurements on pork skin

A pork skin sample with a pigmentation was chosen to investigate the morphological changes via the combined OCT-Raman system. The reason behind choosing a pork skin sample is due to the proclaimed similarity to human skin [90]. Similar to the measurement procedure with the pork loin sample previously, a microscopic image of the region of interest was captured after which an OCT C-scan was performed. As Fig. 3.17 B suggests the area above the red dotted line consisted of the pigmentation whereas the tissue below was of normal tissue.

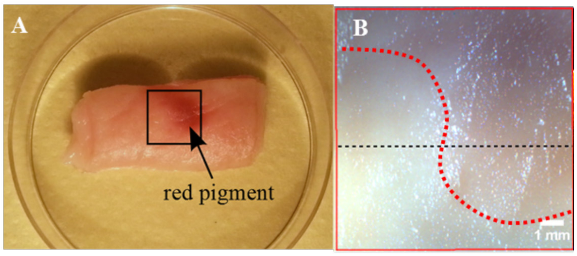

Figure 3.17: A photograph of the red pigmented region on a pork skin sample is shown in A and a microscopic image (B) shows the clear separation between the pigmented region and the normal region indicated by a red dotted line. The black dotted line on B was the OCT B-scan was conducted. Adapted from [87]

There was a slight intensity variation observed on the microscopic image and this must have been due to the cut-off wavelength at 650 nm of the dichroic galvo mirror. This uneven illumination could also be a circumstance of the poor OCT calibration due to the achromatic doublet. Nevertheless, the OCT images represent the usual skin layers with a disarrangement of tissue structure where the red pigment was located. The black dotted line on the UV-Vis image (Fig. 3.17 B) corresponds to the cross section of the measured OCT line scan (Fig. 3.18).

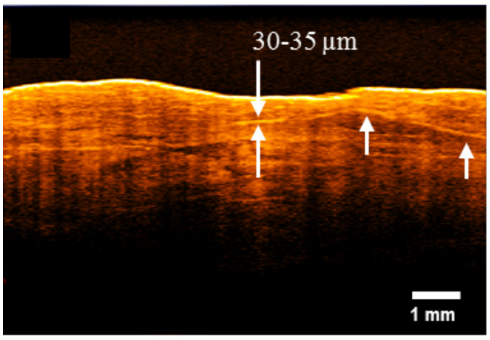

Figure 3.18: shown in C where the red pigment is observed as a hemorrhage within the skin layers and it is a size of 30 – 35 µm. Adapted from [87]

The normal structure of pork skin was not observed probably due to the cleaning/sterilization processes that are being carried out commercially. However, an inclusion between the tissue layers has been observed as indicated by the white arrows on the OCT image (Fig. 3.18). This abnormal feature had a thickness of about 30-35µm which was measured with OCT.

In order to extract spectral information 10 spectra from each region i.e. pigmented and normal were collected with Raman spectroscopy using an integration time of 1 second. Since the depth of focus of our Raman laser spot is about 1 mm, the measurements would consist of molecular information from these depths. Fig. 3.19 shows the mean Raman spectra of the pigmented and normal spectra which are overlaid after the data had been base line corrected and normalized.

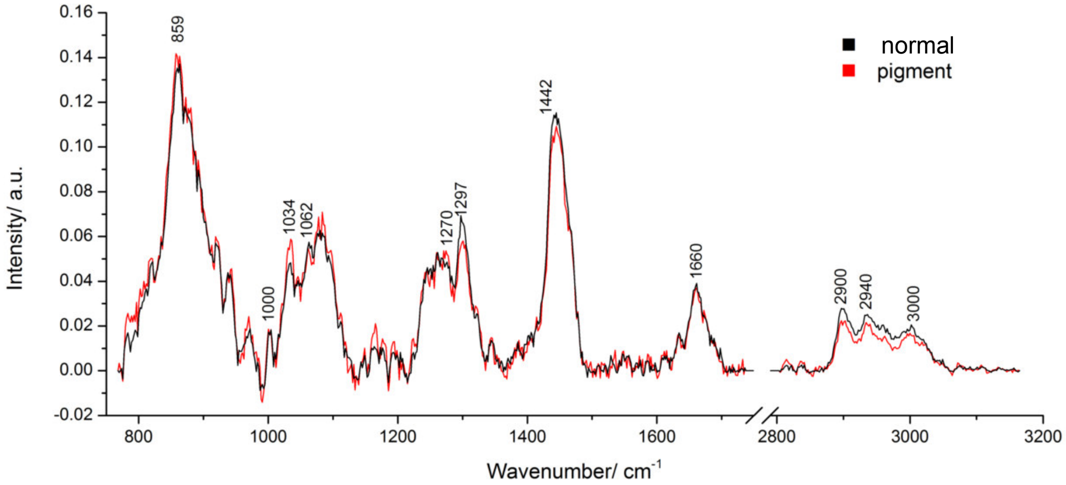

Figure 3.19: Mean Raman spectra from the pigmented region (red) and the unpigmented ('normal') region (black). Representative Raman peaks are labelled.

The main differences observed here have been mostly in Raman intensity of specific peaks. These peaks are C-H related and observed at 1298, 1443 and 2850- 3000 cm^{-1}. As expected Raman spectral band of skin were present at 1660, 1270, 1030 and 1000 cm^{-1}. Even though, it was suspected that the red stain was a subcutaneous hemorrhage no heme-groups were visible in the Raman spectra. This could be due to the relatively small size of the hemorrhage compared to the area of back scattered photons collected from healthy tissue. In addition, the spectra collected were noisy and identifying heme related peaks would be challenging by eye. Therefore, further studies would need to be conducted under same conditions to have a larger sample set.

This chapter has presented detailed information on the system development, characterization and the results from the different objective lenses carried out on 4 pork loin samples. Thus, a thorough understanding of the limitations in terms of performance and the spectral response have been identified. The achromatic doublet lens, that had the least transmission loss and had not produced an inherent Raman spectral response, was clearly the best option for our application. With this objective lens, a clear differentiation of tissue types was achieved with the help of k-means cluster analysis. Clear microscopic images of the samples and detailed B- and C- scans were obtained that were correlated to Raman spectral features.

The main aim of investigating the system parameters was to confirm its suitability for the application on human skin samples and therefore, both axial and lateral resolution of both the modalities were measured. OCT was able to resolve ~10 µm axially and 13 µm laterally. Considering the tissue features that needed to be resolved, these values were suitable for investigating skin tissue. Concluding the optimal conditions for Raman measurements were not straightforward. Since the incident laser beam experiences scattering and absorption when interacting with tissue layers, the measured axial resolution (~5.8 mm) was not representative. In tissue this would be reduced to 700- 1000 µm [91]. Our system not being confocal allowed the detection of spectral response from a larger area within the tissue, but with poor axial accuracy. Scanning tissue axially with a confocal Raman system would cost more time but would provide highly localized depth information, which may be useful in *in vivo* diagnosis as well as during tissue biopsy. This limitation was observed first hand during the pork skin pigment investigation. It was concluded that the amount of hemorrhaging was too small (~35 µm) compared to the amount of normal skin that was present in the measured Raman cross section. However, differences were observed with OCT scans as a darker inclusion between tissue and distinct intensity variations in Raman spectra.

4 Results and discussion

Having demonstrated that the combined OCT-Raman system provides convincing results in tissue visualization and spectroscopic differentiation, a pilot clinical study has been initiated in collaboration with the SRH Wald-Klinikum hospital in Gera, Germany. Furthermore, *ex vivo* atherosclerotic plaques, both human and animal, were investigated in order to observe the system performance and capabilities. *In vivo* animal experiments were then conducted using separate systems, as a proof of principle. Here, the Raman spectroscope used was previously described, i.e. Raman RXN1 (Kaiser Optical Systems, USA), and the OCT system was a commercially available device (St. Jude Medical, US). This chapter focuses on the measurement protocol, system performance and the quality of data in all three applications.

4.1 A pilot clinical study

The main goal of applying the OCT-Raman system in a skin cancer study was to test the feasibility in differentiating *ex vivo* non-melanoma skin cancers as well as the overall applicability in a surgical environment. As expected, many types of cancers were included in the patient pool as it was impossible to identify the diagnosis without an H&E stain. The patients were informed of the experiments beforehand and an agreement was signed which had gone through an ethical vote. The main focus was on BCC tumors as their prevalence is high compared to other non-melanomas [92]. Moreover, the Raman spectral quality of BCC tumors compared to other met tumor types enabled a better correlation between microscopic, OCT and Raman images. According to the histopathologic outcome, the BCC samples were handpicked and used in the data analysis.

Sample preparation: Skin samples were extracted by a surgeon using a scalpel. Each time their size and shape varied such that the diameter of the samples ranged between 3 – 15 mm depending on the location of extraction. After careful extraction the samples were placed on a gauze and was handed over for OCT and Raman measurements.

The OCT-Raman device was initialized well before the beginning of the biopsy as the detector required cooling which took a few minutes. The instrument was placed in the adjacent room, next to the operating theater. The samples did not require any cooling. Initially a few drops of saline were added onto the surface of the sample to avoid any drying during measurement. The saline was only added onto the gauze to supply some moisture that would avoid any drying effects during measurement. The total time required for both OCT and Raman spectroscopy measurements was only

12 minutes per sample and within this period no significant drying had occurred that could mislead the diagnosis of the pathologist. After the measurement, the samples were immersed in a vile of formalin and transported to the pathologist for H&E sectioning.

A total of 18 patients were involved in this study with 28 being the total number of samples. After the first 8 patients there was a change in the system settings and alignment. (Note that the 8th patient was not included in the study as the OCT image acquisition was not recorded successfully). Therefore, the first 7 patients (8 samples) were analyzed separately and those samples were diagnosed to have BCC, SCC and pre-cancer types as shown on Table 4.1 (even though the main focus was on BCC).

Table 4.1: Summary of the first 7 patients and related information. The sample highlighted in green has been presented in detail later (Fig. 4.1)

Patient no.	Region of extraction	No. of samples per patient	Diagnosis-pathologist	Microscopic image
01	Face	1	Superficial BCC	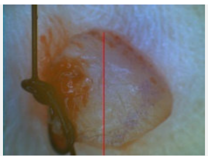
02	Face	1	Partially eroded partially keratinized BCC	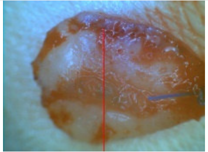
03	Back	2	Hyperkeratosis (sun exposure) Nodular BCC	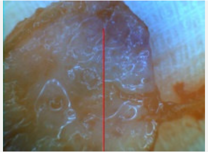 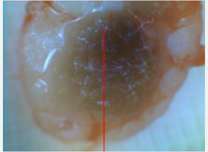
04	Face	1	Partial superficial minimal BCC	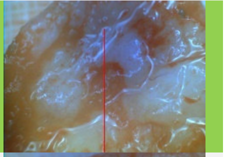
05	Face	1	Multifocal superficial BCC	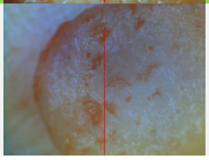

06	Face	1	Partially eroded superficial BCC	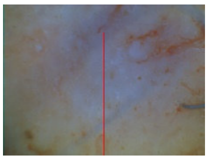
07	Back	1	Solid BCC	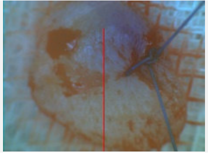

The system change involving the use of a fiber with a smaller diameter made the system alignment very sensitive at a cost of the signal-to-noise ratio and did not improve the subsequent data analysis. At least half of the samples had a too high fluorescence background which hindered a detailed analysis.

Data analysis: The Raman spectra shown in Figure 4.1 D, are that of the fingerprint region since the high wavenumber regions did not contain any useful spectral features. The lower wavenumber region had a system background response that had distorted any usable spectral information. This background response consisted of fluorescence and an etaloning filter function that had been reduced with the background correction algorithm [89] and Savitzky-Golay smoothing, respectively. With a simple clustering method as k-means, a distinguishable separation between diseased and normal tissue was achieved.

Results and discussion: The collected results were compared with one another for correlation. OCT images (B-scans and C-scans), Raman spectra and images of H&E stains of the sample from patient #04 (highlighted in green on Table 4.1) are shown in Figure 4.1.

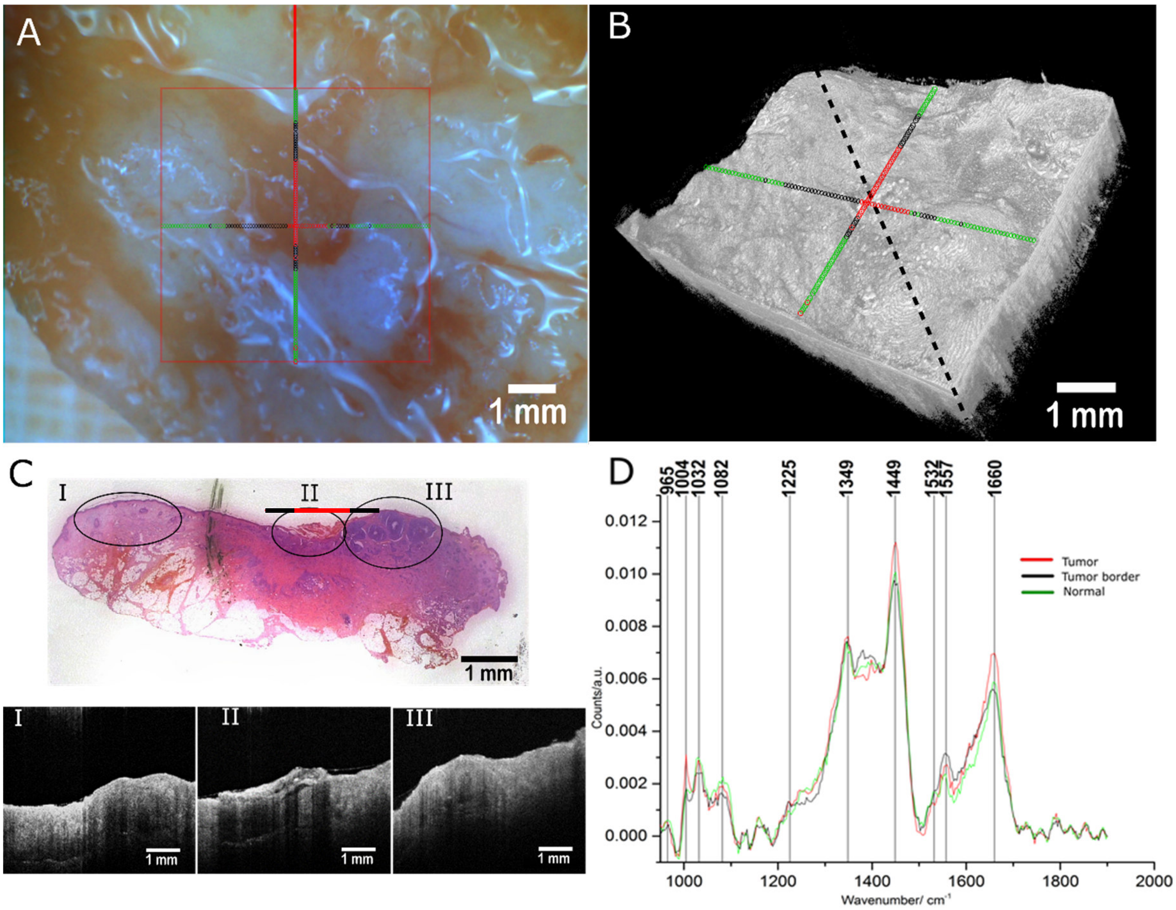

Figure 4.1: Comparison of OCT and Raman results obtained from a BCC skin biopsy. The microscopic image (A) of the sample has been overlaid by Raman spectral measurements (1 sec. integration time per data point). This can be seen on the C-scan in image B as well. The approximate region where the H&E cut has been made has been shown by the dotted line on the 3D volume. From the OCT image slices (B-scans) across the sample, the features observed on the H&E slice were matched as shown in C. The Raman spectra collected from the vertical and horizontal axes were analyzed using k-means cluster analysis and the corresponding spectra have been shown in D.

The sample shown in Figure 4.1 A was extracted from a region on the face and the microscopic image, which provides an *en face* view of the sample, revealed the topology of the skin surface. The red square, overlaid outlining the Raman measurement spots on both x and y axes, shows the FOV of the OCT measurement. A closer look at the diagonal of the image would display the vascularization where the bulging regions were situated. This may be a result of the local inflammation caused by an accumulation of lymphocytes. An abnormal redness in the mid region of the FOV was diagnosed by the pathologist as partial superficial minimal BCC (Table 4.1). This specific sample was one of the exceptions that showed the presence of tumor on the microscopic image. In many instances, the tumor had been submerged or not confined to a certain region due to the physiology of BCCs.

The OCT C-scan of the sample (see Fig. 4.1 B) exposes the topographic details and it has been tilted for better visualization. This image has been overlaid by the Raman data points to show the location of the Raman line scan. Since the H&E slices had not coincided with the exact OCT cross sections only an approximate comparison was achieved between the H&E image and the OCT B-scans. The recorded resolution of 13 µm was sufficient to visualize the relevant topographic features. The 800 2D OCT scans were accessed separately and with careful inspection, three OCT 2D scans were found to correlate with the histology observed on the H&E stain (Fig. 4.1 C). Concerning the Raman spectra, only the tumor and tumor borders were identified on the H&E stain as shown with the corresponding colored line (red and green, Fig. 4.1 C). However, the three B-scans have depicted the information matching those circled in Fig. 4.1 C I, II and III. Tumor granules can be clearly seen in C I and the flaky surface texture of the lesion in C II. Shadowing from the epithelium had resulted in obscured images of the dense collection of the cells beneath the surface. However, this feature was found on another B-scan in the data set. The relatively large tumor nucleoids (Fig. 4.1 C III) were found at a depth of 1 mm which was confirmed by the B-scans. The entire measurement lasted ~12 minutes and included collecting (and saving) OCT images as well as Raman spectra.

The Raman measurements were analyzed using k-means clustering which resulted in three different spectral clusters shown in Figure 4.1 D. The spectrum in green has been assigned to the tumor region whereas red cluster to the tumor border which contains a mix of normal as well as tumor tissue. From the microscopic image (Fig. 4.1 A) it was not possible to conclude how deep the tumor had invaded. With the penetration depth achieved by the Raman spectrometer system, the collected spectra contain chemical information from a depth of nearly 1 mm. Significant differences among spectra had been mostly intensity differences in the following regions: ~800-900 cm^{-1}, ~1000- 1100 cm^{-1}, ~1350- 1450 cm^{-1}, at 1449 cm^{-1} and ~1500- 1700 cm^{-1}. Spectra below 900 cm^{-1} had contained background due to system components. Thus, this region was subtracted from the analysis. The sample from patient #2 which had been extracted from the face and diagnosed as partially keratinized, partially eroded BCC had a good separation between tumor and non-tumor regions allowing the successful correlation of the Raman and microscopic data (Fig. 4.2).

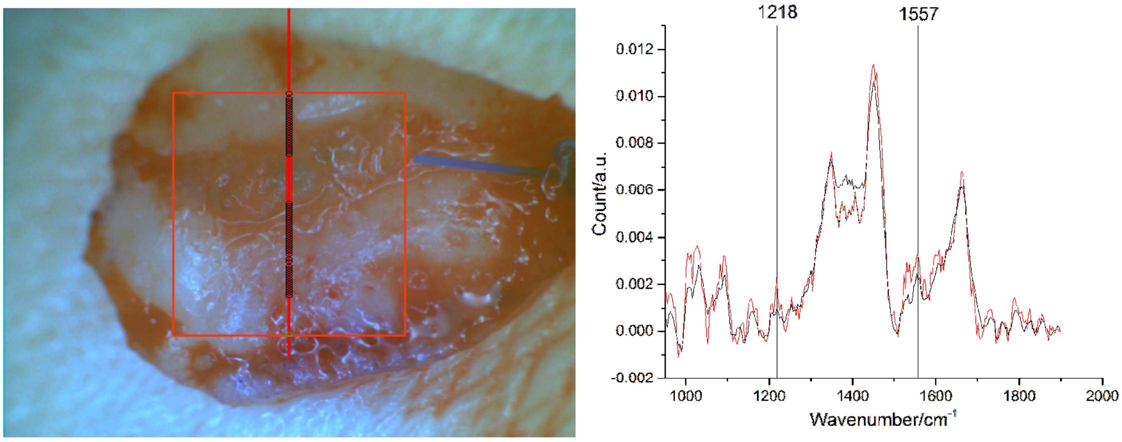

Figure 4.2 VIS image of a partially keratanized, partially eroded BCC overlaid with the Raman measurement (left). K-means cluster spectra showing differences in Raman peaks between tumor (red) and normal (black) tissue regions (right).

Between 1450 and 1660 cm^{-1} there has been an increase in intensity of those spectra originating from the tumor region. Moreover, there has been a peak shape difference observed with the Amide I band between the spectra obtained from the tumor and normal regions. The spectrum from the tumor region has a peak at 1528 cm^{-1} possibly corresponding to the presence of carotenoids and/or chromophores [93]. This has been observed to be similar to that observed in spectra on Fig. 4.1. Fig. 4.3 shows the difference spectrum of tumor and non-tumor regions.

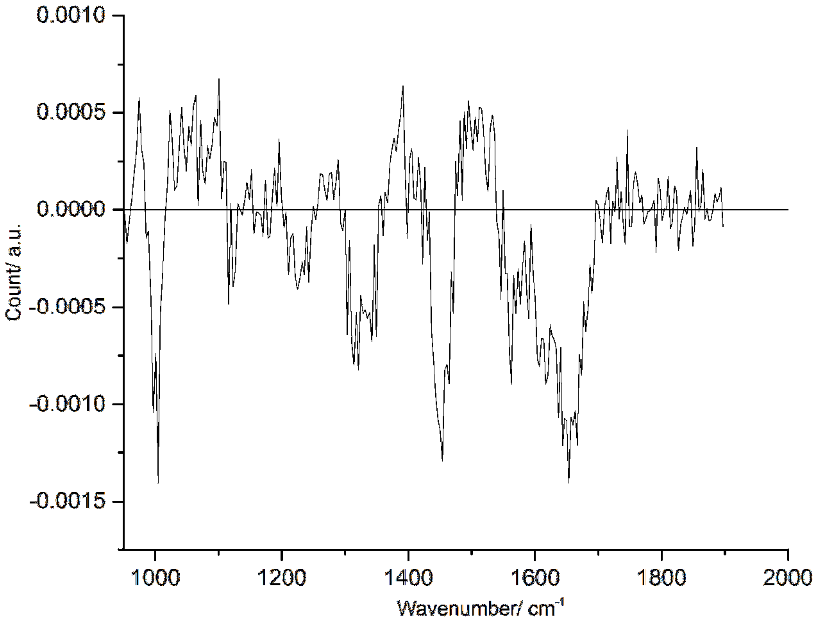

Figure 4.3: Differnce Raman spectrum of the sample from patient #4. The negative region specifies cancer related peaks while the positive is vice versa.

Apart from the sharp peaks at 1004 and 1449 cm^{-1} there have been broad regions identified between 1270 – 1350 cm^{-1} and 1600 – 1700 cm^{-1} as those with the most prominent cancer identifying regions. Since the original spectra have been noisy, it was challenging to accurately track the changes occurred due to BCC. Considering other samples, the difference spectra demonstrated a similar shape mainly at the region between 1400 and 1600 cm^{-1}.

A large sample variation was observed from patient-patient as well as sample-sample. Since all samples originate from different patients the physiology of the samples was different which had reflected strongly on Raman spectra. Many different BCC physiologies were measured that made it difficult to find similarities within one another. For example, the nodular BCC sample (patient #3, Tab. 4.1) was heavily pigmented which produced large amounts of fluorescence that had resulted in a poor background correction of the dataset which produced spectra with a lot of noise. On the other hand, some samples had no obvious visual differences between cancer and healthy tissue (patient #1, Tab.4.1). With the help of OCT imaging the erosion at the surface or embedded tumor clusters were discovered. These were challenging and nearly impossible to correlate with the H&E images due to the lack of perfect alignment of the former with Raman measurements. Therefore, the number of samples measured were too less to be able to correlate the results obtained by the two modalities. The most important outcome was that the H&E stains should be at the same location and direction of the Raman measurement. Consistency was key to our experimental protocol as good correlation was required for comparing the three techniques (i.e. OCT, Raman spectroscopy and histopathology) that had been addressed. Therefore, as the clinical routine procedures were given first priority, a thorough correlation of the data was not possible.

The results from the pilot skin cancer study provided important aspects of measuring human skin samples with OCT and Raman spectroscopy. The goal of this study was to investigate the characteristics of OCT images and Raman responses of the non-melanoma skin cancers and to correlate the findings with histopathology, which is currently the gold standard. The clinical approach taken by the group of Mahadevan-Jansen to differentiate between BCC and normal tissue with a combined OCT-Raman spectroscopy instrument, had moving optical parts [33]. In addition, the strategy employed involved collecting single spectra from the concerned region and the unaffected region. This approach seemingly reduces the efficiency in collection time of Raman measurements. By being able to obtain a Raman map from the region of interest more representative data can be collected and would provide a better overview of the tumor borders. Indeed, the system was not built to obtain confocal information but this was a compromise made for this specific application [87].

The integration time for each spectrum had been 30 seconds for the previously reported combined OCT-Raman setup [33] which had been sufficient to collect Raman spectra through the focal axis of the objective lens. However, moving the incident laser through many regions of the objective lens to obtain a Raman map would require longer integration times, thus the use of 1 second integration time for the mapping approach. Due to the time constraints the FOV was kept to a limit even though the system could measure a FOV of 10 mm [87].

There had been no mention of the total number of patients that had participated in the study but Raman spectral differences from one patient was presented by Patil et al. [33]. The largest differences observed were intensity variations at 1090, 1300 and 1440 cm^{-1} which seemed to have corresponded to the increase in nuclear material compared to the cytoplasm [33]. A similar trend can be observed in the present study as well. However, further measurements must be carried out to achieve better consistency in data and confirm spectral features associated to tumors. The pilot non-melanoma skin cancer study had suffered the most with the very small sample number. Until now, samples from 18 patients have been measured in this study. Another order of magnitude would be necessary to attain statistical consistency. This is because when comparing samples from different patients, the complexity of the study vastly increases. Moreover, the variety between different cancers would add another level of complexity to the dataset. Due to the inconsistency of Raman data collected, the data analysis was unique for each sample. However, the difference spectra and the Raman k-means data show significant intensity difference between cancer and healthy tissue.

A few SCC samples were also investigated which produced overly large fluorescence responses masking the actual Raman responses. With some BCC samples a dominant fluorescence background was observed that made the data analysis very challenging. In contrast, the same amount of fluorescence was not observed with the pork skin samples. Therefore, it would be safe to conclude that pork and human skin may have similarities, but not exhibit similar inherent fluorescence. It has been found that human skin has more vasculature than pig skin and the latter has a larger fat/ lipid content [90]. The increased inflammation of the skin may have been responsible for the increased fluorescence response in human skin samples. A workaround for inherent high fluorescence arising in the combined OCT-Raman setup would be the use of 1064 nm laser excitation wavelength. For this, an InGaAs CCD must be used as the common silicon CCDs would not be sensitive to wavelengths above 1100 nm. In order to further improve the system, the Raman spectrometer grating could be exchanged to higher number of lines/mm. This would result in accurate wavelength calibration with the only disadvantage of having to use longer integration times. If this could be complimented with real time diagnosis based on Raman and OCT images in a clinical environment, the advantages would most definitely compensate for the drawbacks.

Collecting spectra from normal tissue regions of patients would have provided more insight into the issue of patient-patient variability as well as the high fluorescent background as this could possibly be subtracted from the Raman spectra. Without an ethical vote for this specific strategy, any *in vivo* measurements would be impossible. The ease and feasibility of obtaining such a vote depends on the country. Verisante Aura ™ in the U.S. is a commercially available (FDA approved) setup that differentiates melanoma from non-melanoma by conducting a PCA analysis on Raman spectra. This setup uses an incident laser source power of 150 mW at 785 nm central wavelength which was proved not to harm tissue physiology [94].

If OCT were to be accepted as a gold standard, well-trained individuals on extracting accurate diagnosis would be in demand. Proving the similarity of OCT and H&E stains can be further supported by the dark inclusions on the 2D OCT scans that can be observed on the H&E image (Fig. 4.1 C III). This along with the scaly appearance and the increase in tissue density support the diagnosis of superficial BCC. The other types of BCC had features such as unorganized skin layer morphology which had been the hardest to isolate with Raman spectroscopy due to the scattered nodular features. The latter observation could be the property for concluding the recurrence of a cancer type as vastly scattered tumor granules have been known to reappear [95]. Fig. 4.4 further demonstrates the similarity of OCT images with H&E images.

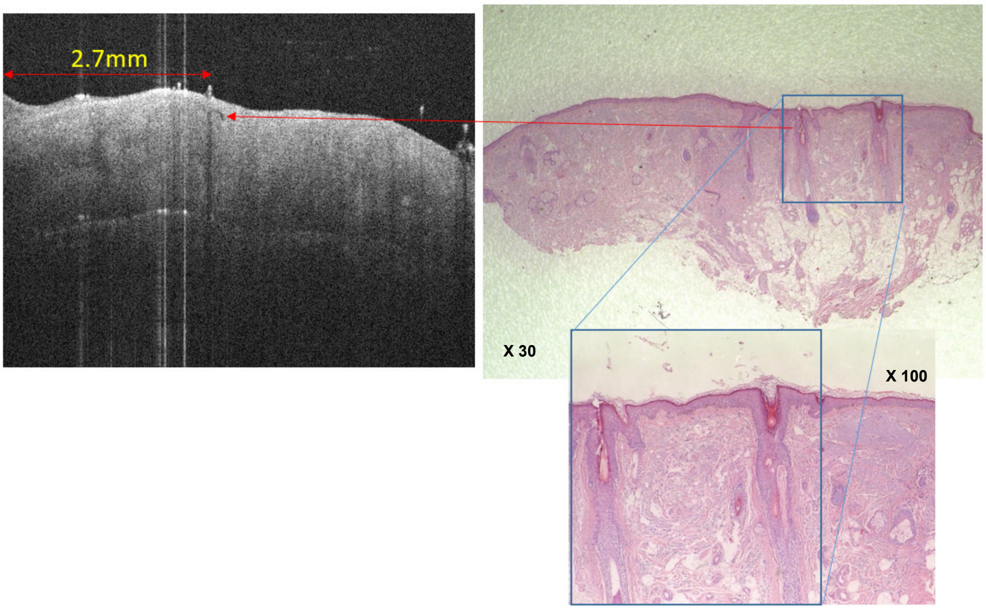

Figure 4.4: A B-Scan of the sample extracted from patient #1 compared with the H&E stains obtained from the pathologist. Note: H&E stains have not been sliced at the same angle of OCT measurement.

OCT is therefore ideal for visualizing exposed tumors and their cross sections to provide morphological information along with their location. There are a few commercially available OCT devices for investigating skin cancers, with different specifications according to the utilized optical components. Apart from devices used for research, those in the market already have successful outcomes. For example, Vivosight has been incorporated already into the clinics in New York, U.S.A for routine patient consultation. This particular device seems to have a high resolution of < 7.5 µm axially and < 5 µm laterally compared with the other commercially available devices. Skintell, another device in the market, has a 3 µm resolution both axially and laterally but a comparison study conducted showed that it has a lower penetration depth and lower signal intensity compared to Vivosight [96]. Another group from Vienna has introduced a medical OCT device into the market called NITID (11 µm axially and 12 µm laterally) which has been combined with dermoscopy.

Overall, the results from the pilot skin study had showed that every sample consisting of the same type of tumor vary in terms of composition and physiology. These variations were challenging to differentiate due to the inherent fluorescence that did not allow the post processing background correction to eliminate the background without obscuring signal contributions corresponding to the important Raman bands. By identifying the type of BCC relevant therapeutic interventions can be implemented. For example, superficial BCC can be intervened by non-surgical methods that would not be suitable for other BCC types [97, 98]. Therefore, combining both OCT and Raman spectroscopy would benefit patients as well as the medical community.

4.2 Investigating atherosclerotic plaques

Concerning the investigation of atherosclerotic plaques both OCT and Raman spectroscopy would be advantageous for the cardiologist in diagnosing the stage of development. To obtain a first impression of the physiology of plaques ex *vivo* animal arteries containing diet-induced plaques were measured. In total 3 *ex vivo* samples were tested with OCT and Raman spectroscopy, 2 before and 1 after the combination of the setup.

Several animal models have been commonly used to investigate atherosclerosis such as mouse, rabbit and pig. Many parameters such as similarities to human physiology, ease of care and the time frame of plaque formation should be taken into account when choosing a suitable model [99]. As one of the first attempts, our research group had used a rabbit model for distinguishing plaques *in vivo* via Raman spectroscopy only [85] and the extracted aorta samples from that experiment have been used for the current measurements. The main reason for using rabbits as an animal model was due to the similarity of the cholesterol uptake and plaque formation pathways to that observed in humans [99, 100]. To extend this study, an *in vivo* animal experiment was conducted to achieve direct understanding of the suitability of the systems, data quality and the levels of fluorescence.

4.2.1 Evidence before the combination.

The OCT device used to visualize *ex vivo* rabbit aortas was a TEL310 (Thorlabs, Lübeck, Germany) with an OCTG-1300 scanning apparatus. Initially a region of interest (red square, Fig 4.5 A) was selected where a 3D C-scan was carried out (Fig 4.5 B) with a spacing of 30 × 38 × 7 µm. By changing the contrast post acquisition, it was possible to gain a surface image (XZ slice) where the cholesterol deposits appear brighter than the rest of the aortal structure. Since atherosclerotic plaque depositions exhibit a higher refractive index compared to the connective tissue of normal vessel walls of aortas (high scattering cross section), lipid inclusions back reflect more light. This had allowed the easy separation between plaques and surrounding by adjusting the contrast of the image.

Fig. 4.5 A shows the microscopic image of the aorta section, ~3 cm in length and ~6 mm in width, cut open along the direction of the blood flow exposing the inner surface. It does not provide much information on the topology or any plaque formations. The 3D OCT image (Fig 4.5 B) of the entire aorta sample showed the rough texture of the inner surface but with no plaque information. By choosing specific regions on the aorta, a more detailed visualization was achieved as this had increased the resolution of measurements. As can be seen in Fig 4.5 C, the brighter regions could have been early plaque deposits. The penetration depth of the OCT can be estimated to be between 1 and 1.5 mm into aortal tissue. Most of the plaques locations had a tendency to be at slight bends or ridges of the aortal section as this topology would produce a physical barrier against the blood stream promoting easy deposition. Thus, the plaque volume seemed to decrease at the edge of the sample (away from the bend) compared to the measured region shown on Fig 4.5 C.

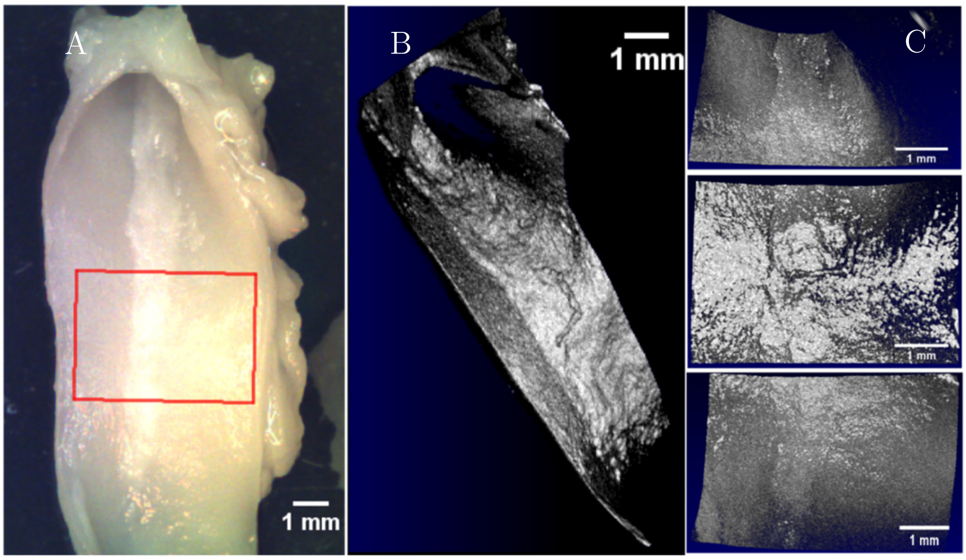

Figure 4.5: A shows the microscopic white light image of the rabbit aorta and B is the corresponding 3D OCT C- scan. C shows three zoomed in sections of the rabbit aorta enhancing the surface topology of the top, middle and end.

For the Raman measurement a confocal Raman microscope (WITec alpha300R, Ulm, Germany) was used with a 10x objective lens (Nikon 10x, Japan) and the spectral results are shown on Fig 4.6.

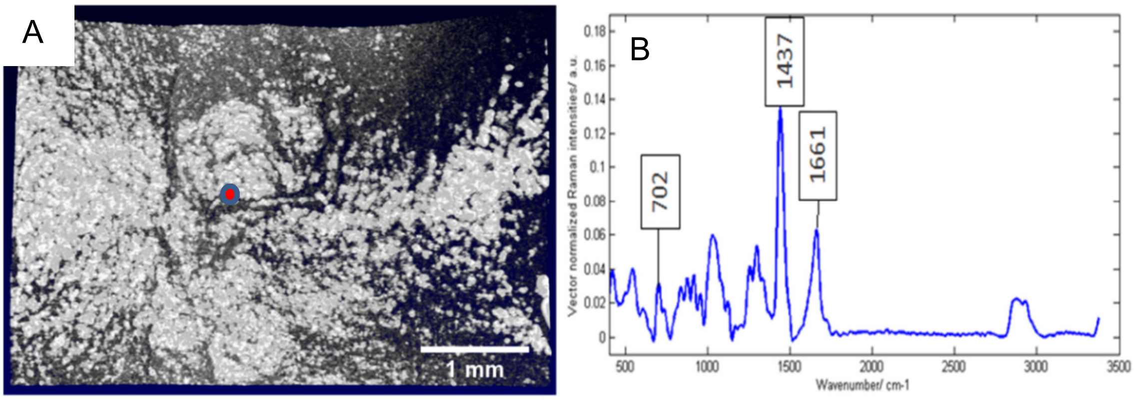

Figure 4.6: A shows the topology of the arterial wall emphasizing the plaque deposits with contrast adjustment. B is the Raman spectrum collected from the plaques at the position shown in A. The spectrum shows mainly cholesterol contributions.

The Raman spectrum (1 sec. integration time, 40 mW at the sample) shown in Fig 4.6 B indicates the presence of lipids and cholesterol at the location where the spectrum was collected and this was measured from the red spot shown on the surface 3D OCT scan (Fig 4.6 A). Spectral bands at 702, 1437 and 1661 cm^{-1} correspond to cholesterol as specified in literature [101]. Since the chemical make-up of plaques is complex, the resultant spectrum is a superposition of all the contributions of the constituents. Therefore, the pure spectra of cholesterol and lipids would have more distinct Raman peaks than observed here.

Table 4.2: Details of the rabbit aorta sample. It had been included in a previous *in vivo* experiment and so anesthesia (ketamine 2-8 mg/kg and xylazine 0.5-1 mg/kg) had been administered by intravenous injection during the experiment [85]**.**

Sample origin	Adult male rabbit (New Zealand White, Harlan) weighing 3.25- 3.58 kg
Diet	0.5% cholesterol
Time period	approximate 7-10 weeks
Fixing procedure	150 ml mixture of 10% hydroxyethyl starch and 1% porcine in ratio of 10:1 followed by a 0.9% saline pressure perfusion at 100 mmHg for a period of 15 mins. The complete aorta was then excised and preserved in 5% formalin solution.

The diet of the animal had been key to observing the plaque formations and as can be seen from the rabbit aorta the plaques had not been fully developed until the advanced stage. Therefore, no advanced plaque inclusions were observed but superficial spot-like distributions of early plaques. During these *ex vivo* measurements the risk of sample dehydration due to the constant exposure to the laser was prominent. At times, a few drops of formalin was added to renew moisture. Moreover, any residual blood on the aorta surface had increased the risk of burning the sample. Therefore, an optimal laser power must be determined for these experiments. In fresh samples, before fixing with formalin, the constituent blood would be still liquid which would not harm the samples. The outcomes of the *ex vivo* rabbit aorta measurements have helped the transition to working with *ex vivo* human aorta samples.

The same measurement strategy was applied to investigate intact *ex vivo* human aorta preserved in 5% formalin. First, a 3D OCT image was collected followed by Raman spectra from a position shown in Fig 4.7 A. Here the KAISER RX Raman spectrometer was used to collect point spectra (1 second integration time, 40 mW at the sample). To expose the inner surface of the aorta the sample was pinned onto a corkboard as it tended to roll to its original cylindrical shape.

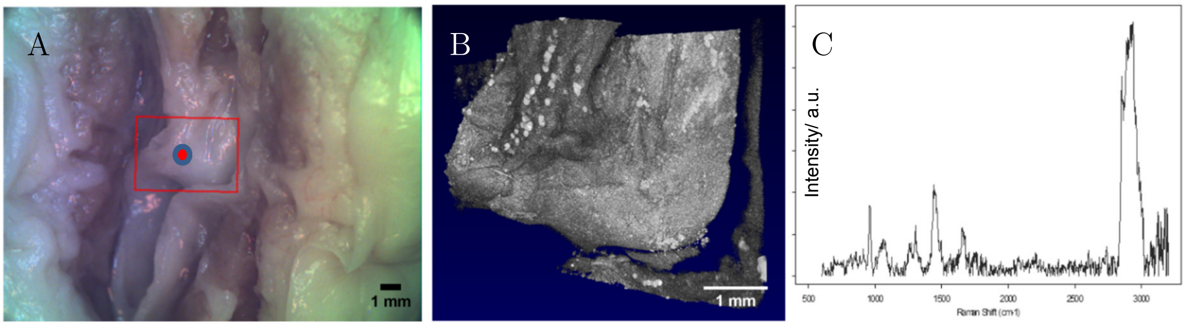

Figure 4.7: A shows the bright field image of the inner wall showing the selection for the 3D OCT scan. B shows the 3D OCT scan. C shows the Raman spectrum of the sample showing lipid.

The 3D OCT image (Fig. 4.7 B) do not show any obvious change in contrast at the measured location (red spot in Fig. 4.7 A) but there is evidence of lipid deposits as depicted by the Raman spectrum (Fig 4.7 C). The Raman band at 1442 cm^{-1} and 1660 cm^{-1} as well as the bands in the lower wavenumber region relate to the CH_2 bending and C=C stretching vibrations associated with cholesterol, cholesterol esters and fatty acids. The band with the highest intensity from 2800 – 3000 cm^{-1} corresponds to CH stretching vibrations.

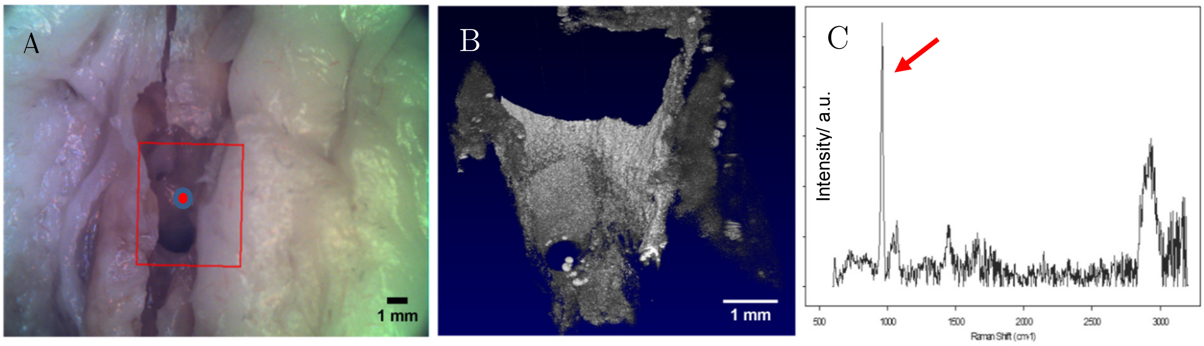

Figure 4.8: A shows the bright field image of the inner wall showing the selection to do 3D scan. B shows the 3D OCT scan. C shows the Raman spectrum of the sample showing calcium peak position (red arrow at 950 cm^{-1}).

At another region on the same aorta, the presence of crystalline calcium was obvious from the Raman peak at 950 cm^{-1} (Fig. 4.8 C). The 3D OCT image clearly showed the topology of the cavity that was scanned. Calcium deposits have been represented as a sheet- like bright layer with OCT, which had been difficult to distinguish from the VIS image of the aorta wall. These measurements therefore show the use-case of both OCT and Raman spectroscopy. The next section focuses on the combined OCT-Raman setup to characterize an *ex vivo* human aorta.

4.2.2 Combined OCT-Raman system measurements *ex vivo* human aorta

Several aorta positions had been scanned using OCT prior to the Raman imaging step. OCT C-scans consisted of a volume of 4 × 4 × 3 mm with a penetration depth of 1.5 mm. The OCT image acquisition took less than 10 seconds. Fig. 4.9 shows the OCT images of the above-mentioned dimensions and 4.9 A represents a C-scan with the noticeable abnormal inclusions indicated by a red arrow. The image has been overlaid by the B-scans that were chosen to demonstrate a calcified deposition (Fig. 4.9 B). The deposit had a diameter of ~ 0.25 mm and approximately 0.5 mm below the aorta surface. This is easily comparable with B III where no noticeable inclusions had existed. Histopathology images corresponding to the B-scans are shown in Fig. 4.9 C and the calcium deposit was successfully correlated with the tissue sections. This was conducted after OCT-Raman image recording and the image analysis was carried out on the software ThorImage OCT and ImageJ software.

Those areas with inclusions (higher refractive index) were chosen for Raman imaging which were recorded with resolutions varying from 50 to 100 µm as well as areas ranging from 0.25 to 1 mm^2. The data acquisition was limited by the step size and due to the time constraints smaller areas such as 2 × 2 mm were recorded with Raman image acquisitions.

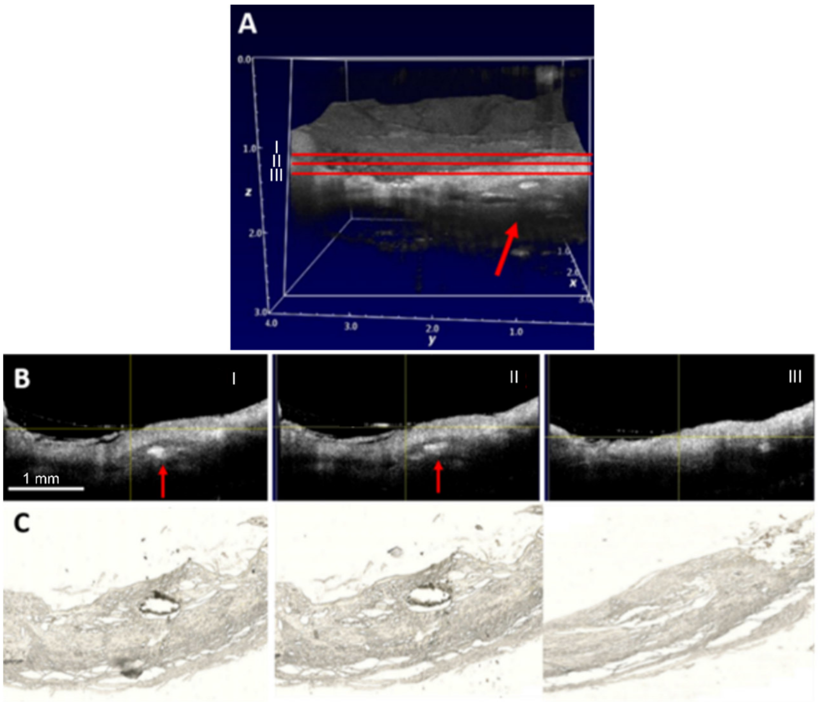

Figure 4.9: OCT images of the aorta area with calcified depositions in comparison with histology. A is an OCT C-scan image of a 4 × 4 mm^2 area and B are representative B-scans of the positions indicated in A as I – III. B I and II show calcification, which was confirmed by histopathology shown in C. B III does not show significant inclusions. Adapted from [102].

Raman spectra were background corrected via a SNIP algorithm [89], and area normalized. Raman images were generated by the N-FINDR spectral unmixing algorithm described by Winter et al.[103, 104] and by a k-means clustering and in both cases R software packages were used [105]. These Raman maps have been overlaid with a sample C-scan on Fig. 4.10. Another surface C-scan of the sample has been shown in Fig 4.11 A and the area with the calcium deposits were located approximately 0.5 mm beneath the surface (red square). By adjusting the overall contrast of the image, the inclusions were made visible. This region was then measured using Raman spectroscopy similar to that of the pilot skin cancer study. The dimensions of the Raman images are 1 × 1 mm^2 with a step size related resolution of 100 µm. Since the sample was already fixed in formalin there had been no time constraints for measurements but the sample was tending to dry during longer measurement times.

The corresponding Raman spectra from the two algorithms used to produce Raman images have been plotted in Fig. 4.11 B - E. They have clearly identified 3 different regions within the area of interest indicated by the red square on the 3D OCT image. Raman spectra show Raman bands that are typical for proteins, as well as calcium phosphate. For the NFINDR algorithm the calcification has been plotted in green and for the k-means in red where both exhibit a sharp calcium phosphate peak located at 960 cm^{-1}. Calcium phosphate is the main inorganic component found in calcifications of the arteries, whereby the scattering intensities are caused due to symmetric vibrations of the $(O{=}PO_3)^{2-}$ anionic phosphate. The areas surrounding the calcification shown in blue colors are mainly connective tissue, which produce spectra with main protein features at 1650 and 1455 cm^{-1}, associated with carbonyl stretches of the peptide bonds of the protein backbones and CH_2 deformations of the peptide residues, respectively. Significant amounts of lipids, such as cholesterol or triglycerides could not be observed, which may have been incorporated into the band positions of the two mentioned Raman bands generally found at slightly lower wavenumbers around 1650 and 1440 cm^{-1} for lipids.

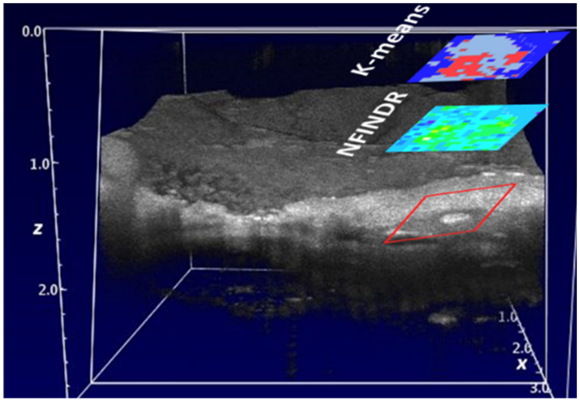

Figure 4.10 Raman maps overlaid over the 3D OCT scan that shows the calcium inclusion of the measured human aorta sample. Adapted from [102]

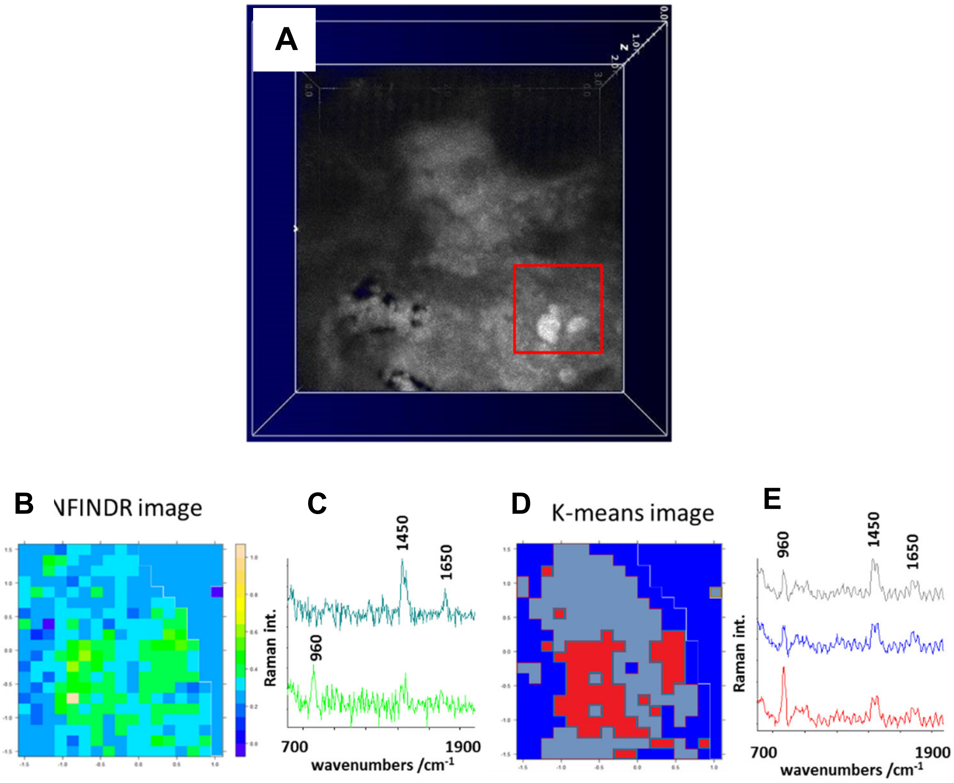

Figure 4.11: OCT image of the surface C-scan of the plaque is shown in (A). The red square shows the region of interest where the Raman maps have been collected. The Raman spectra shown in B and C, as well as D and E for a VCA and K-means cluster analysis, respectively represent the plaque contituents. Adapted from [102].

The Raman maps have been overlaid with the 3D OCT image, where the top image (also shown on Figures 4.11 B & D) reconstructed by the spectral unmixing algorithm and the bottom by k-means clustering. The relevant sample details are shown on Table. 4.3.

Table 4.3: The sample information of the *ex vivo* human aorta. The extraction was conducted at the Heart Center Freiburg-Bad Krozingen, University of Freiburg, Freiburg, Germany [102].

Sample origin	Human carotid artery plaques donated with written consent by patients who underwent endarterectomy.
Fixing procedure	5% para-formaldehyde and stored at 4°C
Histopathology	Samples embedded in Tissuetec® and cryo-sectioned using a CM1860

	cryotome (Leica, Germany) at -20°C, into sections of 10 µm.

In both *ex vivo* human samples lipid signatures had been observed along with very intense Raman bands of crystalline calcium (if present). With the second *ex vivo* human aorta the acquired Raman images correlated very well to the calcium rich areas identified by OCT. The penetration depth of the Raman scans was undoubtedly enough to record spectra with a good signal-to–noise ratio. Differentiation of crystalline calcium deposits from the surrounding connective tissue was possible with the chemically specific Raman spectroscopy. One observation that is important to mention is that areas with high abundances of coagulated blood did not give any measurable Raman signal, but showed strong fluorescence backgrounds, which was not surprising because of the presence of chromophores. After the investigations with *ex vivo* samples an *in vivo* investigation was implemented using an animal model and the following section discusses its experimental details.

4.2.3 *In vivo* plaque investigation

It has been shown with the outcomes of the *ex vivo* samples in previous sections that plaque characterization with the combined OCT-Raman setup is in fact feasible. However, before the introduction of a novel device into the clinics it must be tested on an animal model *in vivo* to address unexpected issues. In order to enable such an investigation a special fiber probe must be developed combining both OCT and Raman spectroscopy which can reach the arteries. As a preliminary step to the catheter fiber probe, the ability to correlate OCT and Raman data collected in real surgical conditions was tested using separate systems.

For surgical conditions, all devices must be able to withstand the standard sterilizing procedure. If the function of the optical components were to degrade over time due to the use of ethanol, the entire design of the system must be changed to suit clinical requirements. Moreover, there is a large probability that the presence of blood in arteries could result in producing large amounts of fluorescence that might obscure the Raman signals. The same goes for the contrast agent used in OCT imaging that flushes the arteries temporarily before measurement. Unless tested these points are challenging to predict and would carry the risk of interfering with the Raman signals leading to false outcomes. Therefore *in vivo* animal tests with the two modalities are necessary.

For this endeavor, an external OCT system was used along with a clinically approved catheter probe. The details of the OCT instrument is shown on Table 4.4.

Table 4.4: OCT instrumentation of ILUMIEN™ Optis™ system (St. Jude Medical, US) for *in vivo* investigation of plaques

Type of OCT and source wavelength	Swept source at 1305 ± 55 nm
Power	26 mW
A-scan depth in air	7 mm
A-scan depth in contrast agent	4.83 mm
Scan repetition rate	90 kHz
Frame rate	180 images per second
Catheter used	C7 Dragonfly (St. Jude Medical, US)

The contrast agent was required to allow better contrast and it was administered before OCT imaging manually into the side port of the imaging catheter. During the experiment the OCT probe was inserted through a 6F introducer (B. Braun, Melsungen, Germany) that was attached to a guidewire (Terumo, Tokyo, Japan). Once the contrast agent had been introduced the device software had initiated the pullback process which measured a length of 40 mm. This pullback technique enabled the imaging of the entire circumference of the vessel. The probe was essentially pulled backwards at a constant speed from a certain location where plaques were suspected to occur. During the pullback, the cross-sectional recording of the aorta took place in a helical fashion. This rotating movement had been achieved by a microcontroller implemented into the commercial OCT system only. All data were reviewed later with the help of the cardiologist.

Raman fiber probe used in this study had been successfully utilized in a previous *in vivo* rabbit experiment within our working group [85]. The Raman setup and fiber information are shown in Table 4.5.

Table 4.5: Raman spectrometer and fiber probe details.

Raman spectrometer	RXN1 spectrometer (Kaiser optical systems, USA)
Fiber probe	Multi-mode (MM) excitation waveguide of 100 µm diameter surrounded by 12 MM collection fibers; diameter of 125 µm. (EM Vision, Loxahatchee, FL, USA)
Total diameter	1 mm (after the steel guided tube)

Incident laser source	Invictus MM cw laser with an FC/PC coupling at 785 nm with 100 mW fiber coupled power
Integration time	1 – 10 second

The fiber probe was embedded at the front with edge filters to avoid any excitation light entering the collection fibers. The fiber probe was designed as a forward facing even though a side-viewing probe would have been more appropriate. In fact, the in-house side-viewing fiber probe that was scheduled for the experiment was too large that there was too less space for the fiber probe to move along the rabbit aorta. It would have eventually caused ruptures and damage the aorta wall. To meet the requirements of the SMA input of the excitation path connector, an SMA – FC/PC adapter was used. At the output of the probe, the twelve collection waveguides were stacked in one line around the SMA connector so that the CCD would essentially detect a vertical line coupling the back scattered Raman response. Binning was adjusted to minimize CCD noise and background effects. A spectrometer wavelength calibration, as well as an intensity correction for changing quantum efficiencies of the CCD was carried out after moving the spectrometer to the clinic. The laser wavelength was calibrated by cyclohexane after the CCD cooling procedure directly before surgery. The whole system was set on a mobile tabletop to enable flexibility during the entire process.

The animal experiment involved rabbits with induced-plaques and the details of the animal and fixing process has been listen in Table 4.6.

Table 4.6: Details of the animal, diet and the fixing procedure for the *in vivo* measurements

Animal	Male rabbit (New Zealand White, Harlan) weighing approximately 3kg.
Diet	0.5% cholesterol
Time period	approximate 7-10 weeks
Fixing procedure	150 ml mixture of 10% hydroxyethyl starch (Fresenius Kabi Deutschland GmbH, Bad Homburg, Germany) and 1% porcine in ratio of 10:1 followed by a 0.9% saline (Fresenius Kabi Deutschland GmbH, Bad Homburg, Germany) pressure perfusion at 100 mmHg for a period of 15 mins. The complete aorta was then excised and preserved in 5%

	formalin solution (Oscar Fischer GmbH, Saarbrücken, Germany) solution.

The rabbits were anaesthetized via an ear vein intravenously using ketamine 2-8 mg/kg (Ketamin "Gräub" 10%, Albrecht, Aulendorf; Germany) and xylazine 0.5-1 mg/kg (Rompun Trockensubstanz, Bayer, Leverkusen, Germany). A 6F introducer (B. Braun, Melsungen, Germany) was inserted through a small arterial cut, followed by the insertion of a guidewire (Terumo, Tokyo, Japan), which was inserted into the descending aorta. Then for image with OCT through a 6F catheter (Cordis, Langenfeld, Germany) the contrast medium (Visipaque, GE Healthcare Buchler, München, Germany) was introduced to obtain an angiogram of the complete aorta. Throughout the entire experiment angiography was enabled to localize fiber probes. There had been concerns that the contrast agent would harm the animal which resulted in swapping the imaging order i.e. first Raman measurements were conducted and then the OCT scanning. The measurements were carried out one after the other such that first the Raman –probe was inserted assisted by the catheter until the aortic bifurcation and slowly retracted manually collecting Raman data on suspicious lipid depositions. The Raman measurements has begun at the abdominal aorta and proceeded to collect from thoracic and aortic arch. Single point spectra were collected between 1 – 3 seconds integration time and approximately at every 0.5 cm. Subsequently, the Dragonfly catheter was introduced after withdrawing the Raman probe and several scans were measured along the entire length the aorta. At the end of the measurements the animal was sacrificed and the aorta fixation procedure as mentioned in Table 4.6 was followed.

The outcome of this experiment for characterizing aorta was that the aorta was normal with sightings of early plaque formations at a few positions. The relevant OCT images are shown in Fig. 4.12 picked from the image dataset which also show the Dragonfly OCT probe. These cross-sectional OCT images were collected from the thoracic aorta and the most distinctive features observed were the rough slightly bulging formations on the inner vessel wall (white arrows in Fig. 4.12). Here, the importance of the penetration depth achieved by the system can be displayed by the fact that the entire circumference of the aorta was imaged even though the probe placement was at the one end of the vessel (diameter ~ 3.5 mm). The depth visible on the aorta wall was ~ 0.75 cm and the deformations were a few 100 µm in size.

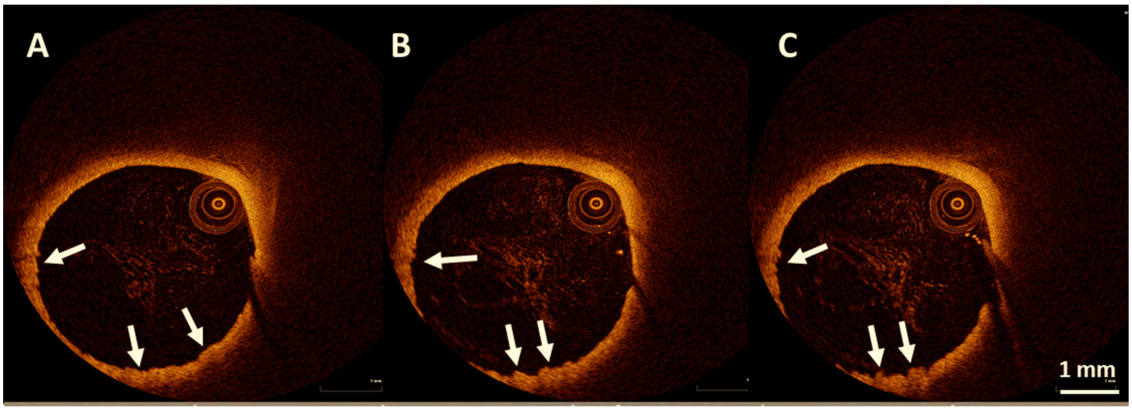

Figure 4.12: OCT images of one of the rabbit aortas investigated for characterizing plaques *in vivo*. The white arrows show the locations of early plaque formations.

Apart from cross-sectional images, the pullback imaging method had produced an entire optical cut along the blood flow of the measured aorta (Fig. 4.13).

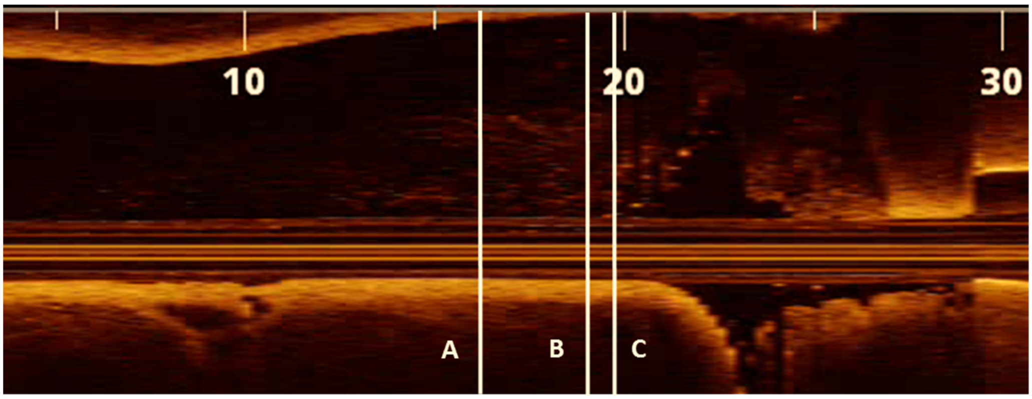

Figure 4.13: OCT cross-sectional image across the blood flow of the thoracic aorta. The positions marked A,B and C correspond to that shown in Fig. 4.12. The units of the scale are in mm.

The entire length measured was about 3 cm, minus the image obscured either by the heartbeat of the rabbit or the OCT probe reaching the end of the catheter. On the other hand, the collected Raman spectra had produced characteristic bands related to lipids mainly. Collagen signatures were also observed as the vessels contain connective tissue. This resulted in protein and cholesterol related spectral features being detected in the Raman dataset. Signs of lipid deposits had appeared in the upper part of the aorta close to the heart. This can be seen from the spectra shown in Figure 4.14.

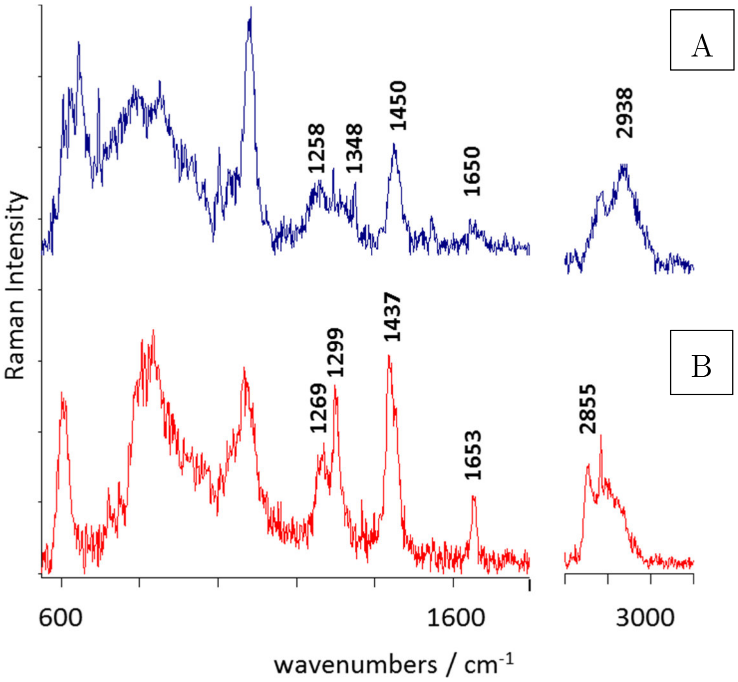

Figure 4.14: Raman spectra from an aorta position that do not contain plaque depositions (A) and that with lipid depositions (B).

The spectrum A (Fig 4.14) shows the typical Raman bands of proteins that relate to the protein/collagen from the arterial wall whereas the spectrum below displays lipid features. The peak at 2855 cm^{-1} has been associated to CH_2 symmetric stretching [106] and therefore shows the presence of lipids. In general, the shape between the spectral region between 2800 and 3000 cm^{-1} contains a difference. In the lower spectral regions, peaks at 1269 (C-H symmetric rock- *cis*) [106] and 1299 (triacylglycerol) [107] can be observed.

The extracted thoracic aorta was dissected for histopathological inspection. An elastic van Gieson (EvG) stain was applied to emphasize the microscopic features and this was compared with the OCT and Raman data. Fig. 4.15 shows the comparison between the OCT B-Scan and the EvG stain obtained from the same location as the OCT image. The alignment of data locations were not precise due to the slight change in protocol i.e. utilizing Raman spectroscopy prior to OCT imaging. As Fig. 4.15 B suggests the intima had been swollen compared to the rest of the tissue circumference. Since OCT would provide the most natural image of the intact aorta compared to the histopathology, the swelling had not been very prominent at the region emphasized (white box). The stained image shows spaces between the tissues that can be concluded to be lipid deposits.

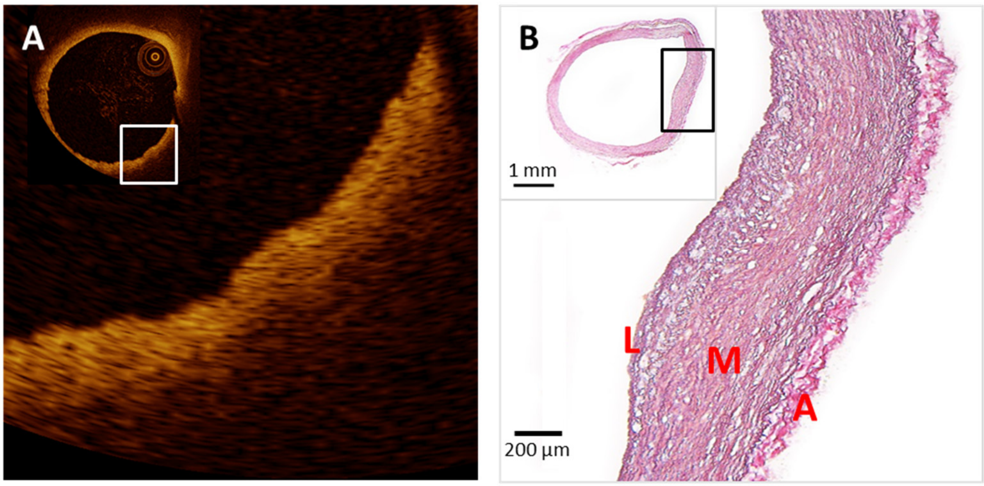

Figure 4.15: OCT image with an inset showing the entire cicumference of the aorta (A) from the extracted part shown in figure 4.13. (B) is an an EvG stain of a section from the same region (L → lumen or artery, M → muscularis media and A → adventitia).

Comparing the morphological information with the spectroscopic features, Raman bands have highlighted the presence of lipid build up at the regions of the aorta.

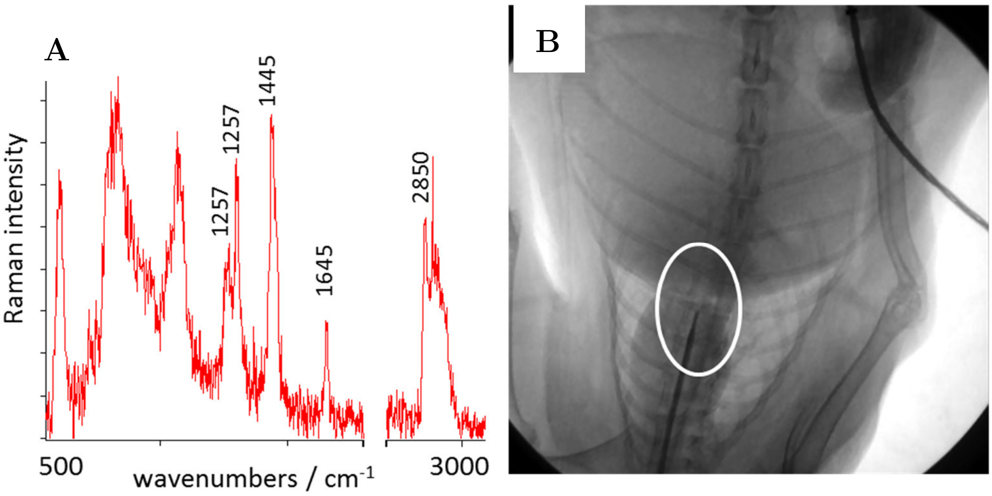

Figure 4.16: The spectrum on (A) has been taken from the location shown in image (B) which an X-ray image is taken during the experiment. The position of the Raman probe can be seen as a dark line adjacent to the bottom of the image.

The trend in Raman bands are similar to that shown in Fig. 4.14.

Table 4.7: The assignments of the observed Raman band in Fig. 4.16

2850 cm^{-1}	Symmetric methyl stretches
1640 cm^{-1}	C=C stretching of unsaturated
1440 cm^{-1}	CH_2 scissoring
1150 – 1300 cm^{-1}	CH deformations- saturated and unsaturated fat

At lower wavenumber regions the quartz fiber probe had produced background that had not allowed the successful extraction of Raman spectra. Considering the overall spectral shape, triglycerides have been the main ingredient of plaques measured in this experiment. Previous results have also shown that plaque depositions have been dominated by cholesterol, cholesterol esters as well as accumulations of triglycerides [47, 108]. Hence, the combination of an OCT-Raman microscopy setup, which can operate in imaging mode, have clearly identified areas of calcification as well as the presence of lipids within an arterial wall affected by atherosclerosis.

This chapter has documented the experimental results from individual systems as well as the combined modalities. Opting for measurements with separate systems in the case for both *ex* and *in vivo,* had assisted the preliminary assessment of spectral quality and issues related to the methodology. In general, plaques from animals had not shown the expected amounts of plaque formations either due to low concentrations of cholesterol or simply less consumption. The OCT scans had delivered very clear images of the morphology of the atherosclerotic inclusions as well as surrounding tissue. For early plaques just using OCT did not show a large difference in contrast between the surrounding area and lipid inclusions. From the Raman spectral analysis the achieved sensitivities were enough to detect early plaque formations. The obtained data quality was sufficient to assign the major plaque constituents as triglycerides reflecting the cholesterol enriched diet. The experimental strategy involved applying several seconds of non-focused laser illumination at 100 mW within the artery that had not lead to any noticeable alterations of the walls of the blood vessels, as confirmed by subsequent histopathological staining. For the current setup for an excitation wavelength of 785 nm, the time frame of 1 s per spectrum at a laser power of ~ 100 mW at the laser focus was comparable to similar experiments previously reported and potentially applicable to *in vivo* conditions [108-110]. Thus, the combination of both modalities is required to arrive to a conclusion when dealing with early stage plaques. Moreover, the *in vivo* measurement emphasized the feasibility of this technique and using both information from OCT and Raman are vital for diagnostic decisions.

To conduct a more thorough investigation on identifying different stages of plaque development, more samples are necessary so that the morphological features and spectroscopic signatures can be identified for each type. This would eventually result in reduced false positives and would lead to more diagnostic standardizations. The amount of stress induced by this dual approach is still very high. Containing two modalities in one device would result in the collection of twice the amount of valuable information in one attempt compared to a diagnosis confirmed by a single method.

This would drastically reduce the amount of surgeries the patients would have to undergo. Moreover, by the knowledge acquired through exhaustive measurements, the cardiologist would be able to estimate the stage of the plaque and prescribe more effective therapeutic measures at an earlier time point. Not only for plaque characterization but also the possible treatments such as balloon angioplasty or stent implantation can be monitored by this combined imaging method. Second-generation balloons for angioplasty and stents, which have been coated with drugs to prevent early restenosis, are currently under development [111-113]. The efficiency of such drug coated balloons and drug eluting stents can be investigated by monitoring the concentration and long term release spectroscopically, as the active compounds would exhibit distinct spectral bands [114, 115].

As for next steps, an OCT fiber probe was developed for the inclusion of Raman modality so that the *in vivo* atherosclerotic characterization would be enabled. The following chapter presents the details of the OCT fiber probe development for future combination with Raman spectroscopy.

5 Fiber approach

The venture to have non-invasive medical devices that could reach inner organs to expose the disease-causing agent is still under way. Especially with atherosclerosis this has become one of the main points to influence the development of a flexible fiber probe that can access the arteries where plaque formations are located. This fiber probe can further be applied in characterizing skin cancers to investigate depth infiltration. The combination of OCT and Raman spectroscopy for characterizing plaques the imaging probe head would need to be miniaturized into a fiber probe that it can access the aortas via a small incision. This would in the end obtain both morphological and spectroscopic information that would lead to better diagnosis. The following sections present the OCT fiber probe development and the future next step would be to include the Raman modality. For this venture, we had collaborated with OBEL labs at the University of Western Australia (UWA) which pioneers in fiber OCT development for clinical application such as imaging breast cancer [51] and deep skeletal muscles [116]. For the measurements with this OCT fiber probe a special sample holder was designed and produced. The fiber probe was later characterized to obtain the spot size and other properties in terms of performance. A similar setup was built at the Leibniz Institute of Photonic Technology (IPHT) which was able to couple with the SD-OCT system that had been introduced previously.

5.1 Sample holder

A sample holder for OCT fiber probe measurements was required due to the properties of the sample itself as well as the experimental strategy. The samples described in section 4.2.1 were used again where the aorta section was cut perpendicular to the axis into three ~15 ×15 mm samples. These aorta samples had a tendency to roll up due to its natural cylindrical shape and elasticity. To prevent this from occurring an in-house sample holder was designed using SolidWorks (Fig. 5.1, left) which was then produced using a 3D printer. The circular opening of the top cover measured up to a diameter of 16 mm (Fig. 5.1, right) which was protected by a quartz slide. The quartz cover was fastened onto the top part of the sample holder by using UV adhesive. This type of glue was chosen as it would not contain organic components that would have potentially interact with the samples. The quartz window had been implemented so that the sample would be protected from any collisions that might occur between the fiber probe and the sample. It further flattens the sample enabling easier scanning. The base of the holder consists of a raised stage-like protrusion where the sample would be usually placed. The gutter-like structure around this stage was designed to hold any extra liquid introduced onto the samples for maintaining appropriate moisture levels. With the help of four plastic screws the top cover can be secured to the bottom part along with the aorta sample in between. This sample holder prevents the sample from losing its moisture during measurement and it efficiently keeps the aorta open exposing the inner arterial wall. The amount of stress applied during fixing the two parts must be minimal as the quartz window had shattered a few times.

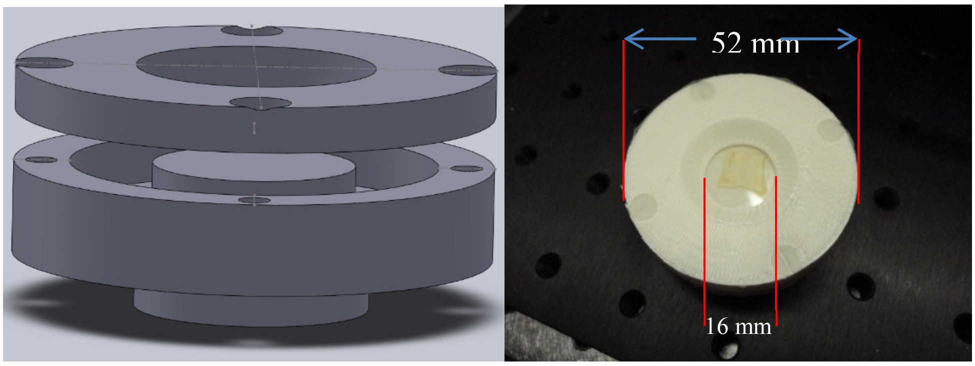

Figure 5.1: Sample holder design sketch (SolidWorks, left) and the 3D printed product showing its dimensions (right).

The bottom half of the holder has extra material printed, similar to a stand, so that a tiltable stage would be able to maintain a stable grip.

5.2 Needle probe

The development of a needle probe specifically for medical applications was intended to minimize the invasiveness of the entire investigation. In the clinic this would be suitable for a point-of-care imaging modality [117]. Even though the procedure is identified as a minor surgery the incision would be relatively small. For intravascular applications needles cannot be used but this was the closest approximation to the necessary miniaturized geometry and the needle was used as a casing to protect the fiber and to provide rigidity during experiments.

Initially, an ABCD Matrix [118] was utilized to simulate and explore the feasibility of the OCT fiber probe that would fulfill the required parameters such as the focus spot size, beam diameter and working distance. Then the proposed enface needle probe was developed which consisted of a stretch of single mode fiber (SMF) that had transported light from the base unit. A length of 345 µm no- core fiber (NCF) with a diameter of 120 µm had dispersed the light beam which focused onto the sample using a gradient- index (GRIN) lens with a length of 108 µm (Fig. 6.25). After splicing these crucial parts together, the fiber was then inserted into a 690 µm needle after the head of the needle was sanded down. The casing by a needle was carried out to give the probe some rigidity and for easy handling. By introducing a blunt tip, the fiber probe would be able to reach the surface of the quartz sample holder window.

It further protects the user from accidentally poking himself. In the case of skin cancer diagnosis the needle would need to be sharp in order to penetrate through tissue to obtain depth imaging for example. Index matching liquid (NA = 1.5) were used between the quartz window and the fiber tip to reduce artefacts. The resulting NA of the fiber was 0.048.

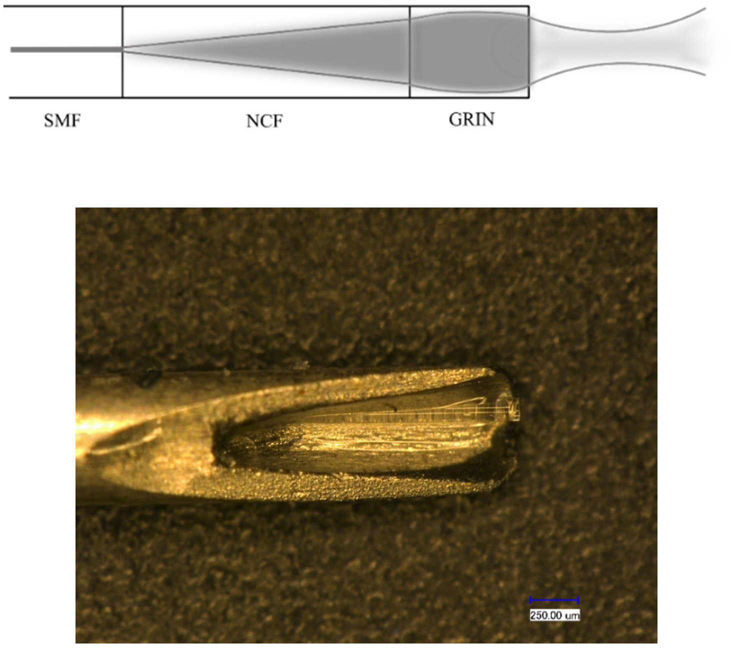

Figure 5.2: The schematic of the needle probe (top) and image (bottom)

The working distance or the focal length of the OCT fiber probe was 380 µm in air (513 µm with a $n = 1.35$ i.e. the average refractive index of water and tissue) and the focal spot diameter was measured to be 20 µm. These resultant parameters were very close to the parameters specified for the simulation (575 µm working distance and 17.4 µm spot size). The uniformity of the beam profile can be observed in Fig. 5.3.

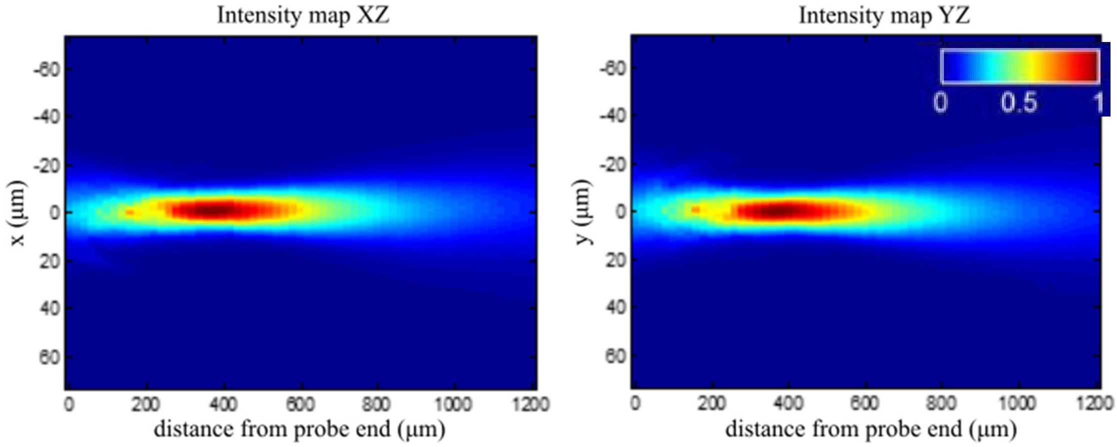

Figure 5.3: Beam profile in terms of an intensity map across XZ (left) and YZ (right)

axes. The colour index of black to blue relates to highest to lowest intensity detected respectively.

The beam intensities are uniform in both XZ and XY axes deeming it suitable to test on the aorta sample. In case, the beam intensity outputs were not symmetric and the parameters out of specification the fiber probe would have been redeveloped.

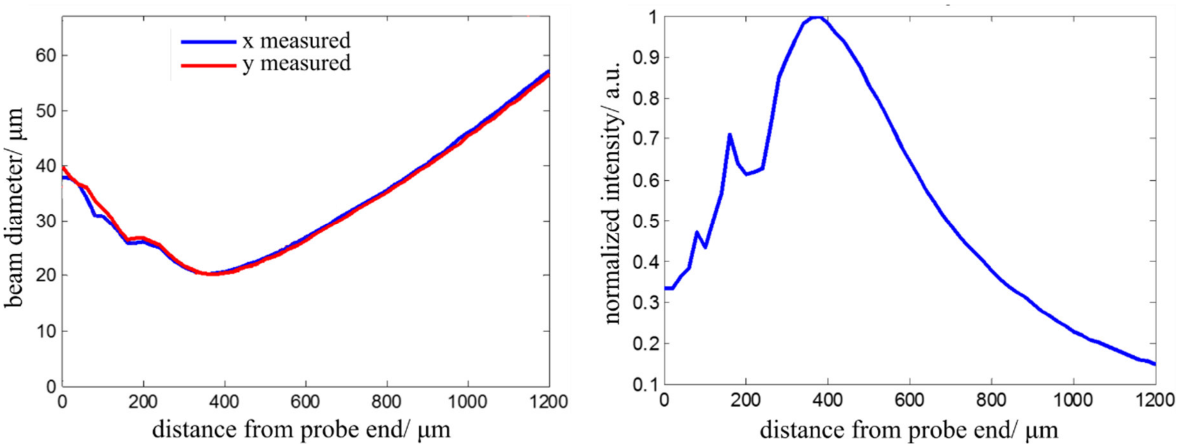

Figure 5.4: The change in beam diameter (left) and the on-axis intensity profile (right) throughout the probe

Fig. 5.4 further demonstrates the behavior of the beam where it can be approximated by a Gaussian profile, which was also assumed by the simulations. Since the intensity curve in both x and y are maintaining a good overlap, it was further confirmation that the beam was symmetric with a focus at 380 µm in air. The focal spot diameter was 20 µm.

5.3 SS-OCT fiber system

The measurement setup at OBEL labs was a swept source OCT (SS OCT) system with a bandwidth of 100 nm, centered at a principle wavelength of 1310 nm.

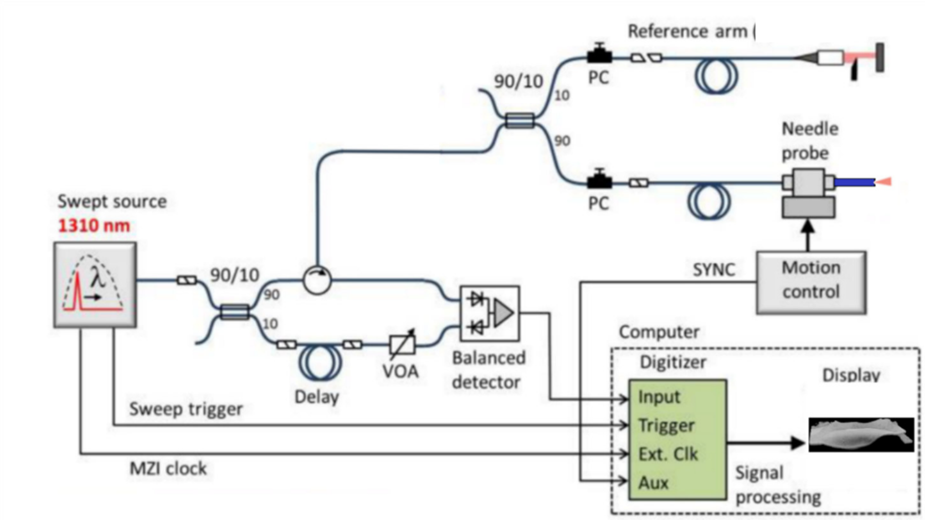

Figure 5.5: Schematic of the 1310 nm SS- OCT system coupled with the needle imaging fiber. (Modified and adapted from [116])

The basic working principle of the SS-OCT is that a tunable laser with a specific bandwidth consisting of narrow separated spectral lines would scan across the sample and provide an image after being Fourier transformed [119]. This method of producing cross-sectional images do not require the use of a spectrograph. The trigger pulses (50 kHz) were synchronized with the needle motion controller along with the signal acquisition such that after every trigger from the laser a signal would be recorded. A Mach-Zehnder interferometer (MZI) clock output of the source had been achieved that allowed time gated sampling in terms of frequency. The power input and output was monitored via power meters at the reference arm and free fiber ports where the light intensity split was taking place via beam splitters. As shown by the diagram the laser output signal had been split by a coupler where 90% of the input power was sent to the interferometer by a circulator. The other 10% was directed to a balanced detector that subtracted this signal from the returned interferometer response. This had enhanced the SNR and any laser fluctuations. The variable optical attenuator (VOA) had equalized the intensity levels between the interferometer and the laser power signal, which was necessary for a correct signal subtraction. The detector used was an InGaAs AC coupled photodetector.

For the measurements the sample holder was fixed to a moving stage and the need probe was positioned enface for the scanning process.

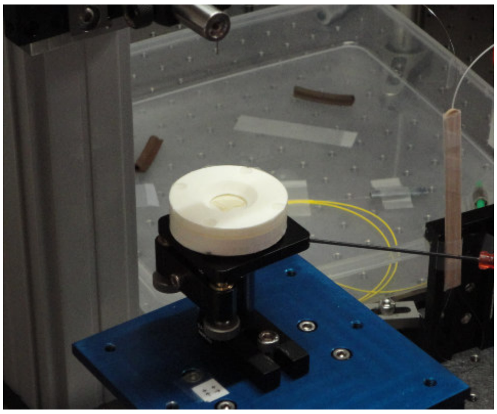

Figure 5.6: The placement of the aorta sample on the sample holder and mounted on a moving stage which is coupled with the source trigger. The needle probe is positioned on top using a holder.

A lot of care had been taken not to crash the needle probe onto the quartz window which might not only damage the needle probe but also the sample holder.

5.4 Application of the OCT needle probe on *ex vivo* rabbit aorta

The measurement process involved choosing a relevant scan area in terms of inserting x and y coordinates onto a custom-built software that had been developed to control the stage. Then an appropriate step size was chosen that would fit the laser spot size and the sample in question to achieve the desired imaging resolution. It was very important to align the stage so that any collisions between the fiber probe and the quartz window would be avoided. Index matching liquid (n=1.5) was applied between the fiber tip and the quartz surface to avoid harsh back reflections due to the change in refractive indices. At each step an A-scan would be collected and after the entire measurement the recorded A-scans were converted to B-scans by averaging 2 A-scans. The depth range achieved was 5 mm and therefore in a medium with n=1.35 (usual tissue refractive index) the achieved axial pixel size was 5.04 µm.

To enhance the image quality an apodization window (Hann), was used to reduce the side lobes of the axial point spread function before signal processing. Fig. 5.7 shows the steps in spectral processing where the apodization can be clearly seen.

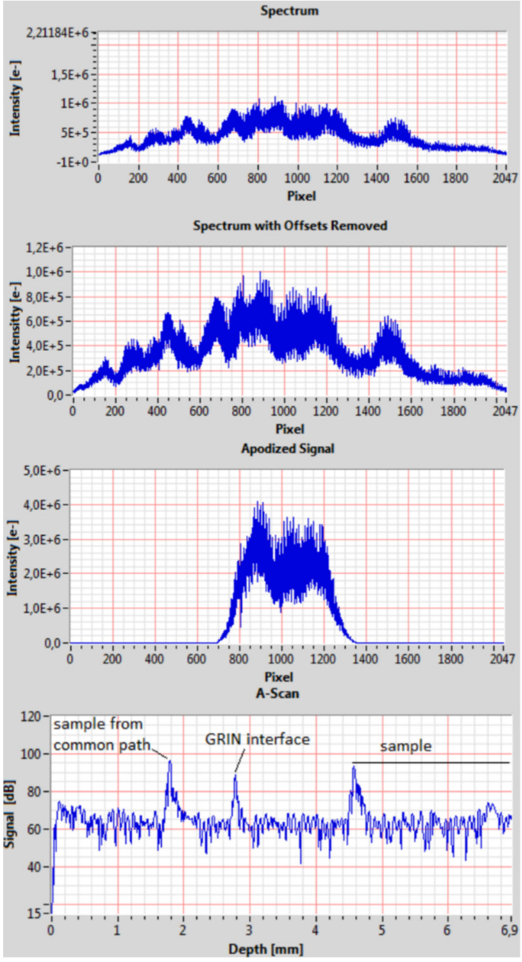

Figure 5.7: Steps of signal processing in fiber OCT and the interpretation of the signals observed.

After the Fourier transform, respective peaks of the sample as well as the reflections from the GRIN interface can be observed. The term referred to as "sample from common path" has been the sample signal observed after it has been reflected and superposed /interfered with the back reflected incident signal. Here the GRIN surface would act as a mirror that reflects the incident signal back into the fiber probe. This observation has resulted in utilizing this back reflected signal as the reference signal omitting an extra reference arm (common path). The reference signal produced by the common path is still independent from the sample. The sample arm had received a power of 32.4 mW.

As the Fig. 5.8 shows a 3D construction of the scanned rabbit aorta had displayed the rough surface structure that had been detected with the microscopic setup previously. The sample had been cut along the blood flow and flattened between the top and bottom of the sample holder which had resulted in the bright patchy regions on the 3D OCT image. Since these aortas had early plaque formations the cross sections did not show obvious plaque features besides small bumps as seen during the *in vivo* animal experiments. The slight shadowing also suggests that the uneven topography indeed relate to plaque formations [80].

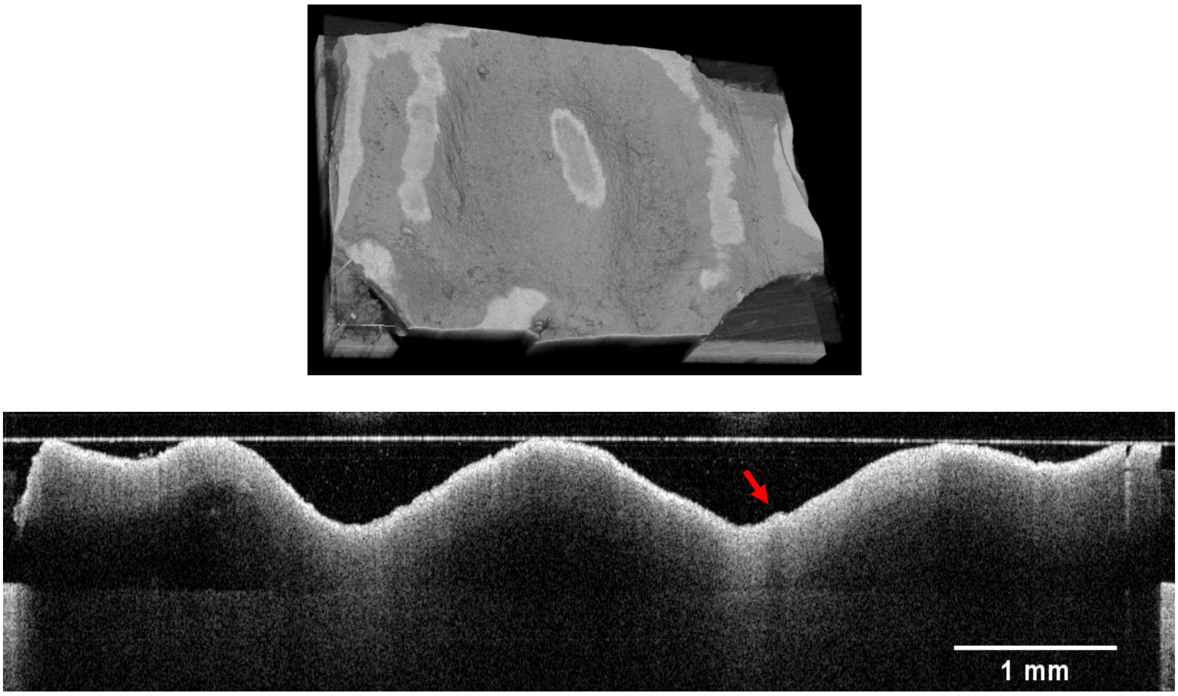

Figure 5.8: Top: 3D constructed image of a rabbit aorta measured with the SS-OCT and the needle probe. It consisted of 10.5 x 7 mm FOV with a resolution of 5x10 um across the corresponding axes. The laser power used was 200 mV at the reference and 1V range. Bottom: a B-scan demostrating the features on the aorta surface. The red arrow shows a small bump that represent lipid accumulation.

The results presented in the previous section have provided a detailed overview about the experiments performed in order to test the implementation and application of the OCT needle fiber probe on excised rabbit aortas. The main aim of this venture was to test the feasibility of miniaturizing the OCT-Raman system. Even though the Raman counterpart is pending, the OCT needle-fiber probe has produced promising results given that this had been the first attempt to image aortas. Similar to previous applications, more samples at different plaque development stages would be useful to provide a deeper insight into the capabilities of the needle probe. For further *in vivo* application the needle casing must be replaced with a material that is more flexible for easy passage through aortas. This would essentially reduce the invasiveness of the diagnostic surgeries and cardiologists would be able to extract more information.

One issue that may arise in an *in vivo* application would be the heartbeat of the patient interfering with the measurement. As a solution, Wang et al. had investigated the possibility of synchronizing with the heartbeat, which involved faster data recording [120-122]. By including Raman into this application, more chemical information can be obtained during the surgery.

6 Summary

The implementation of a combined OCT-Raman device has been presented along with its systematic characterization to assess performance and suitability for the measurements of biological samples important for medical diagnosis. With the main focus on non-melanoma skin cancer and atherosclerotic plaque investigations both OCT and Raman spectroscopy results were compared with histopathology which is the gold standard since many years. By correlating the results, it can be concluded that the combined device was able to differentiate between diseased and unaffected tissue. In an attempt to miniaturize the microscopic setup an OCT needle-fiber probe was developed with future expectations to combine with Raman spectroscopy.

The combination of the two modalities in the microscopy-based system takes place via dichroic mirrors placed strategically within an optical probe cage. The general measuring workflow consisted of OCT providing cross-sectional images of the samples followed by a Raman map of concerned areas to identify the constituents. The former enables quick morphological visualization of any concealed abnormalities beneath the surface that had assisted the latter analytical method to provide subsequent diagnostic information due to its high chemical specificity. The advantage of having two modalities consists of extracting more information in one diagnostic step that would definitely reduce the chain of laborious efforts required to carry out a fast and successful diagnosis. This will not only influence faster diagnosis but also reduce the number of surgeries which would lead to reduced risks of infection. Advantages and disadvantages of the combined setup have been summarized in Table 6.1.

Table 6.1 Summary of advantages and disadvantages of the combined OCT-Raman spectroscopy system.

Type of application *in vivo*	OCT- Raman	
	Advantages	Disadvantages
Non melanoma skin cancer differentiation	Both morphological and chemical data extracted	Optical equipment must fit both modalities
	Reduced number of surgeries by eliminating follow-up biopsies	Presence of high fluorescence masking Raman signal
	Ability to differentiate the border between diseased and healthy tissue	Raman laser power must be regulated
Atherosclerotic plaque identification	Same as above	Need to use contrast agents and X-ray imaging
	Plaque vulnerability confirmed via two modalities	Invasive
	Reduced risk of infections	

The OCT-Raman device demonstrated sufficient axial and lateral resolution (OCT- 10 µm and 13 µm, Raman spectroscopy- ~700 -1000 µm and ~105 µm) to identify the diseased from normal tissue. The most challenging task during the device implementation was the choice of objective lens. A total of 5 objective lenses were extensively tested on a standard as well as commercially available pork loin samples. This provided a preliminary overview of the spectral quality as well as the extent of the fluorescent background. Since the objective lens finalized for this combination was already a compromise, a better substitute would improve the spectral quality and would even be able to reduce the necessary laser power influencing the acceptance of such a device in medical industry. If the device were to be miniaturized in the form of a fiber probe, the issue with the objective lens will be resolved. This solution would be beneficial in both medical applications.

From the pilot non-melanoma skin cancer study valuable knowledge of the different skin cancer types was attained. Due to the large number of BCCs encountered during the clinical trial the final data analysis had a main focus on this specific type of tumor. The OCT B-scans of BCC samples showed a significant correlation with the H&E stained tissue sections. The accuracy of data correlation was limited by the inability to correlate OCT images with histopathology one-to-one due to standard hospital procedures. However, the OCT cross-sectional information coupled with Raman spectra is valuable in terms of extracting more information through a single measurement. A couple of SCC samples that were measured had produced larger fluorescence responses compared to that of BCCs that disabled the extraction of Raman responses.

A common limitation throughout the experiments was the lack of a large sample size. The pool of patients included in this study were reduced from 18 to 7 because of the system change that had taken place in an attempt to improve the collection efficiency which in fact enhanced the fluorescence response such that any Raman responses were obscured. From the 7 patients that were considered for this study, a trend in spectral shape was discovered that were consistent within the 7 BCC samples. A larger sample size would be necessary to run a successful classification model as well as a training dataset to enable the prediction of cancer and non-cancer regions accurately. Assuming large number of samples, a PLS-LDA algorithm would be suitable to predict the tumor borders in tissue. This would require a careful assessment of different types of BCC variations. As a future step, results from a large dataset could be used to create a database that directly assists the classification of tumor types in patients. In order to achieve reduced fluorescence counts and thus reduced noise levels, working in a longer wavelength range such as 1064 nm would be beneficial.

Even though this would produce longer integration times, clinical application would be still feasible with a ‘live diagnosis’ feature as a future implementation. Integrating the device onto a medical cart enabled mobility in clinics. The neat use of light-blocking material further shielded the Raman spectrometer and the probe head from stray light, which would have disturbed the Raman response. The system software fulfilled all the user requirements but further improvements would be necessary in terms of user friendliness. For future clinical applications the software must be revised and coupled with a robust algorithm that extends the current functionality to display the diagnosis along with a confidence level.

Atherosclerotic plaque imaging with the combined OCT-Raman setup was only focusing on *ex vivo* samples. Even though an initial overview of early plaques were provided by animal aortas, the advanced plaques were human samples. Since early plaques show no symptoms and carry a low rupture risk, an account of extensive investigations with human samples are limited. Once in the advanced stages invasive measures would then be advised to avoid stenosis. From existing literature, a fair understanding can been obtained regarding human plaque diagnosis via OCT [40, 80, 82, 123]. The main feature that had been observed in this study was the absence in detected OCT intensity where lipids or calcium deposits were present compared to that of unaffected tissue. Furthermore, the perfectly circular lumen had appeared deformed with swellings or erosions. When investigating *in vivo* atherosclerotic plaques (animal), the images obtained by OCT had a high probability to carry motion artefacts of breathing and heartbeat. To overcome such distortions a research group in the Netherlands had imaged coronary arteries within one cardiac cycle by implementing a fast OCT pullback method [120]. Thus, combining Raman spectroscopy with such a technique would enable a complete plaque diagnosis. The Raman spectra of the *ex vivo* rabbit samples showed evidence of cholesterol (702, 1437 and 1661 cm^{-1}) whereas human *ex vivo* samples did not show triglycerides but lipids (1442, 1660 and 2800 - 3000 cm^{-1}), calcium (960 cm^{-1}) and protein (1455-1650 cm^{-1}). Interpreting Raman spectra of aortas had required a thorough understanding of the plaque formation at a molecular level. To obtain a deeper understanding of the metabolic processes and the storage mechanisms of lipids in cells, Stiebing et al [124, 125] have investigated these processes via cellular incubation. However, at macroscopic levels these molecular features may not be present due to the complexity of organic tissue. The amount of observed fluorescence had drastically increased when measuring coagulated blood which also had a tendency to overheat. Therefore, for future steps, fresh samples without fixing in formalin would be recommended. The *in vivo* measurements lead to characterizing early plaques that provided evidence of device-suitability to this specific application. OCT and Raman spectroscopy both confirmed the presence of lipids.

For the application of the combined system in clinical conditions, an OCT-Raman fiber probe would be vital to reach into the arterial locations. The OCT fiber probe developed, had produced very clear B- and C-scans and conformed to the desired measuring parameters such as working distance, shape of the laser spot and resolution. However, to confirm this OCT fiber probe to be suitable for clinical measurements, more samples with different plaque stages should be investigated. Once the OCT-Raman fiber probe has been developed the measurement strategy can be further characterized for its suitability for *in vivo* measurements. With a Raman-free contrast agent, the usual workflow can be followed i.e. first imaging with OCT and then measuring concerned areas with Raman spectroscopy to identify the plaque contents. Compared with the current methods of diagnosis, faster and more efficient ways are vital as atherosclerosis could persist without showing symptoms until later stages. Potentially the developed needle probe can be applied in skin cancer imaging similar to that used for investigating breast cancer [51] that would enable more accurate differentiation of cancer borders in all directions. This, however, would not maintain the non-invasive criteria. Due to the difficulty and reluctance of welcoming novel technologies into the routine diagnostic workflow, it would take a few years to witness a large change in the medical industry. Given the increased interest in point-of-care devices [126], regulatory bodies could include the active testing of novel medical devices in order to obtain further knowledge of diseases and elevate the chances of recovery by early detection.

Zusammenfassung

Die Implementierung eines kombinierten OCT-Raman-Geräts wurde, zusammen mit seiner systematischen Charakterisierung zur Beurteilung der Leistung und Eignung für die Messungen von medizinisch-relevanten biologischen Proben, vorgestellt. Mit dem Schwerpunkt auf Nicht-Melanom-Hautkrebs und atherosklerotischen Plaque wurden sowohl OCT- als auch Raman-Spektroskopie-Ergebnisse mit der Histopathologie verglichen, die seit vielen Jahren der Goldstandard ist. Durch die Korrelation der Ergebnisse kann geschlussfolgert werden, dass das kombinierte Gerät in der Lage war, zwischen erkranktem und nicht betroffenem Gewebe zu unterscheiden. In einem Versuch, den mikroskopischen Aufbau zu miniaturisieren, wurde eine OCT-Nadelfasersonde entwickelt, die in Zukunft mit Raman-Spektroskopie kombiniert werden soll.

Die Kombination der beiden Modalitäten im Mikroskopiesystem erfolgt über dichroitische Spiegel, die strategisch in einem optischen Sondenaufbau platziert sind. Der allgemeine Messablauf bestand aus OCT-Scans, die Querschnittsbilder der Proben lieferten, gefolgt von Raman-Abbildungen der betroffenen Bereiche, um die Bestandteile zu identifizieren. Erstere ermöglichen eine schnelle morphologische Visualisierung von verborgenen Abnormitäten unterhalb der Oberfläche. Dies half der letzteren analytischen Methode, aufgrund ihrer hohen chemischen Spezifität nachfolgend diagnostische Information zu liefern. Der Vorteil in der Verwendung zweier Modalitäten besteht darin, mehr Informationen in einem diagnostischen Schritt zu extrahieren. Dies würde definitiv die mühsame Prozesskette, welche ansonsten für eine schnelle und erfolgreiche Diagnose erforderlich ist, reduzieren. Zudem wird es nicht nur für eine schnellere Diagnose sorgen, sondern auch die Zahl der Operationen reduzieren, was das Risiko von Infektionen verringert. Vor- und Nachteile des kombinierten Aufbaus sind in Tabelle 6.1 zusammengefasst.

Table 6.1 Zusammenfassung der Vorteile und Nachteile eines kombinierten OCT-Raman-Spektoskopie Systems.

Anwendungsbereich *in vivo*	OCT- Raman	
	Vorteile	Nachteile
Differenzierung von Nicht-Melanom-Hautkrebs	Sowohl morphologische als auch chemische Daten extrahierend	Optische Bauteile müssen zu beiden Modalitäten passen
	Reduzierte Anzahl an Operationen durch die Eliminierung von Folgebiopsien	Hohe Fluoreszenz überlagert das Raman-Signal

	Fähig die Grenze zwischen krankem und gesundem Gewebe festzustellen	Raman-Laserleistung muss reguliert werden
Identifizierung von atherosklerotischen Plaque	wie oben	Kontrastmittel und Röntgenbildgebung notwendig
	Vulnerable Plaque von zwei Modalitäten bestätigt	Invasiv
	Reduziertes Risiko von Infektionen	

Das OCT-Raman-Gerät zeigte eine ausreichende axiale und laterale Auflösung (OCT - 10µm und 13µm, Raman-Spektroskopie - 700 -1000µm und ~ 105µm), um das erkrankte Gewebe von dem Gesunden zu identifizieren. Die schwierigste Aufgabe während der Implementierung des Geräts war die Wahl der Objektivlinse. Eine Gesamtzahl von 5 Objektivlinsen wurde ausgiebig an einem Standard sowie einer kommerziell erhältlichen Schweinelenden-Probe getestet. Dies hat einen vorläufigen Überblick über die spektrale Qualität sowie das Ausmaß des fluoreszierenden Hintergrunds gegeben. Da die für diese Kombination ausgewählte Objektivlinse bereits einen Kompromiss darstellte, würde ein besserer Ersatz die spektrale Qualität weiter verbessern. Ein solcher würde es zudem ermöglichen, die notwendige Laserleistung zu reduzieren, welche die Akzeptanz einer solchen Vorrichtung in der medizinischen Industrie beeinflusst. Wenn das Gerät in Form einer Fasersonde miniaturisiert werden würde, wäre eine Objektivlinse nicht mehr notwendig. Diese Lösung wäre in beiden medizinischen Anwendungen vorteilhaft.

Aus der Nicht-Melanom-Hautkrebs-Pilotstudie wurde wertvolles Wissen über die verschiedenen Hautkrebsarten gewonnen. Aufgrund der großen Anzahl von Basalzellkarzinomen (BCCs), die während der klinischen Studie auftraten, lag der Schwerpunkt der abschließenden Datenanalyse auf dieser speziellen Art von Tumor. Die OCT-B-Scans von BCC-Proben hatten eine signifikante Korrelation mit den H & E-gefärbten Gewebeschnitten gezeigt. Aufgrund von standardisierten Krankenhausverfahren ließen sich die OCT-Bilder nicht eins zu eins mit der Histopathologie korrelieren. Dies limitierte die Genauigkeit der Datenkorrelation. Jedoch konnte durch die mit Raman-Spektren gekoppelte OCT-Querschnittsinformation mehr Information im Rahmen einer einzelnen Messung extrahiert werden. Ein paar der gemessenen SCC-Proben erzeugten größere Fluoreszenzsignale im Vergleich zu denen von BCCs, die die Extraktion von Raman-Signalen behinderten.

Eine häufige Einschränkung während der gesamten Experimente war das Fehlen einer großen Probenanzahl. Die für diese Studie verwertbare Patientenanzahl musste von 18 auf 7 reduziert werden, da das System verändert wurde, um die

Sammlungseffizienz zu erhöhen. Dies verstärkte jedoch die Fluoreszenz, sodass jegliche Raman-Signale verdeckt wurden. Von den 7 Patienten, die für diese Studie in Betracht gezogen wurden, wurde ein Trend in der spektralen Form entdeckt, der innerhalb der 7 BCC-Proben übereinstimmte. Eine größere Probenanzahl wäre erforderlich, um ein erfolgreiches Klassifizierungsmodell sowie einen Trainingsdatensatz zur Vorhersage von Krebs- und Nichtkrebsregionen zu erstellen. Als ein zukünftiger Schritt könnte ein großer Datensatz dafür verwendet werden, um eine Datenbank zu bilden, die die Klassifizierung von Tumortypen am Patienten direkt unterstützt. Unter der Annahme einer großen Anzahl von Proben wäre ein PLS-LDA-Algorithmus zur Vorhersage der Tumorgrenzen im Gewebe geeignet. Dies würde eine sorgfältige Bewertung verschiedener Arten von BCC-Variationen erfordern. Um eine verringerte Fluoreszenz zu erreichen und somit das Rauschlevel zu reduzieren, wäre das Messen in einem höheren Wellenlängenbereich, wie beispielsweise 1064nm, vorteilhaft. Obwohl dies zu längeren Integrationszeiten führen würde, wäre eine klinische Anwendung mit einer Live-Diagnose-Funktion als zukünftige Implementierung noch immer möglich. Die Integration des Geräts in einen medizinischen Wagen ermöglichte eine hohe Mobilität in Kliniken. Die Verwendung von lichtundurchlässigem Material schirmte das Raman-System und den Sondenkopf vor Streulicht ab, was das Raman-Signal gestört hätte. Die Systemsoftware erfüllte alle Benutzeranforderungen, jedoch wären weitere Verbesserungen hinsichtlich der Benutzerfreundlichkeit erforderlich. Für zukünftige medizinische Anwendungen muss die Software überarbeitet und mit einem robusten Algorithmus gekoppelt werden, der die aktuelle Funktionalität erweitert, um die Diagnose zusammen mit einem Konfidenzintervall anzuzeigen.

Die Bildgebung der atherosklerotische Plaques mit dem kombinierten OCT-Raman-System konzentrierte sich nur auf *ex vivo* Proben. Obwohl ein erster Überblick über frühe Plaques von Tieraortas geliefert wurde, waren die fortgeschrittenen Plaques menschliche Proben. Da frühe Plaques keine Symptome zeigen und ein geringes Bruchrisiko aufweisen, gibt es nur wenige umfassende Untersuchungen an menschlichen proben. Im fortgeschrittenen Stadium werden invasive Maßnahmen empfohlen, um eine Stenose zu vermeiden. Aus der bestehenden Literatur kann ein gutes Verständnis hinsichtlich der Plaque-Diagnose mittels OCT gewonnen werden [40, 80, 82, 124]. Das Hauptmerkmal, das in dieser Studie beobachtet wurde, war die geringe OCT-Intensität, an Stellen wo Lipide oder Calcium vorhanden waren, im Vergleich zu nicht betroffenem Gewebe. Darüber hinaus schien das perfekt kreisförmige Lumen mit Schwellungen oder Abnutzung deformiert zu sein. Bei *in vivo* Untersuchungen atherosklerotischer Plaques hatten die mit OCT gewonnenen Bilder eine hohe Wahrscheinlichkeit, Bewegungsartefakte von Atmung und Herzschlag zu tragen. Um solche Verzerrungen zu überwinden, hat eine Forschungsgruppe in den

Niederlanden Koronararterien innerhalb eines Herzzyklus durch Implementierung einer schnellen OCT-Pullback-Methode gemessen [121]. Die Kombination einer solchen Technik mit der Raman-Spektroskopie würde eine vollständige Plaque-Diagnose ermöglichen. Die Raman-Spektren der *ex vivo* Kaninchenproben zeigten einen Nachweis von Cholesterin (702, 1437 und 1661 cm^{-1}), während menschliche *ex vivo* Proben keine Triglyceride, aber anderweitige Lipide (1442, 1660 und 2800 - 3000 cm^{-1}), Calcium (960 cm^{-1}) und Protein (1455-1650 cm^{-1}) aufwiesen. Das Interpretieren von Raman-Spektren von Aorten erforderte ein gründliches Verständnis der Plaquebildung auf molekularer Ebene. Um ein tieferes Verständnis der metabolischen Prozesse und der Speichermechanismen von Lipiden in Zellen zu erhalten, haben Stiebing *et al.* [125, 126] diese Prozesse durch zelluläre Inkubation untersucht. Auf makroskopischer Ebene sind diese molekularen Merkmale jedoch möglicherweise aufgrund der Komplexität von organischem Gewebe nicht vorhanden. Der Anteil der beobachteten Fluoreszenz war bei der Messung von koaguliertem Blut, das ebenfalls zur Überhitzung neigte, drastisch angestiegen. Daher würden sich für zukünftige Schritte frische Proben ohne Fixierung in Formalin empfehlen. Die *in vivo* Messungen resultierten in der Charakterisierung früher Plaques, was die Eignung der Vorrichtung für diese spezielle Anwendung bewies. OCT und Raman-Spektroskopie bestätigten beide die Anwesenheit von Lipiden.

Für die endgültige Anwendung des kombinierten Systems unter klinischen Bedingungen wäre eine OCT-Raman-Fasersonde wichtig, um in die Arterien zu gelangen. Die entwickelte OCT-Fasersonde hatte sehr klare B- und C-Scans erzeugt und entsprach den gewünschten Messparametern wie Arbeitsabstand, Form des Laserspots und Auflösung. Um jedoch zu bestätigen, dass diese OCT-Fasersonde für klinische Messungen geeignet ist, sollten mehr Proben mit unterschiedlichen Stadien der Plaques untersucht werden. Sobald die OCT-Raman-Fasersonde entwickelt ist, kann die Messstrategie weiter auf ihre Eignung für *in vivo* Messungen charakterisiert werden. Mit einem Raman-freien Kontrastmittel kann der übliche Arbeitsablauf verfolgt werden, d.h. zuerst die Bildgebung mit OCT und dann die Messung betroffener Bereiche mit Raman-Spektroskopie, um den Plaquezu charakterisieren. Verglichen mit den derzeitigen Diagnoseverfahren sind schnellere und effizientere Wege wichtig, da die Atherosklerose ohne Symptome bis zu späten Stadien anhalten kann. Möglicherweise könnte die entwickelte Nadel-Sonde in der Hautkrebs-Bildgebung ähnlich der zur Untersuchung von Brustkrebs [51] verwendet werden. Eine genauere Differenzierung der Krebsgrenzen in alle Richtungen könnte ermöglicht werden. Dies würde jedoch das nicht-invasive Kriterium verletzen. Aufgrund der Schwierigkeit und der Zurückhaltung, neue Technologien in den routinemäßigen diagnostischen Arbeitsablauf aufzunehmen, würde es einige Jahre dauern, bis sich ein großer Wandel in der medizinischen Industrie abzeichnet. Angesichts des gestiegenen

Interesses an *Point-of-Care*-Geräten [127] könnten die Aufsichtsbehörden die aktive Prüfung neuartiger medizinischer Geräte einschließen, um weitere Kenntnisse über Krankheiten zu erlangen und die Heilungschancen durch Früherkennung zu erhöhen.

Statement of authorship

I hereby confirm that I have written the present thesis independently and without illicit assistance from third parties and using solely the aids mentioned.

Since some content have already been published as journal articles, permission was requested and has been granted to include the content and images in this thesis. The publications relevant are:

K. Egodage, C. Matthäus, S. Dochow, I.Schie, C. Härdtner, I. Hilgendorf and J. Popp, "Combination of OCT and Raman spectroscopy for improved characterization of atherosclerotic plaque depositions", Chinese Optics Letters, 2017, Volume 15, Issue 9, p. 090008.

C. Matthäus, S. Dochow, ***K. Egodage,*** I. Schie, B. F. Romeike, B. R. Brehm and J. Popp, "Detection and characterization of atherosclerotic plaques by Raman probe spectroscopy and optical coherence tomography (conference presentation)", Proceedings Volume 10042, Diagnostic and Therapeutic Applications of Light in Cardiology, SPIE BIOS, San Francisco, California, 2017.

K. Egodage, S. Dochow, T. Bocklitz, O. Chernavskaia, C. Matthäus, M. Schmitt and J. Popp, "The combination of optical coherence tomography and Raman spectroscopy for tissue characterization", Journal of Biomedical Photonics and Engineering,1, 30 June 2015, 169- 177.

Kokila Egodage

Place and date: Jena, 13.02.2018

Selbständigkeitserklärung

Ich versichere, dass ich die beiliegende Arbeit ohne Hilfe Dritte und ohne Benutzung anderer als der angegebenen Quelle und Hilfsmittel einschließlich des Internets angefertigt und die den benutzten Quellen wörtlich oder inhaltlich entnommenen Stellen als solche kenntlich gemacht habe.

Da einige Inhalte bereits als Zeitschriftenaufsätze veröffentlicht wurden, wurde um Erlaubnis gebeten und es wurde die Erlaubnis erteilt, den Inhalt und die Bilder in diese Arbeit aufzunehmen. Die relevanten Publikationen sind:

K. Egodage, C. Matthäus, S. Dochow, I.Schie, C. Härdtner, I. Hilgendorf and J. Popp, “Combination of OCT and Raman spectroscopy for improved characterization of atherosclerotic plaque depositions”, Chinese Optics Letters, 2017, Volume 15, Issue 9, p. 090008.

C. Matthäus, S. Dochow, ***K. Egodage,*** I. Schie, B. F. Romeike, B. R. Brehm and J. Popp, “Detection and characterization of atherosclerotic plaques by Raman probe spectroscopy and optical coherence tomography (conference presentation)”, Proceedings Volume 10042, Diagnostic and Therapeutic Applications of Light in Cardiology, SPIE BIOS, San Francisco, California, 2017.

K. Egodage, S. Dochow, T. Bocklitz, O. Chernavskaia, C. Matthäus, M. Schmitt and J. Popp, “The combination of optical coherence tomography and Raman spectroscopy for tissue characterization”, Journal of Biomedical Photonics and Engineering,1, 30 June 2015, 169- 177.

Unterschrift:

Ort, Datum: Jena, 13.02.2018

References

1. Velayos, F., P. Kathpalia, and E. Finlayson, *Changing Paradigms in Detection of Dysplasia and Management of Patients With Inflammatory Bowel Disease: Is Colectomy Still Necessary?* Gastroenterology, 2017. **152**(2): p. 440-450.e1.
2. Kim, S.G., et al., *Quality of Life after Endoscopic Submucosal Dissection for Early Gastric Cancer: A Prospective Multicenter Cohort Study.* Gut and Liver, 2017. **11**(1): p. 87-92.
3. Spinney, L., *Cancer: Caught in time.* Nature, 2006. **442**(7104): p. 736-738.
4. American Cancer Society, *Global cancer facts and figures* World Health Organization (WHO), Editor. 2015: Atlanta.
5. Black, C. *New initiative launched to tackle cardiovascular disease, the world's number one killer.* Global Hearts Initiative 2017 22 Sept. 2016 [cited 15 April 2017; WHO.
6. Barquera, S., et al., *Global Overview of the Epidemiology of Atherosclerotic Cardiovascular Disease.* Archives of Medical Research, 2015. **46**(5): p. 328-338.
7. Virmani, R., et al., *The Vulnerable Atherosclerotic Plaque: Strategies for Diagnosis and Management.* 2007: Blackwell Publishing.
8. Naghavi, M., et al., *From Vulnerable Plaque to Vulnerable Patient.* A Call for New Definitions and Risk Assessment Strategies: Part I, 2003. **108**(14): p. 1664-1672.
9. Kronz, J.D. and W.H. Westra, *The role of second opinion pathology in the management of lesions of the head and neck.* Current Opinion in Otolaryngology & Head and Neck Surgery, 2005. **13**(2): p. 81-84.
10. Longo, C., et al., *Routine Clinical-Pathologic Correlation of Pigmented Skin Tumors Can Influence Patient Management.* PLOS ONE, 2015. **10**(9): p. e0136031.
11. Popp, J., et al. *Raman meets medicine: Raman spectroscopy: a powerful tool in biophotonics.* 2009.
12. Mogensen, M. and G.B.E. Jemec, *Diagnosis of Nonmelanoma Skin Cancer/Keratinocyte Carcinoma: A Review of Diagnostic Accuracy of Nonmelanoma Skin Cancer Diagnostic Tests and Technologies.* Dermatologic Surgery, 2007. **33**(10): p. 1158-1174.
13. Drexler, W. and J.G. Fujimoto, *Optical coherence tomography: technology and applications.* 2008, Berlin-Heidelberg: Springer. p.1-45
14. de Boer, E., et al., *Optical innovations in surgery.* British Journal of Surgery, 2015. **102**(2): p. e56-e72.

15. Mogensen, M., et al., *Assessment of Optical Coherence Tomography Imaging in the Diagnosis of Non-Melanoma Skin Cancer and Benign Lesions Versus Normal Skin: Observer-Blinded Evaluation by Dermatologists and Pathologists.* Dermatologic Surgery, 2009. **35**(6): p. 965-972.
16. Korde, V.R., et al., *Using optical coherence tomography to evaluate skin sun damage and precancer.* Lasers in Surgery and Medicine, 2007. **39**(9): p. 687-695.
17. Gambichler, T., et al., *In vivo optical coherence tomography of basal cell carcinoma.* Journal of Dermatological Science, 2007. **45**(3): p. 167-173.
18. Olmedo, J.M., et al., *Optical coherence tomography for the characterization of basal cell carcinoma in vivo: A pilot study.* Journal of the American Academy of Dermatology, 2006. **55**(3): p. 408-412.
19. Gladkova, N.D., et al., *In vivo optical coherence tomography imaging of human skin: norm and pathology.* Skin Research and Technology, 2000. **6**(1): p. 6-16.
20. Themstrup, L., et al., *Optical coherence tomography imaging of non-melanoma skin cancer undergoing photodynamic therapy reveals subclinical residual lesions.* Photodiagnosis and Photodynamic Therapy, 2014. **11**(1): p. 7-12.
21. Hussain, A., L. Themstrup, and G. Jemec, *Optical coherence tomography in the diagnosis of basal cell carcinoma.* Archives of Dermatological Research, 2015. **307**(1): p. 1-10.
22. Cheng, H.M. and P. Guitera, *Systematic review of optical coherence tomography usage in the diagnosis and management of basal cell carcinoma.* British Journal of Dermatology, 2015: p. 1371–1380
23. Gambichler, T., V. Jaedicke, and S. Terras, *Optical coherence tomography in dermatology: technical and clinical aspects.* Archives of Dermatological Research, 2011. **303**(7): p. 457-473.
24. Scalvenzi, M., et al., *Dermoscopic patterns of superficial basal cell carcinoma.* International Journal of Dermatology, 2008. **47**(10): p. 1015-1018.
25. Tao, Z., et al., *Early tumor detection afforded by in vivo imaging of near-infrared II fluorescence.* Biomaterials, 2017. **134**: p. 202-215.
26. Haque, A., et al., *Next generation NIR fluorophores for tumor imaging and fluorescence-guided surgery: A review.* Bioorganic & Medicinal Chemistry, 2017. **25**(7): p. 2017-2034.
27. Jurowski, K., et al., *Comprehensive review of trends and analytical strategies applied for biological samples preparation and storage in modern medical lipidomics: State of the art.* TrAC Trends in Analytical Chemistry, 2017. **86**: p. 276-289.
28. Eberhardt, K., et al., *Advantages and limitations of Raman spectroscopy for molecular diagnostics: an update.* Expert Review of Molecular Diagnostics, 2015. **15**(6): p. 773-787.

29. Krafft, C., et al., *Raman and coherent anti-Stokes Raman scattering microspectroscopy for biomedical applications.* Journal of Biomedical Optics, 2012. **17**(4): p. 0408011-04080115.

30. Ashok, P.C., et al. *Combined information from Raman spectroscopy and optical coherence tomography for enhanced diagnostic accuracy in tissue discrimination.* in *Biomedical Vibrational Spectroscopy VI: Advances in Research and Industry.* 2014. Proc. SPIE 8939.

31. Kong, K., et al., *Diagnosis of tumors during tissue-conserving surgery with integrated autofluorescence and Raman scattering microscopy.* Proceedings of the National Academy of Sciences, 2013. **110**(38): p. 15189-15194.

32. Calin, M., et al., *Optical techniques for the noninvasive diagnosis of skin cancer.* Journal of Cancer Research and Clinical Oncology, 2013. **139**(7): p. 1083-1104.

33. Patil, C.A., et al., *A clinical instrument for combined raman spectroscopy-optical coherence tomography of skin cancers.* Lasers in Surgery and Medicine, 2011. **43**(2): p. 143-151.

34. Patil, C.A., et al., *Integrated system for combined Raman spectroscopy–spectral domain optical coherence tomography.* Journal of Biomedical Optics, 2011. **16**(1): p. 011007-011007-10.

35. Patil, C.A., et al., *Combined Raman spectroscopy and optical coherence tomography device for tissue characterization.* Optics Letters, 2008. **33**(10): p. 1135-1137.

36. Evans, J.W., et al., *Optical coherence tomography and Raman spectroscopy of the ex-vivo retina.* Journal of Biophotonics, 2009. **2**(6-7): p. 398-406.

37. Egawa, M., et al., *In vivo characterization of the structure and components of lesional psoriatic skin from the observation with Raman spectroscopy and optical coherence tomography: A pilot study.* Journal of Dermatological Science, 2010. **57**(1): p. 66-69.

38. van Soest, G., et al., *Imaging atherosclerotic plaque composition with intracoronary optical coherence tomography.* Netherlands Heart Journal, 2009. **17**(11): p. 448-450.

39. van der Meer, F.J., et al., *Quantitative optical coherence tomography of arterial wall components.* Lasers in Medical Science, 2005. **20**(1): p. 45-51.

40. Regar, E., T.G. van Leeuwen, and P.W. Serruys, *Optical coherence tomography in cardiovascular research.* 2008, New York: informa healthcare.

41. Kang, S.-J., et al., *Combined IVUS and NIRS Detection of Fibroatheromas: Histopathological Validation in Human Coronary Arteries.* JACC: Cardiovascular Imaging, 2015. **8**(2): p. 184-194.

42. Huynh, K., *Imaging: Combining IVUS and NIRS improves accuracy of fibroatheroma detection.* Nat Rev Cardiol, 2015. **12**(3): p. 130-130.

43. Wang, T., et al., *Detection of plaque structure and composition using OCT combined with two-photon luminescence (TPL) imaging.* Lasers Surg Med., 2015. **47**(6): p. 485-94.

44. Bec, J., et al., *Multispectral fluorescence lifetime imaging system for intravascular diagnostics with ultrasound guidance: in vivo validation in swine arteries.* J Biophotonics, 2014. **7**(5): p. 281.

45. Phipps, J., et al., *A fluorescence lifetime imaging classification method to investigate the collagen to lipid ratio in fibrous caps of atherosclerotic plaque.* Lasers Surg Med., 2012. **44**(12): p. 564-71.

46. Park, J., et al., *Biochemical characterization of atherosclerotic plaques by endogenous multispectral fluorescence lifetime imaging microscopy.* Atherosclerosis, 2012. **220**(2): p. 394-401.

47. Matthäus, C., et al., *Multimodal nonlinear imaging of atherosclerotic plaques differentiation of triglyceride and cholesterol deposits.* J Innov Opt Heal Sci., 2014. **7**(5): p. 1450027.

48. Cicchi, R., et al., *Non-linear imaging and characterization of atherosclerotic arterial tissue using combined SHG and FLIM microscopy.* J Biophotonics., 2015. **8**(4): p. 347-56.

49. Ko, A., et al., *Multimodal nonlinear optical imaging of atherosclerotic plaque development in myocardial infarction-prone rabbits.* J Biomed Opt., 2010. **15**(2): p. 020501.

50. Lim, R., et al., *Multimodal CARS microscopy determination of the impact of diet on macrophage infiltration and lipid accumulation on plaque formation in ApoE-deficient mice.* J Lipid Res., 2010. **51**(7): p. 1729-37.

51. McLaughlin, R.A., et al., *Imaging of Breast Cancer With Optical Coherence Tomography Needle Probes: Feasibility and Initial Results.* IEEE Journal of Selected Topics in Quantum Electronics, 2012. **18**(3): p. 1184-1191.

52. McLaughlin, R.A., et al., *Static and dynamic imaging of alveoli using optical coherence tomography needle probes.* Journal of Applied Physiology, 2012. **113**(6): p. 967-974.

53. Kerkhof, M., et al., *Grading of dysplasia in Barrett's oesophagus: substantial interobserver variation between general and gastrointestinal pathologists.* Histopathology, 2007. **50**(7): p. 920-927.

54. Fujimoto, J.G., et al., *Optical Coherence Tomography: An Emerging Technology for Biomedical Imaging and Optical Biopsy.* Neoplasia, 2000. **2**(1): p. 9-25.

55. Brezinski, M.E., *Optical coherence tomography.* Principles and applications. 2006, California, USA: Eslevier Inc.

56. Huang, D., et al., *Optical Coherence Tomography.* Science (New York, N.Y.), 1991. **254**(5035): p. 1178-1181.

57. Brezinski, M.E., et al., *Imaging of coronary artery microstructure (in vitro) with optical coherence tomography.* The American Journal of Cardiology, 1996. **77**(1): p. 92-93.
58. J.M. Schmitt, C.P., S. Zhang, R. Lovec and C. Xu, *Development of OCT technology for clinical applications*, in *Optical coherence tomography: technology and applications*, W.D.a.J.G. Fujimoto, Editor. 2008, Springer: Springer-Verlag Berlin Heidelberg
59. Bezerra, H.G., et al., *Intracoronary Optical Coherence Tomography: A Comprehensive ReviewClinical and Research Applications.* JACC: Cardiovascular Interventions, 2009. **2**(11): p. 1035-1046.
60. Tomlins, P.H. and R.K. Wang, *Theory, developments and applications of optical coherence tomography.* Journal of Physics D: Applied Physics, 2005. **38**(15): p. 2519.
61. Bousi, E. and C. Pitris. *Lateral resolution improvement in Optical Coherence Tomography (OCT) images.* in *2012 IEEE 12th International Conference on Bioinformatics & Bioengineering (BIBE).* 2012.
62. Hamdan, R., et al., *Optical coherence tomography: From physical principles to clinical applications.* Archives of Cardiovascular Diseases, 2012. **105**(10): p. 529-534.
63. Sharma, U., E.W. Chang, and S.H. Yun, *Long-wavelength optical coherence tomography at 1.7 μm for enhanced imaging depth.* Optics express, 2008. **16**(24): p. 19712-19723.
64. Schmitt, J.M., *Optical coherence tomography (OCT): a review.* Selected Topics in Quantum Electronics, IEEE Journal of, 1999. **5**(4): p. 1205-1215.
65. Yaqoob, Z., J. Wu, and C. Yang, *Spectral domain optical coherence tomography: a better OCT imaging strategy.* Biotechniques, 2005. **39**(6 Suppl): p. S6-13.
66. Fercher, A.F., et al., *Optical coherence tomography-principles and applications.* Reports on progress in physics, 2003. **66**(2): p. 239.
67. Freitas, A., M. Amaral, and M. Raele, *Optical Coherence Tomography: Development and Applications*, in *Laser Pulse Phenomena and Applications*, F.J. Duarte, Editor. 2010, InTech: Available from: https://www.intechopen.com/books/laser-pulse-phenomena-and-applications/optical-coherence-tomography-development-and-applications.
68. Hanlon, E., et al., *Prospects for in vivo Raman spectroscopy.* Physics in medicine and biology, 2000. **45**(2): p. R1.
69. Parra-Murillo, C.A., et al., *Stokes-anti-Stokes correlation in the inelastic scattering of light by matter and generalization of the Bose-Einstein population function.* Physical Review B, 2016. **93**(12): p. 125141.

70. Zaleski, S., et al., *Identification and Quantification of Intravenous Therapy Drugs Using Normal Raman Spectroscopy and Electrochemical Surface-Enhanced Raman Spectroscopy.* Analytical Chemistry, 2017. **89**(4): p. 2497-2504.
71. Ghesti, G.F., et al., *Application of raman spectroscopy to monitor and quantify ethyl esters in soybean oil transesterification.* Journal of the American Oil Chemists' Society, 2006. **83**(7): p. 597-601.
72. *Diffraction grating.* 2017 [cited 20.12. 2017 2017]; B&W Tek; Available from: http://bwtek.com/spectrometer-part-2-the-grating/.
73. Choo-Smith, L.P., et al., *Medical applications of Raman spectroscopy: From proof of principle to clinical implementation.* Biopolymers, 2002. **67**(1): p. 1-9.
74. Santos, I.P., et al., *Raman spectroscopy for cancer detection and cancer surgery guidance: translation to the clinics.* Analyst, 2017. **142**(17): p. 3025-3047.
75. Bratchenko, I.A., et al., *Combined Raman and autofluorescence ex vivo diagnostics of skin cancer in near-infrared and visible regions.* Journal of Biomedical Optics, 2017. **22**(2): p. 027005-027005.
76. Lim, L., et al. *Clinical study of noninvasive in vivo melanoma and nonmelanoma skin cancers using multimodal spectral diagnosis.* 2014. SPIE.
77. Patterson, J.W., *Weedon's skin pathology.* 4 ed. 2015: Elsevier - Health Sciences Division.
78. Afolabi, A., et al., *Role of Optical Coherence Tomography in Diagnosis and Treatment of Patients with Acute Coronary Syndrome.* Cardiovascular Innovations and Applications, 2017. **2**(2): p. 229-235.
79. van Soest, G., et al., *Atherosclerotic tissue characterization in vivo by optical coherence tomography attenuation imaging.* Journal of Biomedical Optics, 2010. **15**(1).
80. Tarkin, J.M., et al., *Imaging Atherosclerosis.* Circulation Research, 2016. **118**(4): p. 750.
81. Di Vito, L., et al., *Identification and quantification of macrophage presence in coronary atherosclerotic plaques by optical coherence tomography.* European Heart Journal - Cardiovascular Imaging, 2015.
82. Uemura, S., et al., *Assessment of Coronary Plaque Vulnerability with Optical Coherence Tomography.* Acta Cardiologica Sinica, 2014. **30**(1): p. 1-9.
83. De Rosa, R., et al., *Coronary Atherosclerotic Plaque Characteristics and Cardiovascular Risk Factors — Insights From an Optical Coherence Tomography Study —.* Circulation Journal, 2017.
84. Poll, S.W.E.v.d., et al., *Raman Spectroscopy of Atherosclerosis.* Journal of Cardiovascular Risk, 2002. **9**(5): p. 255-261.

85. Matthäus, C., et al., *In Vivo Characterization of Atherosclerotic Plaque Depositions by Raman-Probe Spectroscopy and in Vitro Coherent Anti-Stokes Raman Scattering Microscopic Imaging on a Rabbit Model.* Analytical Chemistry, 2012. **84**(18): p. 7845-7851.
86. MacRitchie, N., et al., *Molecular imaging of atherosclerosis: spotlight on Raman spectroscopy and surface-enhanced Raman scattering.* Heart, 2017.
87. Egodage, K., et al., *The combination of optical coherence tomography and Raman spectroscopy for tissue characterization.* Journal of Biomedical Photonics & Engineering, 2015. **1**(2): p. 169-177.
88. Khan, K.M., et al., *Depth-sensitive Raman spectroscopy combined with optical coherence tomography for layered tissue analysis.* Journal of Biophotonics, 2014. **7**(1-2): p. 77-85.
89. Ryan, C., et al., *SNIP, a statistics-sensitive background treatment for the quantitative analysis of PIXE spectra in geoscience applications.* Nucl Instrum Methods Phys Res B. , 1988. **34**(4): p. 396-402.
90. Jung, E.C. and H.I. Maibach, *Animal models for percutaneous absorption.* Journal of Applied Toxicology, 2014. **35**(1): p. 1-10.
91. Zhao, J.e.a., *Biomedical optical imaging technologies: design and applications.* 2013, Berlin Heidelberg: Springer-Verlag.
92. Hoorens, I., et al., *Is early detection of basal cell carcinoma worthwhile? Systematic review based on the WHO criteria for screening.* British Journal of Dermatology, 2016. **174**(6): p. 1258-1265.
93. Hata, T.R., et al., *Non-Invasive Raman Spectroscopic Detection of Carotenoids in Human Skin.* Journal of Investigative Dermatology, 2000. **115**(3): p. 441-448.
94. Haka, A.S., et al., *Diagnosing breast cancer using Raman spectroscopy: prospective analysis.* Journal of Biomedical Optics, 2009. **14**(5): p. 054023.
95. Crowson, A.N., *Basal cell carcinoma: biology, morphology and clinical implications.* Mod Pathol, 2006. **19**(S2): p. S127-S147.
96. Schuh, S., et al., *Comparison of different optical coherence tomography devices for diagnosis of non-melanoma skin cancer.* Skin Research and Technology, 2016: p. n/a-n/a.
97. Telfer, N.R., G.B. Colver, and C.A. Morton, *Guidelines for the management of basal cell carcinoma.* British Journal of Dermatology, 2008. **159**(1): p. 35-48.
98. Cheng, H.M., et al., *Accuracy of optical coherence tomography for the diagnosis of superficial basal cell carcinoma – a prospective, consecutive, cohort study of 168 cases.* British Journal of Dermatology, 2016: p. n/a-n/a.
99. Yanni, A.E., *The laboratory rabbit: an animal model of atherosclerosis research.* Laboratory Animals, 2004. **38**(3): p. 246-256.

100. Fan, J., et al., *Rabbit models for the study of human atherosclerosis: from pathophysiological mechanisms to translational medicine.* Pharmacology & therapeutics, 2015. **0**: p. 104-119.
101. Movasaghi, Z., S. Rehman, and I.U. Rehman, *Raman Spectroscopy of Biological Tissues.* Applied Spectroscopy Reviews, 2007. **42**(5): p. 493-541.
102. Egodage, K., et al., *Combination of OCT and Raman spectroscopy for improved characterization of atherosclerotic plaque depositions.* Chinese Optics Letters, 2017. **15**(9): p. 090008.
103. Winter , M., *N-FINDR: an algorithm for fast autonomous spectral end-member determination in hyperspectral data.* . Proc. SIE, 1999: p. pp 266-275.
104. Hedegaard, M., et al., *Spectral unmixing and clustering algorithms for assessment of single cells by Raman microscopic imaging.* . Theor Chem Acc 2011. **130**(4-6): p. 1249-1260.
105. Beleites, C. and V. Sergo. *`hyperSpec: a package to handle hyperspectral data sets in R. ', R package version 098-20150304* 2016.
106. Howell, N.K., H. Herman, and E.C.Y. Li-Chan, *Elucidation of Protein−Lipid Interactions in a Lysozyme−Corn Oil System by Fourier Transform Raman Spectroscopy.* Journal of Agricultural and Food Chemistry, 2001. **49**(3): p. 1529-1533.
107. Elder, J.B. and G. Rao, *Intraoperative imaging, An issue of neurosurgery clinics of North Amrtica*, ed. S. Eastman. Vol. 28. 2017, Pennsylvania: Elsevier.
108. Matthäus C, et al., *In vivo characterization of atherosclerotic plaque depositions by Raman-probe spectroscopy and in vitro coherent anti-stokes Raman scattering microscopic imaging on a rabbit model.* Anal Chem., 2012. **84**(18): p. 7845-51.
109. Motz JT, et al., *In vivo Raman spectral pathology of human atherosclerosis and vulnerable plaque.* J Biomed Opt., 2006. **11**(2): p. 021003.
110. Sćepanović OR, et al., *Multimodal spectroscopy detects features of vulnerable atherosclerotic plaque.* J Biomed Opt., 2011. **16**(1): p. 011009.
111. Speck, U., et al., *How does a drug-coated balloon work? Overview about coating technologies and their impact.* J Cardiovasc Surg (Torino). , 2015: p. Epub ahead of print.
112. Zeller, T., et al., *Novel Approaches to the Management of Advanced Peripheral Artery Disease: Perspectives on Drug-Coated Balloons, Drug-Eluting Stents, and Bioresorbable Scaffold.* Curr Cardiol Rep., 2015. **17**(9): p. 624.
113. Banerjee, S., et al., *Drug-coated balloon and stent therapies for endovascular treatment of atherosclerotic superficial femoral artery disease.* Curr Cardiol Rep., 2015. **17**(5): p. 36.

114. Balss, K., et al., *Multivariate analysis applied to the study of spatial distributions found in drug-eluting stent coatings by confocal Raman microscopy.* Anal Chem., 2008. **80**(13): p. 4853-9.

115. Belu, A., C. Mahoney, and K. Wormuth, *Chemical imaging of drug eluting coatings: combining surface analysis and confocal Raman microscopy.* J Control Release, 2008. **26**(2): p. 111-21.

116. Yang, X., et al., *Imaging deep skeletal muscle structure using a high-sensitivity ultrathin side-viewing optical coherence tomography needle probe.* Biomedical optics express, 2014. **5**(1): p. 136-148.

117. Kuo, W.-C., et al., *Real-time three-dimensional optical coherence tomography image-guided core-needle biopsy system.* Biomedical Optics Express, 2012. **3**(6): p. 1149-1161.

118. Siegman, A.E., *Lasers.* 1986, Sausalito, California: University Science Books.

119. Podoleanu, A.G., *Optical coherence tomography.* The British Journal of Radiology, 2005. **78**(935): p. 976-988.

120. Wang, T., et al., *Heartbeat OCT: in vivo intravascular megahertz-optical coherence tomography.* Biomedical Optics Express, 2015. **6**(12): p. 5021-5032.

121. Wang, T., et al., *Development of a high-speed synchronous micro motor and its application in intravascular imaging.* Sensors and Actuators A: Physical, 2014. **218**(0): p. 60-68.

122. Wang, T., et al., *Intravascular optical coherence tomography imaging at 3200 frames per second.* Optics Letters, 2013. **38**(10): p. 1715-1717.

123. Mintz, G.S., *Intravascular Imaging of Coronary Calcification and Its Clinical Implications.* JACC: Cardiovascular Imaging, 2015. **8**(4): p. 461-471.

124. Stiebing, C., et al., *Complexity of fatty acid distribution inside human macrophages on single cell level using Raman micro-spectroscopy.* Analytical and Bioanalytical Chemistry, 2014. **406**(27): p. 7037-7046.

125. Stiebing, C., et al., *Raman imaging of macrophages incubated with triglyceride-enriched oxLDL visualizes translocation of lipids between endocytic vesicles and lipid droplets.* Journal of Lipid Research, 2017. **58**(9).

126. Howick, J., et al., *Current and future use of point-of-care tests in primary care: an international survey in Australia, Belgium, The Netherlands, the UK and the USA.* BMJ Open, 2014. **4**(8).